UNIVERSIDADE FEDERAL DE ITAJUBÁ - UNIFEI
PROGRAMA DE PÓS-GRADUAÇÃO EM ENGENHARIA MECÂNICA

Estimation of Thermal Efficiency in Capacitive Discharge Welding Using Inverse Problems: Experimental and Numerical Analysis of the Effects of Measurement with Thermocouples

Fábio Silva Faria

Itajubá, July 7 2025

UNIVERSIDADE FEDERAL DE ITAJUBÁ - UNIFEI
PROGRAMA DE PÓS-GRADUAÇÃO EM ENGENHARIA MECÂNICA

Fábio Silva Faria

Estimation of Thermal Efficiency in Capacitive Discharge Welding Using Inverse Problems: Experimental and Numerical Analysis of the Effects of Measurement with Thermocouples.

Thesis submitted to the Postgraduate Program in Mechanical Engineering as part of the requirements to obtain the doctorate degree in mechanical engineering.

Field of learning: Fluid-thermal and Flow Machines

Advisor: Prof. Dr. Sandro Metrevelle Marcondes de Lima e Silva
Co-advisor: Prof. Dr. Philippe Le Masson

July 7 2025
Itajubá

UNIVERSIDADE FEDERAL DE ITAJUBÁ - UNIFEI
PROGRAMA DE PÓS-GRADUAÇÃO EM ENGENHARIA MECÂNICA

Estimation of Thermal Efficiency in Capacitive Discharge Welding Using Inverse Problems: Experimental and Numerical Analysis of the Effects of Measurement with Thermocouples.

Fábio Silva Faria

Thesis awarded for thesis committee in 7 July 2025

Defense committee membership:
Prof. Dr. Helcio Rangel Barreto Orlande - UFRJ
Prof. Dr. Jean-Luc Battaglia - Université de Bordeaux
Prof. Dr. Antonio Augusto Araujo Pinto da Silva - UNIFEI
Prof. Dr. Rogério Fernandes Brito - UNIFEI
Prof. Dr. Sandro Metrevelle Marcondes de Lima e Silva (advisor) - UNIFEI
Prof. Dr. Philippe Le Masson (Co-advisor) - UBS

Itajubá
2025

Fábio Silva Faria
Estimation of Thermal Efficiency in Capacitive Discharge Welding Using Inverse Problems: Experimental and Numerical Analysis of the Effects of Measurement with Thermocouples/ Fábio Silva Faria. – Itajubá, July 7 2025-
105 p. : il. (algumas color.) ; 30 cm.

Advisor: Prof. Dr. Sandro Metrevelle Marcondes de Lima e Silva

Tese (Doutorado)
Universidade Federal de Itajubá - UNIFEI
Programa de pós-graduação em engenharia mecânica, July 7 2025.

1. Descarga Capacitiva. 2. Técnica da Função Especificada. 3. Comsol. 4. Efeito Joule. I. Prof. Dr. Sandro Metrevelle Marcondes de Lima e Silva. II. Universidade Federal de Itajubá. III. Estimativa da Eficiência térmica em Soldagem por Descarga Capacitiva Usando Problemas Inversos: Análise Experimental e Numérica dos Efeitos da Medição com Termopares

CDU 07:181:009.3

Fábio Silva Faria

Estimation of Thermal Efficiency in Capacitive Discharge Welding Using Inverse Problems: Experimental and Numerical Analysis of the Effects of Measurement with Thermocouples

Thesis submitted to the Postgraduate Program in Mechanical Engineering as part of the requirements to obtain the doctorate degree in mechanical engineering.

Work approved. Itajubá, 7 de July de 2025:

Prof. Dr. Sandro Metrevelle Marcondes de Lima e Silva- UNIFEI
Advisor

Prof. Dr. Philippe Le Masson- UBS
Co-advisor

Prof. Dr. Helcio Rangel Barreto Orlande - UFRJ

Prof. Dr. Jean-Luc Battaglia - Université de Bordeaux

Prof. Dr. Antonio Augusto Araujo Pinto da Silva - UNIFEI

Prof. Dr. Rogério Fernandes Brito - UNIFEI

Itajubá
July 7 2025

Acknowledgements

Agradeço a Deus, que é bom o tempo todo, pela vida, pela sabedoria e pelo amor.

Aos meus pais Guilherme e Lourdes que sempre estiveram ao meu lado e deram o apoio necessário para que mais uma etapa fosse concluída.

À minha esposa, Karina Silva Rodrigues, pela paciência e incentivo durante todo o processo.

Aos professores, Dr. Sandro Metrevelle Marcondes de Lima e Silva e Dr. Philippe Le Masson, pela oportunidade e confiança em meu trabalho, pelo apoio e pela orientação ao longo do curso.

Aos colegas do Laboratório de Transferência de Calor, em especial àqueles que participaram diretamente no trabalho: Mariana de Melo Antunes e Rodrigo Gustavo Dourado da Silva por todo auxílio na elaboração do trabalho.

Ao Conselho Nacional do desenvolvimento Científico e Tecnológico (CNPq), pelo apoio financeiro através da concessão de bolsa.

À Fundação de Amparo à Pesquisa do Estado de Minas Gerais (FAPEMIG), ao Conselho de Aperfeiçoamento de Pessoal de Nível Superior (CAPES) pelo suporte financeiro e também ao Instituto de Engenharia Mecânica – IEM pela estrutura fornecida para o desenvolvimento desse trabalho.

“A persistência é o caminho do êxito”

(Charlie Chaplin)

Abstract

Temperature measurement is critical in various engineering applications, particularly in processes involving high thermal gradients and rapid heating, such as welding. Accurate temperature data are essential for quality control, process optimization, and safety assurance in industrial operations. However, in fast and high-energy processes like Capacitor Discharge Welding (CDW), precise temperature measurement poses significant challenges, especially due to the difficulty of attaching thermocouples with minimal thermal contact resistance and high repeatability. This work presents an analysis of the process of attaching K-type thermocouples to metallic surfaces using a custom-designed CDW device. The development of this device aimed to overcome the scarcity of commercial equipment suitable for this purpose, improve the thermal contact between the thermocouple and the metallic surface, and reduce contact resistance, which directly affects the accuracy of temperature readings. Furthermore, the design of the equipment enabled better control and understanding of the electrical parameters, which were later integrated into the thermal analysis. Experimental and numerical methods were employed throughout the study. In the first stage, a simplified configuration using a single chromel wire was used to isolate and study heat transfer phenomena and validate the thermal model with fewer sources of uncertainty. This step was crucial for identifying and mitigating typical thermocouple measurement errors. In the second stage, the full welding of K-type thermocouple wires (chromel and alumel) was analyzed. A transient three-dimensional thermal model, including phase change, was developed and implemented using COMSOL Multiphysics®. To estimate the heat flux during welding, the nonlinear Function Specification Method was applied to the temperature data obtained from experiments. The study demonstrated that both the experimental design and the robustness of the thermal model significantly influence the accuracy of heat flux estimation. Using the estimated heat input and electrical energy delivered by the capacitor bank, the thermal efficiency of the process was calculated at 45%. Beyond enabling precise thermocouple attachment, the CDW process also served as a well-controlled case study for analyzing temperature measurement techniques and estimating heat flux in ultra-fast thermal events. The methods and findings from this research can be applied to improve thermal characterization in other manufacturing processes, such as micro-welding, additive manufacturing, and rapid thermal testing in the aerospace and automotive industries.

Key-words: Heat transfer. Inverse Problems. Function Specification Technique. Capacitor Discharge Welding. Thermocouples. COMSOL. Joule Effect.

Resumo

A medição de temperatura é fundamental em diversas aplicações da engenharia, especialmente em processos com altos gradientes térmicos e aquecimento rápido, como na soldagem. Dados precisos de temperatura são essenciais para o controle de qualidade, otimização de processos e garantia de segurança em operações industriais. No entanto, em processos rápidos e de alta energia, como a Soldagem por Descarga Capacitiva (CDW), a medição precisa da temperatura apresenta desafios significativos, principalmente devido à dificuldade de fixar termopares com baixa resistência térmica de contato e alta repetibilidade. Este trabalho apresenta uma análise do processo de fixação de termopares tipo K em superfícies metálicas utilizando um dispositivo de CDW desenvolvido sob medida. O desenvolvimento deste equipamento teve como objetivos superar a escassez de soluções comerciais adequadas, melhorar o contato térmico entre o termopar e a superfície metálica, e reduzir a resistência de contato, que afeta diretamente a precisão da medição de temperatura. Além disso, o projeto permitiu maior controle e compreensão dos parâmetros elétricos envolvidos, os quais foram integrados posteriormente à análise térmica. Métodos experimentais e numéricos foram utilizados ao longo do estudo. Na primeira etapa, uma configuração simplificada com um único fio de cromel foi utilizada para isolar os fenômenos de transferência de calor e validar o modelo térmico com menor incerteza. Essa etapa foi crucial para identificar e mitigar erros típicos de medição com termopares. Na segunda etapa, analisou-se a soldagem completa dos fios do termopar tipo K (cromel e alumel). Um modelo térmico transiente tridimensional com mudança de fase foi desenvolvido no COMSOL Multiphysics®. Para estimar o fluxo de calor durante a soldagem, aplicou-se o método não linear Function Specification Method aos dados de temperatura obtidos experimentalmente. O estudo demonstrou que tanto o projeto experimental quanto a robustez do modelo térmico influenciam significativamente na precisão da estimativa do fluxo de calor. Com base na energia térmica estimada e na energia elétrica fornecida pelos capacitores, foi calculada a eficiência térmica do processo em 45%. Além de permitir a fixação precisa de termopares, o processo de CDW serviu como estudo de caso bem controlado para a análise de técnicas de medição de temperatura e estimativa de fluxo de calor em eventos térmicos ultrarrápidos. Os métodos e resultados desta pesquisa podem ser aplicados para melhorar a caracterização térmica em outros processos de manufatura, como micro-soldagem, manufatura aditiva e testes térmicos rápidos nas indústrias aeroespacial e automotiva.

Palavras-chaves: Transferência de Calor. Problemas Inversos. Técnica da Função Especificada. Descarga Capacitiva. Termopares. COMSOL. Efeito Joule.

List of figures

Figure 2.1 – Junction of two dissimilars materials indicating the thermoelectric effect. 19
Figure 2.2 – Reference junction configuration and software compensation. 20
Figure 2.3 – Separated junction thermocouple configuration. 20
Figure 2.4 – Common issues in thermocouple measurements. 24
Figure 2.5 – Thermocouples installation. 24
Figure 2.6 – Projection welding by capacitor discharge. 26
Figure 2.7 – Main resistances in the capacitor discharge welding circuit. 28
Figure 2.8 – Projection welding in thermocouples using capacitor discharge. 29
Figure 2.9 – Structure of the inverse heat transfer problem. 32
Figure 3.1 – Discharge released melting one chromel wire. 37
Figure 3.2 – Discharge released fusing two wire. 38
Figure 3.3 – Comparison of Thermal Models 39
Figure 3.4 – Thermal model 40
Figure 3.5 – Properties over temperature 41
Figure 3.6 – Voltage distribution in circuit components. 43
Figure 3.7 – Comparison of the mesh refinements. 44
Figure 3.8 – Comparison of actual and estimated heat rates. 47
Figure 3.9 – Comparison of actual and estimated temperatures. 48
Figure 4.1 – Stages of the device presented in block diagram. 50
Figure 4.2 – Electrical design of voltage regulator. 50
Figure 4.3 – Electrical design for capacitor bank. 51
Figure 4.4 – Printed Circuit Board developed to simplify the assembly. 51
Figure 4.5 – Final assembled welding device. 52
Figure 4.6 – Schematic of the capacitor discharge welding system. 53
Figure 4.7 – Thermocouple wires joined by capacitor discharge welding. 54
Figure 4.8 – Electrical design for oscilloscope. 55
Figure 4.9 – Apparatus for measuring by oscilloscope. 56
Figure 4.10–Apparatus for measuring by data acquisition. 56
Figure 4.11–Simple voltage divider. 57
Figure 4.12–Electrical design data acquisition. 57
Figure 4.13–Capturing the flash of the electrical arc. 58
Figure 4.14–Capturing the silhouette of the metal. 59
Figure 4.15–Schematic representation of the experimental arrangement used to gather temperature measurements. 60
Figure 4.16–Measuring thermocouples positioning in relation to the tip of the welded thermocouple. 60

Figure 4.17–Measuring thermocouple wires fixed in different point. 61
Figure 4.18–Four-wire resistivity measurement setup. 62
Figure 4.19–Tubular furnace structure. 63
Figure 4.20–Square wave current signal used in the experiment. 64
Figure 4.21–Embedded samples after polishing process. 64
Figure 5.1 – Eletrical parameters obtained through the melting of chromel wire. . . 66
Figure 5.2 – Calculated power distribution during discharge. 67
Figure 5.3 – Time evolution of electrical parameters during the discharge. 68
Figure 5.4 – Power distribution during the welding of two thermocouple wires. . . . 69
Figure 5.5 – Process image over time melting one chromel wire. 70
Figure 5.6 – Process image over time joining two wires. 71
Figure 5.7 – Comparison between video and electrical measurements. 73
Figure 5.8 – Thermocouple wires fixed in different positions (Separated junction method) (right). Thermocouple wires fixed through the bead in the same position (left). 74
Figure 5.9 – Experimental temperatures measured by the 40 AWG (0.08 mm) thermocouples during the melting of the chromel wire (0.51 mm diameter), with 4 ms sampling interval. 76
Figure 5.10–Comparison between temperatures obtained by the two methods. . . . 77
Figure 5.11–30 AWG thermocouples positioning in relation to the tip of the 24 AWG thermocouple. 78
Figure 5.12–Experimental temperatures measured by the 30 AWG thermocouples during the welding process, in 90 ms reading time step. 79
Figure 5.13–40 AWG thermocouples positioning in relation to the tip of the 24 AWG thermocouple. 79
Figure 5.14–Experimental temperatures measured by the 40 AWG (0.08 mm) thermocouples during the welding process, in 4 ms reading time step. . . . 80
Figure 5.15–Comparison between temperature read in 90 ms time step and 4 ms time step. 80
Figure 5.16–Chromel resistivity temperature-dependent. 82
Figure 5.17–Second heating chromel. 82
Figure 5.18–Alumel resistivity temperature-dependent. 83
Figure 6.1 – Profile of the calculated heat flux. 87
Figure 6.2 – Thermal model representing the one wire melting. 88
Figure 6.3 – Bead position used in the thermal model. 89
Figure 6.4 – Comparison of bead temperature, surface temperature, experimental temperature. 89
Figure 6.5 – Thermal model 90

Figure 6.6 – Heat rate estimation using temperature measured in 90 ms reading time step, r=3. 91
Figure 6.7 – Comparison between experimental and estimated temperatures. 91
Figure 6.8 – Estimated heat rate without considering measuring thermocouple effect. 92
Figure 6.9 – Comparison between experimental and estimated temperatures, without the bead. 93
Figure 6.10–Thermal model 94
Figure 6.11–Resistor association. 95
Figure 6.12–[Heat rate estimation using temperature measured in 4 ms reading time step, with the bead. 96
Figure 6.13–Comparison between experimental and estimated temperatures, with the bead 97

List of tables

Table 5.1 – **Analysis of the compositions by EDS (Bead).** 84
Table 5.2 – **Statistical Analysis.** 84
Table 5.3 – **Analysis of the compositions by EDS (Alumel).** 85
Table 5.4 – **Analysis of the compositions by EDS (Chromel).** 85
Table 6.1 – **Comparison between estimation.** 98

Table of Contents

1 INTRODUCTION . . . 16
1.1 Justification . . . 17
1.2 Objectives . . . 17
1.3 Thesis Organization . . . 18

2 LITERATURE REVIEW . . . 19
2.1 Thermocouples Introduction . . . 19
2.2 Capacitor Discharge Welding . . . 25
2.3 Thermal modelling and Finite Elements Method for heat transfer problem . . . 29
2.4 Inverse heat transfer problems . . . 31
2.5 Summary of the Literature Review and Research Proposal . . . 34

3 NUMERICAL METHODOLOGY . . . 36
3.1 Defining steps . . . 36
3.1.1 Melting one wire analysis using static wire model . . . 36
3.1.2 Welding two wires analysis using static bead model . . . 37
3.2 Heat transfer equation . . . 38
3.2.1 Thermal Properties . . . 40
3.2.2 Joule effect equation . . . 42
3.3 Simulating and calculating (COMSOL) . . . 43
3.3.1 Mesh . . . 43
3.4 Inverse heat transfer problem . . . 45
3.4.1 Validation of the proposed method . . . 46

4 EXPERIMENTAL PROCEDURES . . . 49
4.1 Capacitor Welding Device . . . 49
4.2 Capacitor Discharge Welding Process . . . 52
4.3 Measuring electrical quantities during the process using the oscilloscope . . . 54
4.4 Measuring electrical quantities during the process using the data acquisition . . . 55
4.5 Capturing the images during the bead formation . . . 57
4.6 Obtaining temperature data during the welding . . . 58
4.7 Resistivity Measurements . . . 61
4.8 Elemental Composition Evaluation . . . 63

5 EXPERIMENTAL RESULTS . . . 66
5.1 Electrical quantities obtained of the one wire melting . . . 66
5.1.1 Thermocouples welding (40V) . . . 67
5.2 Shape over time . . . 68
5.3 Discharge Time . . . 72
5.4 Temperature During Melting of a Single Chromel Wire . . . 74
5.5 Experimental temperature welding thermocouples . . . 76
5.5.1 90 ms reading time step using 30 AWG (0.254 mm) measuring thermocouples 77
5.5.2 4 ms interval reading using 40 AWG measuring thermocouples . . . 78
5.5.3 Comparison . . . 78
5.6 Resistivity Measurements Results . . . 81
5.7 Energy Dispersive Spectroscopy results . . . 84

6 HEAT TRANSFER MODEL RESULTS . . . 86
6.1 Heat transfer in single chromel wire . . . 86
6.2 Heat transfer in two thermocouple wires . . . 89
6.2.1 Estimating using the 90 ms reading time step experiments . . . 90
6.2.2 Estimating using the 4 ms reading time step experiments . . . 91
6.3 Two thermocouple wires with Joule Effect and measuring bead . . . 94
6.3.1 Estimating using two thermocouple wires with measuring bead . . . 94
6.4 Comparison between the solutions . . . 95
6.5 Thermal efficiency . . . 98

7 CONCLUSION AND PERSPECTIVES . . . 99
7.1 Perspectives . . . 100

REFERENCES . . . 102

1 Introduction

Temperature is one of the most frequently measured physical quantities in science and engineering. Knowing the temperature is essential for the proper functioning of several systems, ranging from the human body to automotive engines, power plant turbines, and laboratory equipment. Often, temperature serves as a warning signal: it can indicate a fever, brake wear, or even overheating in industrial components. In various applications, thermal monitoring directly contributes to preventing failures, reducing wear, and ensuring the safe and efficient operation of equipment. To achieve this, it is crucial that the sensors used exhibit low uncertainty and high reliability.

Thermocouples, due to their simplicity, low cost, and robustness, are widely used as temperature sensors, including in highly complex industrial environments. However, accurate surface temperature measurement using thermocouples still presents significant challenges. Issues such as wire oxidation, poor attachment, hysteresis-induced calibration drift, reference junction compensation errors, and incorrect thermocouple type selection in the acquisition system are common sources of uncertainty. When it comes to temperature measurement on metallic surfaces using thermocouples, the quality of the thermal contact between the thermocouple and the surface, as well as the bead geometry, has a significant impact on the accuracy of the resulting data. The thermal contact resistance between the sensor and the surface influences both the velocity and accuracy of the measurement. Although it is possible to position the sensor by simple contact, this practice can result in high thermal resistance and delay the local thermal equilibrium, thereby compromising the data obtained.

The positioning of the thermocouple can also alter the physics of the thermal problem being studied. In many cases, the thermocouple wires act as small fins, dissipating heat to the environment and introducing a disturbance in the local thermal field. This influence must be taken into account, especially when experimental data are used as the basis for thermal model calculations and inverse heat transfer problems.

Given this context, this work proposes the use of a CDW (*Capacitor Discharge Welding*) as a method for thermocouple attachment. This process involves releasing a pulse of electrical energy from a capacitor bank, enabling a fast and effective attachment with good thermal conduction and high repeatability. This technique, in addition to minimize the thermal contact resistance, improves the quality of the measurements, especially in environments with high rates of thermal variation, such as welding processes. Furthermore, this work investigates the effects of temperature measurement errors with thermocouples on the estimation of heat flux in capacitor discharge welding processes, through the integration of experiments, thermal modeling, and inverse problem-solving techniques.

1.1 Justification

The thermal characterization of welding processes is essential for quality control and the development of new technologies in the manufacturing industry. However, short-duration and high-energy processes, such as capacitor discharge welding, present challenges for both temperature measurement and modeling. Although thermocouples are widely used, their application is subject to uncertainties related to attachment methods, dynamic response, and interaction with the surrounding environment, which may compromise the reliability of experimental data.

In this context, the proposed work is justified by the need to understand and quantify the effects of measurement errors, specially on heat flux estimation through inverse problem techniques. The approach is innovative in combining an emerging thermocouple attachment method, capacitor discharge welding, with numerical modeling and sensitivity analysis of inverse problems, thus contributing to advancements in both experimental instrumentation and thermal modeling.

Furthermore, the implementation of capacitor discharge welding technology in the heat transfer laboratory enhances the efficiency, accuracy, and repeatability of thermal sensor attachment. This is an improvement for the experimental research in heat transfer conducted at the institution.

1.2 Objectives

To achieve the main objective of investigating the effects of temperature measurement errors with thermocouples, particularly on heat flux estimation in capacitor discharge welding processes, this work is guided by the following specific objectives:

- Implement and experimentally adapt the capacitor discharge welding process for thermocouple attachment in the Heat Transfer Laboratory (LabTC) at UNIFEI, ensuring good thermal contact and repeatability for temperature measurements.
- Evaluate the influence of different sources of error in thermocouple temperature measurements, especially under rapid thermal variation conditions, and analyze their impact on experimental data accuracy.
- Develop and validate thermal models for the capacitor discharge welding process, integrating experimental data and applying inverse problem techniques to estimate heat rate.

- Analyze the sensitivity of inverse problem results to measurement errors and propose improvements in both temperature acquisition methods and thermal modeling strategies for rapid processes.

1.3 Thesis Organization

In Chapter 2 of this work, the concept of temperature measurement using thermocouples is introduced, as well as the challenges encountered with this method. Additionally, studies addressing the method of capacitor discharge welding are presented. Furthermore, studies those utilized thermal modeling and finite element methods to analyze heat transfer problems in various processes are also discussed. Finally, the concept of inverse problems, their challenges, and studies that used these methods for parameter and thermal property estimation are presented.

Chapter 3 describes the numerical model used for the capacitor discharge welding process. The thermophysical properties and parameters of the thermal model are presented. Additionally, the calculations used for the inclusion of the Joule effect in the model are shown.

A description of the experimental methodology is presented in Chapter 4. This chapter outlines the experimental approaches for obtaining electrical parameters and temperature measurements during the studied process.

Chapter 5 presents the experimental results obtained for the studied case. A detailed analysis of the influence of the thermocouple weld bead on temperature measurements is conducted.

Chapter 6 presents the numerical results obtained for the studied case. A detailed analysis of the influence of the thermocouple weld bead on the calculated temperatures is conducted. Additionally, the results obtained from estimations, using inverse problems are presented, highlighting the influence of a good thermal model and experiments on the approach to inverse problems.

Finally, Chapter 7 presents a conclusion on the study conducted in this work and suggestions for future research that could continue this topic.

2 Literature review

2.1 Thermocouples Introduction

The most common electrical method for temperature measurement uses the thermocouple [1]. The thermocouple is a popular sensor due to its relatively low cost, interchangeability, wide measurement range and reliability. When two different metals are joined, as shown in Figure 2.1, there will be a potential difference, dependent on the temperature of the junction, between the wire ends, A and B. This phenomenon is known as the Seebeck effect. In addition to the Seebeck effect, two more phenomena are present in the thermoelectric circuit: the Peltier effect and the Thomson effect. The first is related to the temperature variation at the wire junction due to the electric current flowing through the system. Meanwhile, the Thomson effect is the changes in the potential difference based on the temperature gradient along the wires. As the thermocouples are insulated, Peltier and Thomson are neglected in this work.

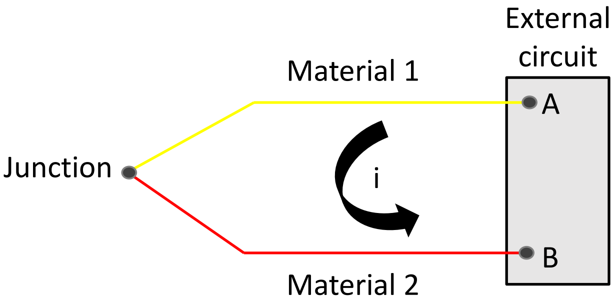

Figure 2.1 – Junction of two dissimilars materials indicating the thermoelectric effect (adapted from Holman [1]).

One problem may exist while you try to measure the voltage in A and B, when you connect the thermocouple at the hardware, another thermal EMF (*electromotive force*) is generated at the junction, it may be the cause of significant errors in this method, so it is important to take account. To make an absolute measurement, the thermocouple must be referenced to a known temperature at the other end of the sensor leads. In the past, to establish the reference temperature, an arrangement with a mixture in equilibrium of ice and distilled water was used, producing a known temperature of 0 °C (32 °F). However, as this is inconvenient to transport, the software compensation method requires only an additional sensor for direct temperature reading, such as a thermistor or a silicon sensor, to measure the temperature of the isothermal block of the reference junction, the set is shown in Figure 2.2. Software is then used to calculate the equivalent voltage of the reference temperature, either using polynomial equations or through tables, for the corresponding type of thermocouple. Once calculated, this value is added to the measured output voltage at the thermocouple. The resulting voltage is then converted back to a temperature that represents the actual temperature of the thermocouple.

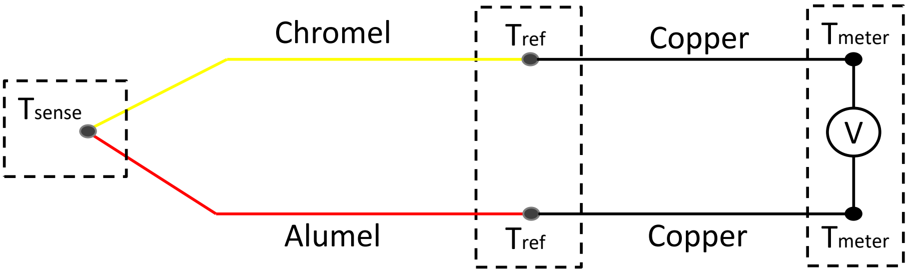

Figure 2.2 – Schematic of the reference junction configuration using software compensation.

The EMF between two different materials, considering a reference temperature as shown in Figure 2.2, can be determined using Equation 2.1:

$$\begin{aligned}\epsilon_{meter} &= \int_{T_{sense}}^{T_{ref}} \epsilon_{chromel}\, dT + \int_{T_{ref}}^{T_{meter}} \epsilon_{copper}\, dT + \int_{T_{meter}}^{T_{ref}} \epsilon_{copper}\, dT + \int_{T_{ref}}^{T_{sense}} \epsilon_{alumel}\, dT \\ \epsilon_{meter} &= \int_{T_{sense}}^{T_{ref}} \epsilon_{chromel}\, dT + \int_{T_{ref}}^{T_{sense}} \epsilon_{alumel}\, dT\end{aligned} \tag{2.1}$$

Another technique used for measuring temperature is the separated junction method. In this case, two thermocouple leads are attached to two different points of the sample, where the metallic surface completes the thermoelectric circuit, as shown in Figure 2.3.

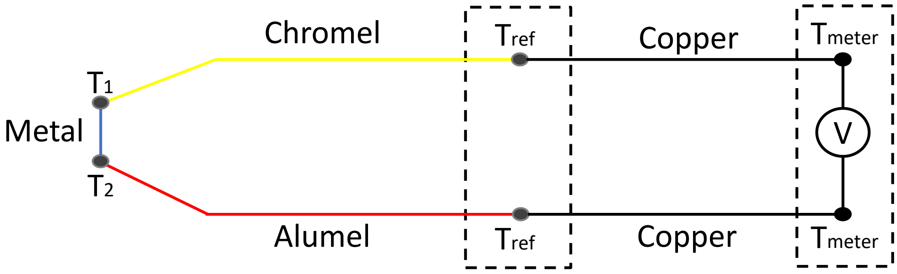

Figure 2.3 – Schematic representation of the separated junction thermocouple configuration.

In this setup, the weld bead inertia effect is minimized, as it is possible to attach the wires directly to the surface. However, a new error is introduced since the temperature measurement will be the average of two contact points. In this case, the EMF can be defined by Equation 2.2:

$$\epsilon_{meter} = \int_{T_1}^{T_{ref}} \epsilon_{chromel}\, dT + \int_{T_{ref}}^{T_2} \epsilon_{alumel}\, dT + \int_{T_2}^{T_1} \epsilon_{metal}\, dT \tag{2.2}$$

If there is no temperature difference between T_1 and T_2, then there is no EMF contributed by that conductor. Thus, T_1 to T_2 can be considered as T_{sense} and calculated as shown in Equation 2.1. This principle is known as the thermocouple law of intermediate metals.

Despite the simplicity, low cost, and effectiveness of the method, there are some problems that may occur, such as: oxidation issues or failures in the fixing of thermocouples, leading to errors in the calibration curve; Decalibration due to operation outside the applicable temperature ranges (hysteresis problem); Error in the compensation of the reference junction; Incorrect selection of the thermocouple type in data acquisition.

The complexity of the surface where the temperature will be measured can also be a challenge. Often, the surface does not align with the model used to describe it, due to roughness, chemical properties, and even the presence of oxide layers. This complexity is heightened in porous materials, such as insulators and wood. Moreover, in contact methods, like the one described, achieving thermal equilibrium between the sensor and the particles quickly is important, emphasizing the importance of good contact for effective interaction. For obtaining the surface temperature of a specific point, the measured volume needs to be small enough to represent the point on the surface but sufficiently large to contain an adequate number of particles. When the objective is the measurements of temperature variation, the sensor must have characteristics that enables the surface element to reach equilibrium in a short enough time so that temperature variations during the equilibrium process are insignificant. In other words, the interaction between the thermocouple and the surface needs to achieve equilibrium within a time frame shorter than the desired interval, thus defining the device inertia with a characteristic time, known as the time constant or response time.

The response time, according to the International Vocabulary of Basic and General Terms in Metrology published by ISO (similar to standard NF X 07-001), is the interval between the specified sudden change in the input signal and the moment when the output signal reaches, within specified limits, its final value in the steady state and remains there. In control theory, the response time (τ) corresponds to the time it takes for a system to reach $1 - \frac{1}{e} = 0.632$ of its limit value after a step disturbance. The term "thermal equilibrium time"refers to the time it takes for the measuring instrument to reach a generally high fraction of the final value, which theoretically would only be reached at an infinite time, for example, $\tau_{0.98} = 4\tau_{0.632}$. Just like accuracy, the response time strongly depends on the assembly of the thermometric device, as the thermal equilibrium between the sensor and the studied environment is influenced by thermal exchanges depending on the sensor, environment, and sensor-environment interface. The overall response time is important, and the thermometer response time should be small compared to the rate of temperature change of the observed phenomenon. Shorter response times are achieved with sensors having high thermal diffusivity and a large exchange surface.

Beyond the contact resistance between the sensor and the surface, the response time of thermocouples also depends on the size of the junction; the smaller the junction, the faster the response time. For instance, junctions with a thickness of up to 0.1 mm encapsulated by a polymer glass laminate will measure temperatures within the range of 5 ms [1].

Michalski *et al.* [2] examined the uncertainty of temperature measurements using K-type thermocouples. The study involved calibrating the thermocouples and collecting data to statistically compare measured temperatures with actual values. The results indicated that temperature corrections did not exceed 0.6°C, with the highest correction value being 0.704°C at 50°C within the 0°C to 100°C range. They concluded that this method effectively estimated the uncertainty of temperature measurements in research on flow boiling heat transfer in minichannels. kee *et al.* [3] investigated the uncertainty in temperature measurements using thermocouples by addressing errors from reference junction compensation and data fluctuations. They also explored the limitations of the data acquisition device and errors in converting voltage measurements to temperature. The findings showed an uncertainty of 0.42°C for a K-type thermocouple. Kee *et al.* [3] concluded that the measured temperature uncertainty was less than that reported by the thermocouple manufacturer and recommended the use of an ice-water bath in research settings. Both studies focused on steady-state conditions, where the influence of the thermocouple bead on measurement errors is minimal. In contrast, the present work explores a transient analysis, where temperature changes are affected by the inertia of the thermocouple welded bead. Research on temperature measurement in transient state using thermocouples has shown that high temperature gradients introduce bias errors, particularly with embedded sensors ([4], [5]). In the study by Wooley *et al.* [4], differences between the tip temperature and the junction temperature exceeded 20°C, representing more than a 12.5% discrepancy in measured temperatures at that time.

In this context, some problems must be considered when the temperature is measured using thermocouple:

- The measured temperature corresponds to be the bead temperature rather than directly to that of the plate, as illustrated by T_1, T_2 and T_3 in Figure 2.4. A transient approach is presented by Woolley *et al.* [4], where the authors address bias errors caused by temperature measurement inaccuracies using thermocouples. They examined the challenge of determining the exact location where the thermocouple measures the temperature. To identify this location, they created a three-dimensional model of the thermocouple wires and their welded bead. Infrared thermal imaging was employed to experimentally validate the location at which the thermocouple measures. The authors concluded that the temperature is measured at the interface between the wire and the welded bead.

- The imperfections between the bead and the sample surface can generate a contact resistance, sometimes leading to relevant discrepancies between the sample temperature and the temperature collected in the wires, Figure 2.4.
- The high temperatures experienced during bead formation can cause oxidation or changing mechanical characteristics, which may affect the thermocouples calibration, Figure 2.4. Abdelaziz *et al.* [6] subjected K-type and N-type thermocouples to thermal exposure periods at maximum temperatures to investigate stability. Using SEM (*Scanning Electron Microscopy*) and EDX (*energy-dispersive X-ray*) analysis, they monitored changes in the crystalline structure and chemical composition of thermocouple wires after each stage of thermal exposure, assessing the changes in thermoelectric properties. Results showed that N-type thermocouples are more stable at high temperatures (up to 1050 °C) even after 1200 hours of use, while type K thermocouples presented rapid drift and failed after 600 hours due to severe corrosion. Microstructural analysis indicated that contamination of the Alumel and Nicrosil thermoelements is a main cause of thermal drift in type K and N thermocouples, respectively.

The installation of thermocouples must be executed carefully. Thermocouples measure the temperature at the last point of electrical contact between the two wires [1]. In Figure 2.5a, only the bead makes contact with the plate, meaning it measures the temperature in the region where bead is fixed. Figure 2.5b presents the contact of the wires at two points on the plate, therefore, if a temperature gradient exists on the plate, the potential difference will indicate the average temperature between these two points. Figure 2.5c shows a common error in thermocouple application, where the wires make contact outside the plate. Consequently, as the thermocouple signal corresponds to the shortest electrical path, the measured point will be the wires rather than the actual surface temperature of the plate.

Therefore, when considering the use of thermocouples for surface temperature measurement, it is extremely important to take into account the contact resistance between

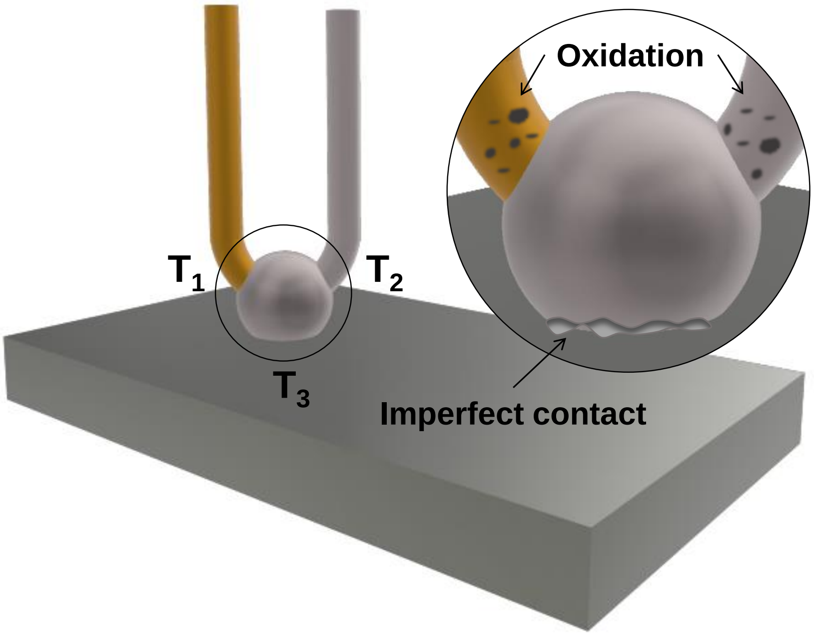

Figure 2.4 – Illustration of common issues in thermocouple temperature measurements.

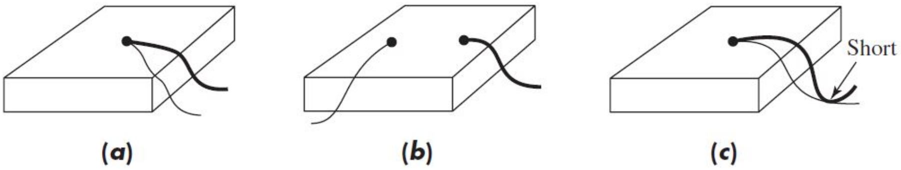

(*a*) (*b*) (*c*)

Figure 2.5 – (a) Only the welded joint in contact with the plate. (b) Contact at two points. (c) Contact at the welded joint and along the wires.(adapted from Holman [1])

the thermocouple and the measured surface. While measurements can be performed by simply making contact between the thermocouple and the desired region, the thermal contact resistance, in this case, will be high enough to result in an extremely slow thermal equilibrium between them. In other words, for an effective interaction between the surface and the thermocouple, imperfections related to contact resistance must be minimized. This justifies the importance of employing effective methods for thermocouple fixation.

Difficulties for fixing thermoucouple in metallic surface are presented in the literature. In the 1990s, Tsai *et al.* [7] investigated the insufficient control of spot welding parameters. They presented an expansion-based control algorithm for real-time spot welding, simulating the process through Finite Element analysis to establish the correlation between material expansion and weld quality. The authors observed that surface temperature data could be related to the maximum temperature at the nugget center throughout the process. However, they presented challenges associated to the attachment of thermocouples for collecting that temperatures.

In this work, CDW is proposed as a method to fix thermocouple to minimize thermal contact resistance and also it is used as a heat source for performing experiments to obtain temperature data. Details on this method are provided in the next chapter.

2.2 Capacitor Discharge Welding

One effective way to fix thermocouples onto metallic surfaces is through the CDW method. The process involves the application of an energy pulse by releasing the electric charge stored in a capacitor bank. This method offers several advantages compared to other welding techniques. Since it is an extremely fast process duration (ranging from 8 to 20 milliseconds, as reported by Wang *et al.* [8]), the HAZ (*Heat-Affected Zone*) is narrow, ensuring good material continuity and minimizing stress concentration effects in the welded area. As previously discussed, maintaining the thermocouples properties is essential for accurate measurements. Furthermore, preserving the integrity of the observed surface is critical for reliable temperature data acquisition. Additionally, this type of welding can be performed near heat-sensitive areas, such as seals between glass and metal or explosive composites.

Within the category of welding processes using electrical energy sources, CDW can be classified as both resistance welding (spot or projection welding) and arc welding (when plasma is involved in the process). One of the earliest studies involving CDW was conducted by Wilson *et al.* [9], who investigated the plasma jet present during the welding of Fe3Al solid cylinders.

Examples of spot welding using the capacitor discharge method include those presented by Zhou *et al.* [10], who applied CDW to join aluminum, brass, and copper sheets. Gould *et al.* [11] examined the resistance spot welding of aluminum sheets, comparing CDW with polarity-switching to MFDC (*medium-frequency direct current*) welding. They found that polarity-switching CDW achieved tensile shear strengths approximately 500 N higher than MFDC welds. Despite the different failure mechanisms, CDW welds failing by nugget shear and MFDC welds by button pull-out, the CDW process demonstrated superior tensile shear strength, likely due to reduced softening in the HAZ associated with its shorter thermal cycles. Transverse tensile tests showed similar results, with CDW outperforming MFDC in tensile shear strength.

Projection welding using the capacitor discharge method is commonly applied in pin welding, as illustrated in the schematic in Figure 2.6. In this setup, two pins with a guiding tip are pressed together by clamps connected to the anode and cathode of the capacitor bank. During capacitor discharge, heat is concentrated at the interface between the pins, where fusion occurs. Chiozzi *et al.* [12] utilized this technique to join bars made of Inconel 718 and Titanium TiAl6V4 superalloys, demonstrating its potential for repairing damaged components without replacing the entire assembly or requiring additional machining. Cao *et al.* [13] investigated CDW in the projection welding of M8 flanged hexagonal nuts. They conducted pullout tests, microstructural analysis, and fracture examinations after welding under different voltages. The authors concluded that welding voltage significantly affects the mechanical strength and weld nugget size. They also proposed a criterion for calculating the minimum nugget diameter required to ensure pullout fracture in projection welds for nuts. Lienert *et al.* [14] applied CDW for projection welding in nuclear reactor components made of 14YWT nano-ferritic alloy. Beyond pins and nuts, projection welding using CDW has been proposed by Wang *et al.* [8] for joining wire meshes in hollow structures of nickel-based alloy turbines.

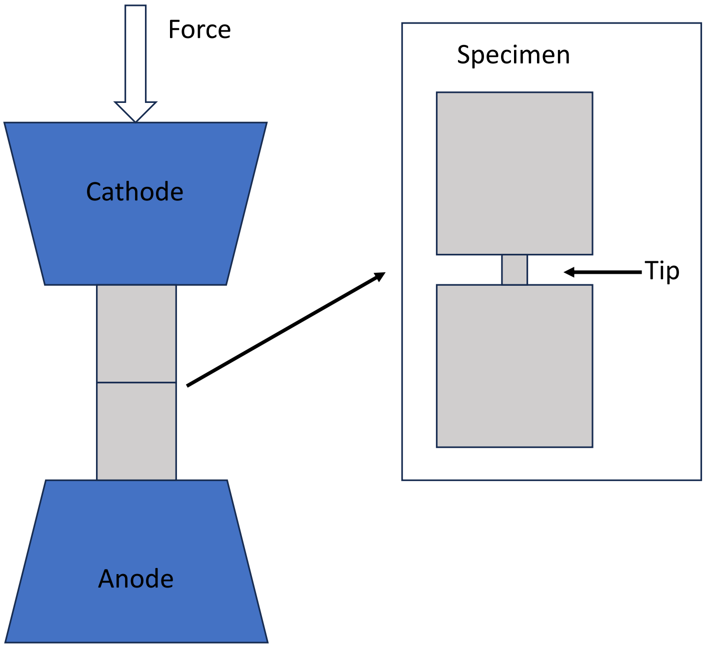

Figure 2.6 – Schematic representation of projection welding using the capacitor discharge method.

Some studies have explored the use of CDW to preserve material characteristics and prevent oxidation in the welded area. Chiozzi *et al.* [12] examined the mechanical behavior of joints welded by CDW. This technique enables the repair of damaged parts without the need to replace the entire component or perform additional machining. To analyze the HAZ, the microstructure was examined using optical microscopy and SEM, with pure argon serving as a shielding gas to reduce oxidation. The results showed good durability of weld spot compared to the base metal, although the welded joints exhibited some brittleness. Verástegui *et al.* [15] explored the CDW process in three types of steel. The welding apparatus included 12 electrolytic capacitors operating at 80 V with a capacitance of 10 mF, used to weld pins onto a base plate. Their findings indicate that the process produced a narrow HAZ with a martensitic microstructure. The rapid cooling rate led to a brittle joint, likely due to martensite formation. The authors concluded that HAZ size increases with welding energy, and hardness is correlated with the equivalent carbon content. Lienert *et al.* [14] studied ways to extend the lifespan of nuclear reactor components, proposing nanoferritic alloys containing nano-oxides. Preserving the oxide structure during joining is critical for this application, so they recommended resistance projection welding using CDW. They found that welding energy had a greater impact on the process than applied force, successfully joining the materials while retaining the original microstructures and material properties.

One of the main challenges when studying electrical parameters in the welding process is defining the resistance in the arc welding region. This resistance is transient: at the start of the process, when the electrode contacts the wires, the resistance is nearly zero. As the process advances and the electrode moves away from the wires, the arc welding resistance increases. This variation in resistance causes fluctuations in the electrical current. In the case of capacitor discharge, the supply voltage also varies due to the gradual discharge of the capacitors throughout the process. These fluctuations cause the power applied in the welding arc to be unstable. Figure 2.7 shows the distribution scheme of the resistances in the welding circuit. The welding circuit is approximated by a resistor-capacitor circuit, where the capacitor bank is responsible for storing energy. The resistances in the circuit include: the resistance of the connecting wires between the capacitor bank and the welding process, the resistances of the thermocouple wires, the electrode resistance, and, primarily, the arc welding resistance, which is the most significant for this study. The resistances of the electrode and connecting wires are ignored in this case due to their low influence on the circuit.

The polarity of the electrode and thermocouples is also an important factor during the welding process. The CDW process resembles TIG (*Tungsten Inert Gas*) welding, as it involves a non-consumable electrode. Wilson *et al.* [9] analyzed the CDW process using high-speed photography and Finite Element analysis software to model heat flux within the process. Their results revealed that the cathode plasma jet was responsible for expelling material from the anode. The uneven heating of the anode and cathode was attributed to the heat transfer from the anode to the expelled metal particles. The authors concluded that weld metal spatter is not caused by electrode contact extrusion but rather by plasma jet expulsion during the arc phase. Additionally, the arc propagation at ignition is rapid enough to characterize the CDW process as essentially one-dimensional. Based on these findings, it can be concluded that when the positive pole is connected to the thermocouple and the negative pole to the electrode, as represented in Figure 2.7, the thermocouple wires will not be contaminated by the electrode. In the opposite case

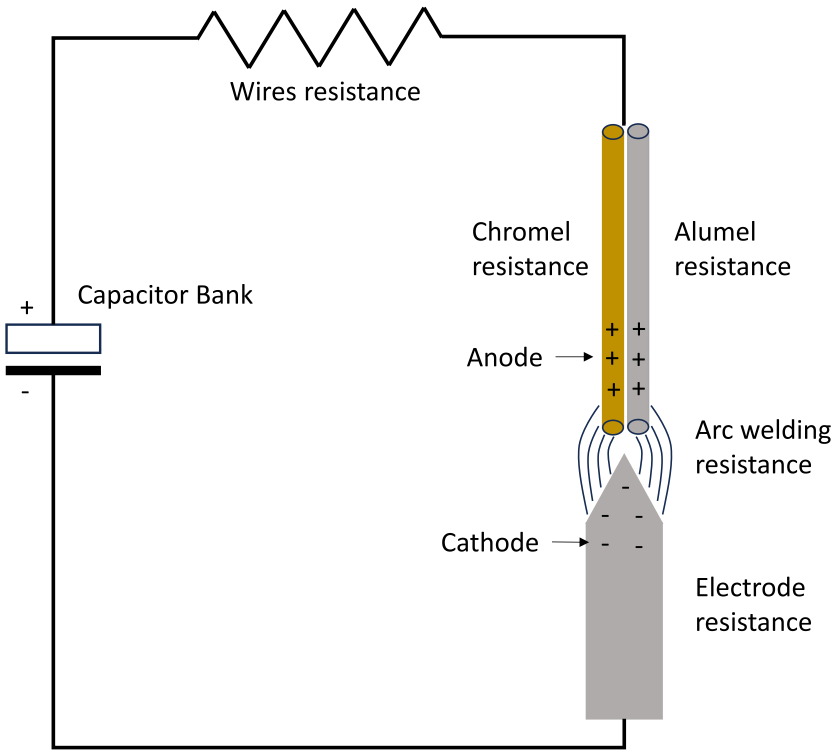

Figure 2.7 – Schematic representation of the main electrical resistances involved in the capacitor discharge welding circuit.

(electrode on the positive pole), the electrode heats up, transferring material towards the thermocouples.

Two categories of capacitor discharge welding are considered in this work. The first involves the use of plasma and welding arcs, as illustrated in Figure 2.7, to form the junction between chromel and alumel wires. The second employs projection welding to attach thermocouples onto surfaces where temperatures will be monitored. A schematic of the projection welding process is shown in Figure 2.8. In this setup, an electrode (typically tungsten or another conductive metal) is connected to the anode of the capacitor bank, while the surface to be welded is polarized with the cathode. The electrode is positioned on the upper surface of the bead, maintaining contact between the bead and the surface. The capacitors are then discharged, generating heat at the interface between the bead and the surface, thereby welding the two components together.

The CDW process for thermocouples involves multiple physical phenomena, including fluid mechanics, heat transfer, electrical, materials, and electromagnetic challenges. In this study, the heat transfer problem in the thermocouple wires during welding will be the focus of analysis. The electrical parameters of the CDW process will be used to define the heat generation rate, which will then be applied in the thermal model.

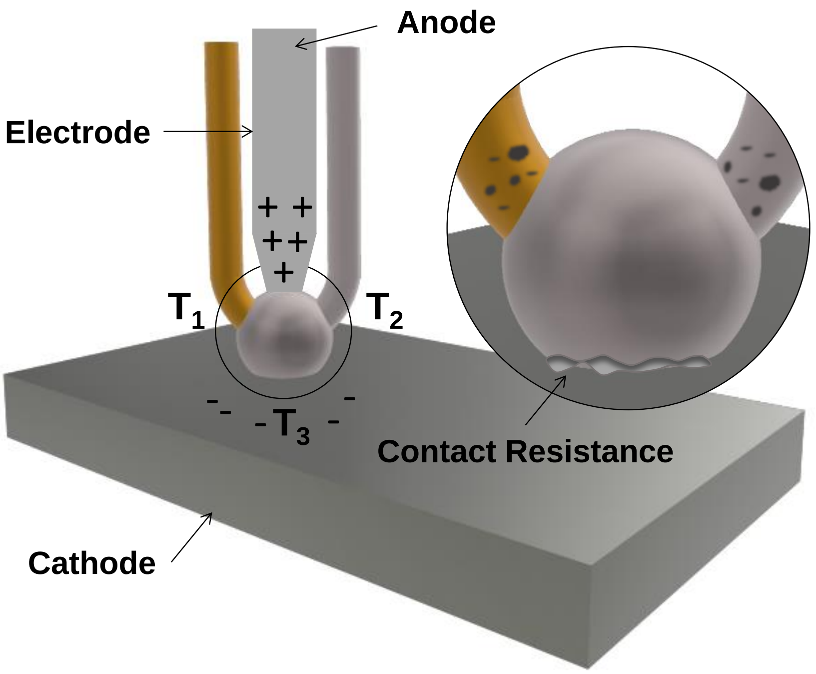

Figure 2.8 – Schematic of the projection welding process applied to thermocouples using capacitor discharge.

2.3 Thermal modelling and Finite Elements Method for heat transfer problem

Thermal modeling is a valuable approach for analyzing mechanical processes, especially those involving rapid thermal transients, such as welding. Accurate prediction of temperature distribution is essential, as thermal input directly affects microstructural evolution, material properties, and overall process efficiency. However, in welding applications, modeling becomes particularly challenging due to the non-linear behavior of material properties at high temperatures, the presence of fluid dynamics, and complex boundary conditions.

In this work, the thermal modeling focuses on the temperature field of the thermocouples during a capacitor discharge welding process. The objective is to determine the heat rate and the temperature field generated by the capacitor discharge and analyze the influence of parameters such as heat rate and efficiency of the process. To achieve this, the FEM (*Finite Element Method*), implemented via COMSOL Multiphysics®, is employed due to its capability to solve transient, non-linear heat transfer problems with geometric and physical fidelity.

The use of FEM in thermal welding simulations is well established in the literature. Carbone and Langella [16] used COMSOL to model the resistance welding of thermoplastic composites, showing that while the temperature field had limited sensitivity to temperature-dependent thermal conductivity, the melting time was highly dependent on the applied power density. This highlights the importance of accurately defining the thermal input to predict phase change behavior.

In spot welding applications, the geometry and material properties at the contact interface are critical. Sallem *et al.* [17] investigated the formation of weld nuggets in resistance spot welding and showed that the electrode-plate contact area significantly affects heat generation, requiring higher currents as the contact area increases. Similarly, Vural [18] used FEM simulations in ANSYS to correlate welding parameters with nugget formation and mechanical separation. His results demonstrated a 10% discrepancy between simulated and experimental weld bead heights, reinforcing the need for accurate thermal modeling when determining optimal welding parameters.

Zammar *et al.* [19] highlighted how FEM can be used as an effective alternative when experimental measurements are difficult, particularly in the manufacturing of thermoplastic composites. Their three-dimensional thermal model achieved errors below 10% when compared to experimental results, validating its use for process parameter optimization.

Beyond classical welding, modeling efforts have also extended to encapsulated systems with complex thermal interfaces. Jain and Parhizi [20], for example, proposed a model to predict phase change behavior in encapsulated materials, accounting for interfacial thermal contact resistance and convective boundary conditions. Their work highlights how advanced modeling can provide predictive capability where direct measurement is impractical.

Despite these advances, estimating the actual thermal input remains a critical challenge, especially in processes like capacitor discharge welding where the timescales are extremely short and the heat flux is difficult to measure directly. To address this, inverse heat transfer techniques can be integrated with thermal modeling to estimate the heat rate based on temperature measurements. This approach is particularly useful in experimental setups involving thermocouples, where errors due to contact resistance and sensor dynamics must be carefully considered. By combining FEM with inverse analysis techniques, this study aims to improve the understanding of heat transfer during thermocouple welding and support the development of more accurate temperature acquisition systems for high-speed thermal processes.

2.4 Inverse heat transfer problems

In general, a problem is said to be inverse if we seek input data of a physical problem from its output data. To understand the concept of inverse problems, it is necessary to first grasp the concept of well-posed problems, as defined by Hadamard [21], these correspond to problems that satisfy the following conditions:

- There must exist a solution;
- The solution must be unique;
- The solution must continuously depend on the input data or initial and boundary conditions.

The stability of the solution must be observed concerning a perturbation in the system observable. In practice, this corresponds to noise in a temperature measurement. This noise is not present in the observable resulting from modeling, leading to a difference and resulting in an error in the estimation. In certain cases, noise in the measurement causes amplified noise in the unknown and hinders the resolution of the inverse problem [22].

Any physical problem that does not satisfy at least one of these conditions is considered an ill-posed problem. The inverse problem is a class of ill-posed problems in which the condition of solution stability is generally not met, because some part of the function is unknown. Therefore, additional data, such as temperature response within the domain obtained through experiments, is required. Data errors, such as delays in response time caused by thermocouples measuring the temperature of their bead rather than the surface, undermine the stability of the solution, making the problem ill-posed. However, there are certain methods to restore a well-posed nature to a problem that does not meet one of the aforementioned conditions. Regularization is the tool that transforms an ill-posed problem into a well-posed problem, ensuring that the solution approximates the original problem. For example, Tikhonov regularization is a method of regularization of ill-posed problems that can be used to solve the problem of multicollinearity in linear regression, which commonly occurs in models with large numbers of parameters [23], [24]. This method is a valuable tool to estimate multiple parameters simultaneously. There are other regularization methods, however, they require a specific formulation of the inverse problem. For example, the Sequential Function Specification Method [25], in which the reduction of a quadratic criterion is carried out at each time step using information from future times.

In experimental heat transfer, the measured data such as temperature, heat flux, or electrical quantities, is collected to deduce other parameters like heat flux, emissivity, diffusivity, or even temperature in specific regions, shown in the orange section of Figure 2.9. In these cases, a model can be constructed for correlating input parameters with the measured quantities, facilitating the study of the effects of several causes. When this model aligns with the experimental process, proceeding from cause to effect rather than the inverse, it is called the forward model, shown in the yellow part of Figure 2.9. A forward problem is the commonly considered issue, where the governing equation and material properties are known. In such case, the analyst task is to calculate the values of the field variables. On the other hand, the inverse problem uses measured data to estimate parameters, moving from the effect to cause. In the studied model, causes include initial and boundary conditions, thermal properties, heat rate and geometric characteristics, while the effect is observed temperature data over time.

The operation of the inverse problem is based on comparing measured data to data calculated by the model. The optimization function aims to minimize the difference between these data by changing input values (causes), as shown in the blue section of Figure 2.9. Additionally, it is also possible to apply an inverse method to define an optimal experiment. This can be applied to estimate parameters and assist in determining the best position for measurement points, as shown in the "design of experiments"pathway in Figure 2.9.

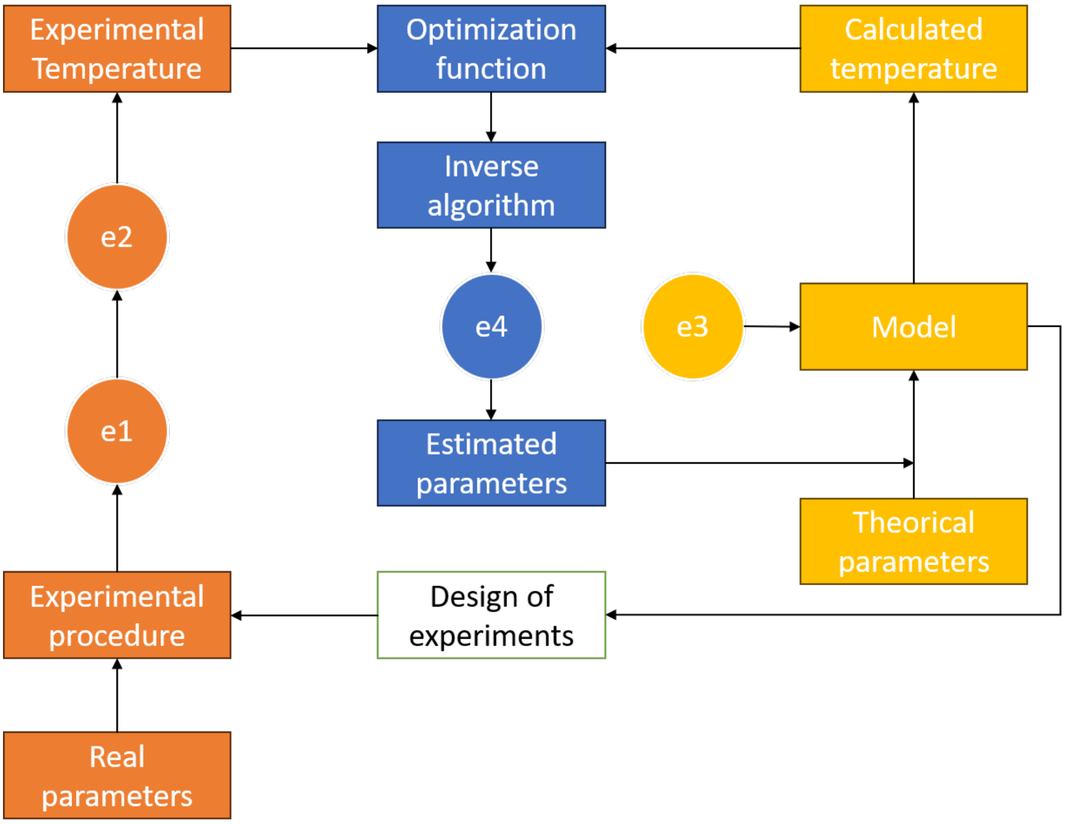

Figure 2.9 – Schematic representation of the inverse heat transfer problem and its associated errors.

The error between the estimated numerical data and the experimentally measured data represents the confidence in the application of the inverse problem (represented as e4 in Figure 2.9). This error may also be associated with the model inadequacy in faithfully representing the physical problem (represented as e3 in Figure 2.9), and finally, errors in experimental measurements (system measurement noise, thermocouple response time delay), represented as e1 and e2 in Figure 2.9.

In welding and other manufacturing processes, it is often desired to determine the temperature or heat-flux on the surface [26]. Frequently, the temperature is in inaccessible regions, and thermal properties of materials are unknown, or the heat rate during a mechanical process is desired. In such cases, inverse problems may be applied to estimate unknown parameters [27], particularly when satisfactory results cannot be obtained through experiments alone. These estimations are typically based on experimentally measured temperature data within a specific domain. One of the pioneering studies on inverse heat transfer problems was presented by Stolz [28]. He developed a method for assessing the heat flux on spherical surfaces during the quenching procedure. To address the noise present in Stolz's temperature data [28], the Function Specification Method was proposed by Beck *et al.* [25]. This method offers robustness to data noise and does not require extensive computational time.

Chen *et al.* [29] compared the effectiveness of the inverse problem techniques WDFSM (*Whole-Domain Function Specification*) and SFSM (*Sequential Function Specification Method*) in a transient model of conjugate heat transfer of forced laminar convection in a circular tube. The techniques were used to estimate the inlet temperature and heat flux on the outer wall of the tube based on measured temperatures inside the tube. The authors concluded that both presented methods were effective in solving this type of problem. Although both methods yield accurate approximations, the results of the WDFSM method are slightly better than those of the SFSM approach. However, the SFSM method is computationally more efficient than the WDFSM method. The FSM (*Function Specification Method*) in both approaches is conceptually simple and can be readily extended to solve other inverse problems.

Berntsson [30] proposed an IHCP to determine the surface temperature of a shielded thermocouple. He solved the inverse problem using the Tikhonov method and used Finite Difference Method to solve the numerical thermal simulation.

The Function Specification Method was used by Samadi *et al.* [31] during the operation of a cutting tool to estimate the transient heat flux considering both constant and temperature-dependent thermal conductivity. Their numerical modeling employed ANSYS software, and the results showed that smoother results were obtained as the number of future data (r) increased. They concluded that the comparison between linear and nonlinear estimates affirmed the effectiveness of the method in handling nonlinear heat conduction problems.

Brito *et al.* [32] analyzed the thermal aspects in the operation of a cutting tool in machining processes. Due to the difficulty of obtaining process data with the tool in motion, they used the nonlinear Function Specification Method to determine the temperature field and the heat flux in the tool region.

Nanfuka *et al.* [26] addressed solution errors in the Cauchy problem for the heat equation, noting that the model amplifies measurement errors. They introduced a regularization method using a Cubic Smoothing Spline to approximate the time derivative, avoiding the periodicity assumption required by the Fourier method, which causes significant numerical errors. They demonstrated that the smoothing spline method effectively serves as a regularization technique for solving the Cauchy problem

Ngendahayo *et al.* [33] proposed an algorithm to solve an IHCP using multiple measurements taken inside the material. They formulated the problem as an operator equation and achieved stability through the Tikhonov Regularization method. By utilizing temperature measurements from different regions within the material, their approach estimates surface temperature with lower errors compared to methods that rely on data from a single point.

2.5 Summary of the Literature Review and Research Proposal

The literature review allowed the contextualization of the main technical elements that support this research. It was observed that, despite the widespread use of thermocouples as temperature sensors in thermal studies, proper attachment to metallic surfaces remains a significant challenge, especially in processes with rapid thermal transitions.

The technique of capacitor discharge welding emerges as a promising solution for this attachment, with the potential to ensure greater repeatability and lower thermal contact resistance. However, the literature lacks detailed studies evaluating the local thermal behavior during attachment by this method, as well as its influence on the quality of temperature measurement.

Thermal modeling, both analytical and numerical, has been widely explored to understand heat transfer processes, including those involving phase change. However, in situations where experimental data are limited or difficult to obtain, such as in accurate temperature measurement during welding, inverse problems become valuable tools for estimating variables such as heat rate.

In this context, this work proposes the development and the experimental and numerical analysis of a capacitor discharge welding process for thermocouple attachment, aiming to evaluate the influence of thermal measurement on heat rate estimation and, consequently, on the determination of the thermal efficiency of the process. To focus specifically on heat transfer phenomena, the complexities associated with fluid flow and electromagnetic effects were disregarded, and a simplified thermal model was adopted, justified by the very short duration of the process and the assumption that the influence of fluid formation is limited. This approach not only integrates the theoretical foundations discussed in the literature but also sets the stage for more accurate thermal characterization methods in high-intensity, short-duration processes. Furthermore, the proposed model and experimental setup provide a basis for future studies, including the evaluation of alternative inverse problem techniques and the refinement of thermal correction methods related to heat losses in the thermocouple bead and wires.

3 Numerical Methodology

In this chapter, the heat transfer model developed to address the heat transfer problem associated with the melting of wires is presented. The chapter begins by detailing the heat transfer equation used for the calculations, followed by a discussion of the thermal properties and parameters necessary for accurate modeling. The Joule effect equation is introduced next, explaining how the Joule effect is calculated based on the current flowing through the wires and highlighting its significance in the overall heat transfer process. Subsequently, the chapter shows the computational model implemented using COMSOL Multiphysics® software. This subsection provides an explanation of the domain and mesh setup, as well as the convergence test conducted to ensure the reliability and accuracy of the simulation results. Finally, the inverse heat transfer solution, an important component of this study, is discussed, which is employed to estimate the heat rate. This approach allows for refining the model and improving the accuracy of the estimation based on experimental data.

3.1 Defining steps

In this study, CDW is analyzed during the joining of K-type thermocouple wires, using a heat transfer approach. A self-developed machine is used to carry out the CDW process, providing flexibility and control over the parameters used in the experiments. Due to the rapid and complex nature of the process, the analysis is divided into steps. Firstly, the melting process, using the CDW process, of a single chromel wire is analyzed. Subsequently, the bead formation between the thermocouple wires is analyzed.

3.1.1 Melting one wire analysis using static wire model

In the initial approach, the discharge is released to initiate the melting of the chromel wire, producing a fused zone. Subsequently, the bead on the wire tip is formed through solidification. This process is illustrated in Figure 3.1, where the first quarter shows the wire positioned close to the electrode before contact, the second quarter shows the wire during the discharge, the third quarter shows the solidification after discharge, and the last quarter shows the bead at the end of solidification.

For the initial analysis, a simple static heat transfer model is used, excluding fluid flow considerations. This simplified model provides an initial understanding of the physics and phenomena involved in the process. Additionally, this approach aims to assess the influence of the measurement bead on the recorded temperature data. The temperature

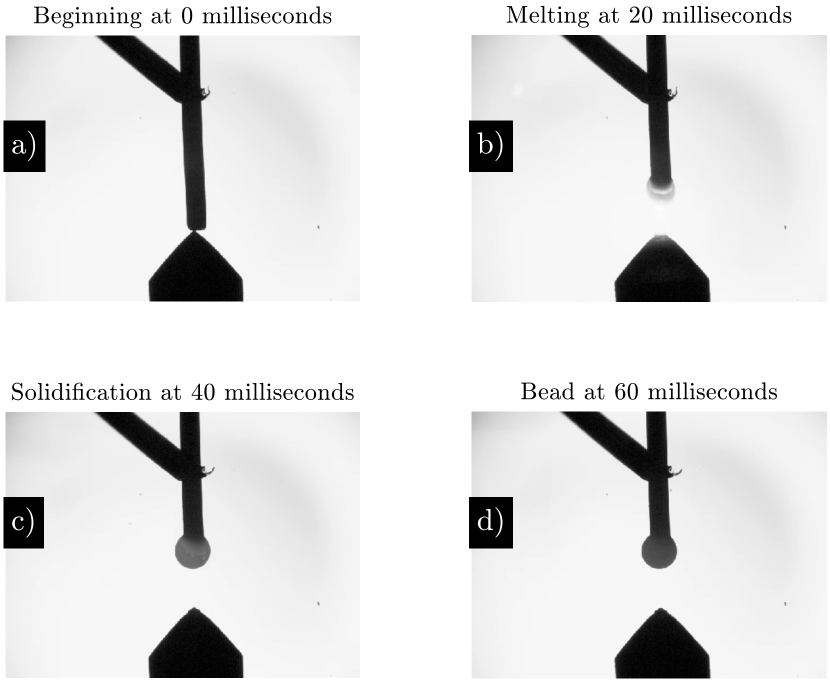

Figure 3.1 – Discharge released melting one chromel wire.

readings from the bead will be compared with simulated data to validate the simulation. Once the simulation reflects the experimental data, it can be used to determine the actual surface temperature of the wire, rather than the bead temperature. Following this validation, the heat flux consumed by the bead will be calculated by estimating the efficiency of the process.

3.1.2 Welding two wires analysis using static bead model

In the second approach, the bead formation between the thermocouple wires is analyzed. Despite the process being similar to the single wire analysis, this becomes more complex due to the mixture of two materials and the higher energy involved. This introduces additional physical effects, instability, and more energy dissipation. As presented in Figure 3.2, the process begins with the two wires making contact with the electrode when the discharge starts. Following the discharge, the wires melt and fuse, and then solidify to produce the bead between the tips of the wires. In this figure, it is also possible to observe the arc during the discharge and notice the asymmetry of the bead due to the differences in properties between the materials, effects that are analyzed in this study.

Given the rapid dynamics of bead formation, occurring in approximately 20 ms, a simplified model was adopted, focusing exclusively on the heat transfer aspect. The complexities related to fluid flow and electromagnetic effects were disregarded. To facilitate

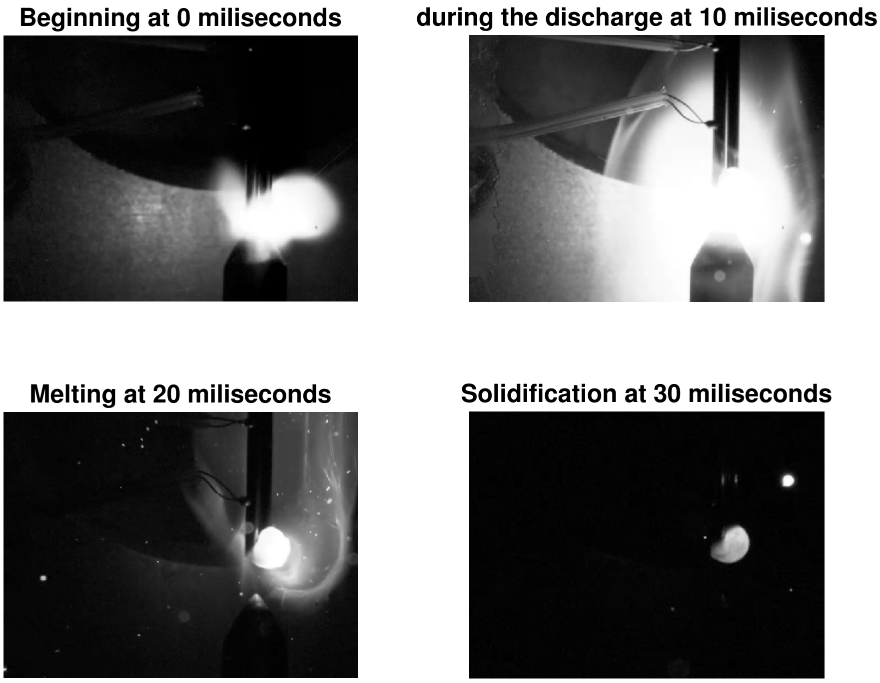

Figure 3.2 – Discharge released fusing two wire.

meshing and take advantage of geometric symmetry, the weld bead was represented as a static sphere, allowing for an efficient and focused thermal analysis.

3.2 Heat transfer equation

Two geometry were considered in this work. The first approach (A1), two wires, chromel and alumel, and the bead composed of both materials, were considered as shown in Figure 3.3a. In the second approach (A2), the thermocouple measuring bead (Ω_7) was also considered in geometry, as shown in Figure 3.3b.

The thermal model is composed by several subdomains. For the model A1: an alumel wire (Ω_1), a chromel wire (Ω_2) and a bead composed of a mixture of chromel and alumel (Ω_3), as shown in Figure 3.3a, the thermophysical properties in this subdomain are obtained by averaging the properties of the constituent metals. For the model A2: an alumel wire (Ω_4), a chromel wire (Ω_5) and a bead composed of a mixture of chromel and alumel (Ω_6), and also the bead of the measuring thermocouple (Ω_7), as shown in Figure 3.3b. Each subdomain has distinct thermal properties, in addition to distinct convective properties and boundary conditions. A convection boundary condition is applied on all surfaces Γ_1 to Γ_7. Since Γ is the boundary and Ω is the domain, the problem can be modeled by the system given by Eq. (3.1):

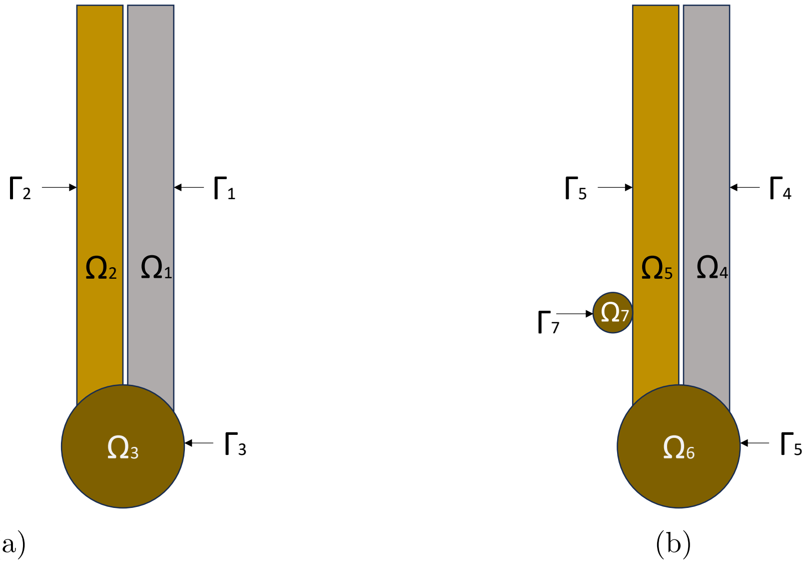

Figure 3.3 – a) Schematic of thermocouples geometry analyzed in the thermal model (A1). b) Schematic of thermocouples geometry analyzed in the thermal model (A2).

$$
\begin{cases}
\rho_m(T)c_{p_m}\frac{\partial T}{\partial t} = \nabla \cdot (k_m \nabla T)\,, & \text{in } \Omega_m, m = 1,2,7 \\
\rho_m(T)\frac{\partial H_m}{\partial t} = \nabla \cdot (k_m \nabla T) + Q_w(t), & \text{in } \Omega_m, m = 3,6 \\
\rho_m(T)c_{p_m}\frac{\partial T}{\partial t} = \nabla \cdot (k_m \nabla T) + Q_J(t), & \text{in } \Omega_m, m = 4,5 \\
-k_m \nabla T \cdot n = h\,(T - T_\infty) + \sigma\varepsilon(T^4 - T_\infty^4), & \text{in } \Gamma_n, n = 1,..,7 \\
T(x,y,z,0) = T_0, & \text{in } \Omega_m, m = 1,..,7
\end{cases}
\tag{3.1}
$$

The initial temperature of the domain, T_0, and the temperature of the surroundings, T_∞, are both 25 °C. The surface of the wires and the bead are subject to boundary conditions of convection and radiation, where n is the normal direction to the surface, h represents the convection heat transfer coefficient, σ is the Stefan-Boltzmann constant, ε represents emissivity and T_∞ is the room temperature. In this case, convection caused by factors such as arc welding, gas effects, rapid heating time, and the thinness of the wires was not considered. So, the convection coefficient is assumed to be h = 20 $\mathrm{W/(m^2 \cdot K)}$. Q_w represents heat rate over the volume generated by the arc welding and acts uniformly throughout the bead, Q_J represents heat rate over the volume generated by the Joule Effect on the wires, k represents the thermal conductivity, c_p represents specific heat, T is temperature, ρ is the density and t represents time.

The enthalpy, $H(T)$ function can be defined as:

$$H = \int c_p \, dT + \theta L \tag{3.2}$$

where L is latent heat and θ is liquid mass fraction in the phase change expressed by the Heaviside function (with a smooth transition equation) presented in Eq. (3.3), which is defined as a function of the melting temperature T_{m}. The function $\theta(T)$ is used to define the region of the phase transition. When $\theta(T) = 0$, the domain is in a solid state, and when $\theta(T) = 1$, the domain is fully liquid.

$$\theta(T) = \begin{cases} 0, & T > T_S \\ 1, & T < T_L \\ 0.5 + 0.9375\left(2 \times \frac{T-T_m}{\Delta T}\right) - 0.625\left(2 \times \frac{T-T_m}{\Delta T}\right)^3 & \\ +0.1875\left(2 \times \frac{T-T_m}{\Delta T}\right)^5 & T_S < T < T_L \end{cases} \tag{3.3}$$

Equation (3.3) smooths the phase transition, offering the liquid and solid fraction for each temperature within the transition, as illustrated in Figure 3.4, based on the melting temperature of the bead material.

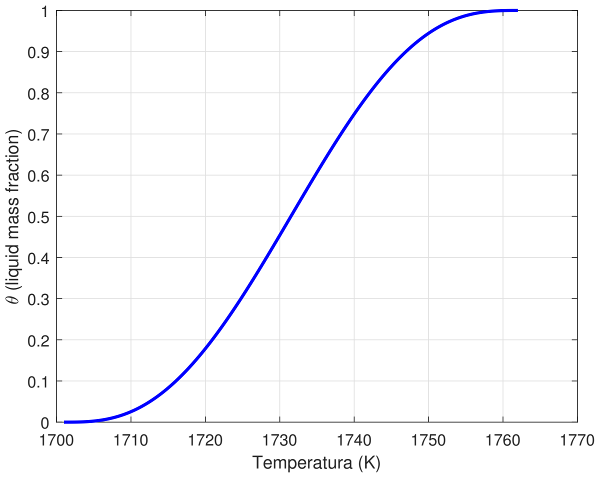

Figure 3.4 – Liquid mass fraction (θ) as a function of temperature (T).

In the phase transition zone, the densities and entalphy are computed as the weighted average of the solid/liquid fraction represented by $\theta(T)$ in Eq. (3.3), and shown as:

$$\rho = (1 - \theta)\rho_S + \theta\rho_L \tag{3.4}$$

where the property is evaluated with temperatures T_S and T_L, the index s represents the property in solid phase and L the properties in liquid phase.

3.2.1 Thermal Properties

The densities were calculated as weighted averages of the alloy elements. For Chromel, composed of 90% Ni and 10% Cr, the densities were determined to be 8736 kg/m^3 in the solid state and 7659 kg/m^3 in the liquid state. For Alumel, consisting of 95% Ni, 2% Al, 2% Mn, and 1% Si, the densities were 8689 kg/m^3 in the solid state and 7611 kg/m^3 in the liquid state. The phase transition temperatures for Chromel were determined using the Nickel-Chromium phase diagram, with the solidus temperature (T_{solidus}) defined as 1458°C (1731 K) and the liquidus temperature (T_{liquidus}) as 1477°C (1750 K). For Alumel, the phase transition is more complex to define due to its multi-element composition. However, the melting process was considered to start at 1399°C (1672 K), with a transition range of 20°C, leading to complete melting at 1419°C (1692 K).

The thermophysical properties of chromel and alumel, specifically the conductivity k(T) and specific heat c_{p}(T), were obtained from Buttsworth [36] and are defined by the Equations (3.5-3.8).

$$c_{p(chromel)}(T) = 0.1786 \times T + 394.3 \; [J/(kg.K)] \tag{3.5}$$

$$k_{chromel}(T) = 0.01912 \times T + 12.11 \; [W/(m.K)] \tag{3.6}$$

$$c_{p(alumel)}(T) = 0.0712 \times T + 500.8 \; [J/(kg.K)] \tag{3.7}$$

$$k_{alumel}(T) = 0.02981 \times T + 18.42 \; [W/(m.K)] \tag{3.8}$$

In these equations, the temperature T is expressed in Kelvin. To extrapolate these properties to higher temperature levels, some assumptions were made. The linear equation provided by Buttsworth [36], originally valid for the range of 300 K and 1000 K, was extended up to the solidus temperature (T_{solidus}). Beyond this temperature, the properties were assumed to remain constant. To ensure smooth transitions and improve numerical convergence, a logarithmic smoothing function was applied between the linear region and the constant values beyond T_{liquidus}. The results of these assumptions and transitions are shown in Figure 3.5, which shows the trends in specific heat and thermal conductivity over a range of temperatures.

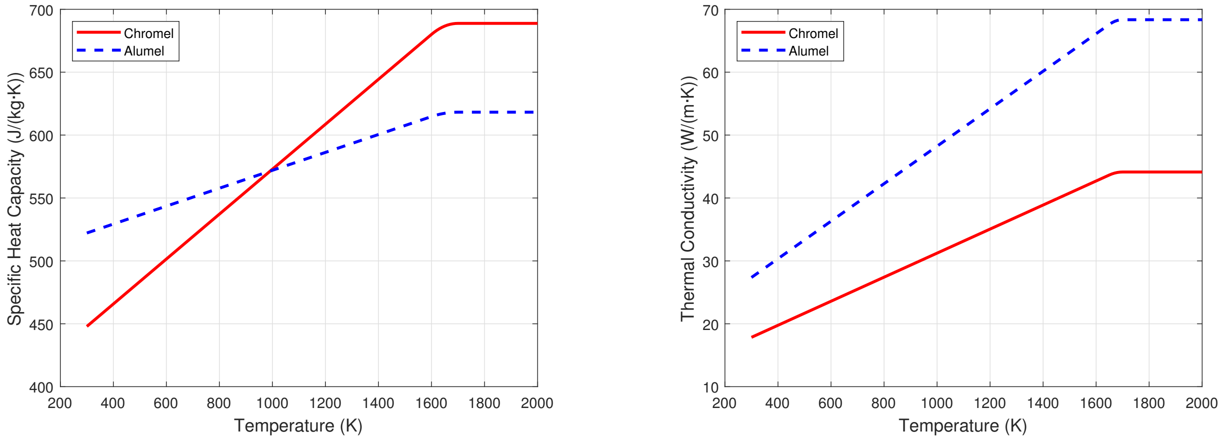

(a) (b)

Figure 3.5 – Thermophysical properties as function of temperature: a) Specific heat, $c_p(T)$. b) Thermal conductivity, $k(T)$.

In addition, the equations for the emissivity of chromel and alumel were obtained by performing linear regression on discrete values extracted from data presented by Sasaki *et al.* [37], as follows:

$$\varepsilon_{chromel}(T) = 1.2 \times 10^{-4} \times T + 0.0528 \tag{3.9}$$

$$\varepsilon_{alumel}(T) = 1.55 \times 10^{-4} \times T + 0.0212 \tag{3.10}$$

An approximate assumption was made that the sphere representing the bead is formed by an equal blend of 50% alumel and 50% chromel. This fact is confirmed in section 4.8. Thus, the thermophysical properties in this subdomain are obtained by averaging the properties of the constituent metals of the thermocouple.

3.2.2 Joule effect equation

Due to the thin dimensions of the wire, the Joule effect becomes evident during welding and significantly influences the wire temperature. Therefore, the Joule effect must be considered in the equation. The effect is modeled as a volumetric heat source that acts on the entire volume of the wire. The heat source produced by the Joule effect is defined as follows:

$$Q(t) = \frac{P(t)}{V} = \frac{R \times i(t)^2}{V} \tag{3.11}$$

where $Q(t)$ is the power density of heat source in W/m^3, V is the volume of the wire in m^3, i is the electrical current during the time A, R is the electrical resistance of the wire, that is calculated as:

$$R = \frac{\rho \times L}{A} \tag{3.12}$$

where ρ is the electrical resistivity of the material, L is the length of the wire and A is the cross-sectional area of the wire.

Replacing the Eq. (3.12) in the (3.11), it is obtained the power density of heat source in function of ρ, i and A:

$$Q(t) = \frac{\rho \times \frac{L}{A} \times i(t)^2}{A \times L} = \rho \times \frac{i(t)^2}{A^2} \tag{3.13}$$

The voltage distribution in the process is depicted in Figure 3.6 and distributed as follows: V_{total} represents the total voltage measured across the capacitor bank, V_{resistor} is the voltage measured across the high-power resistor, V_{welding} is the unknown voltage of the system, and V_{wire} represents the voltage across the wire calculated using the resistance of the Eq. (3.12) and the circuit current as:

$$V_{\text{wire}} = R \times i \tag{3.14}$$

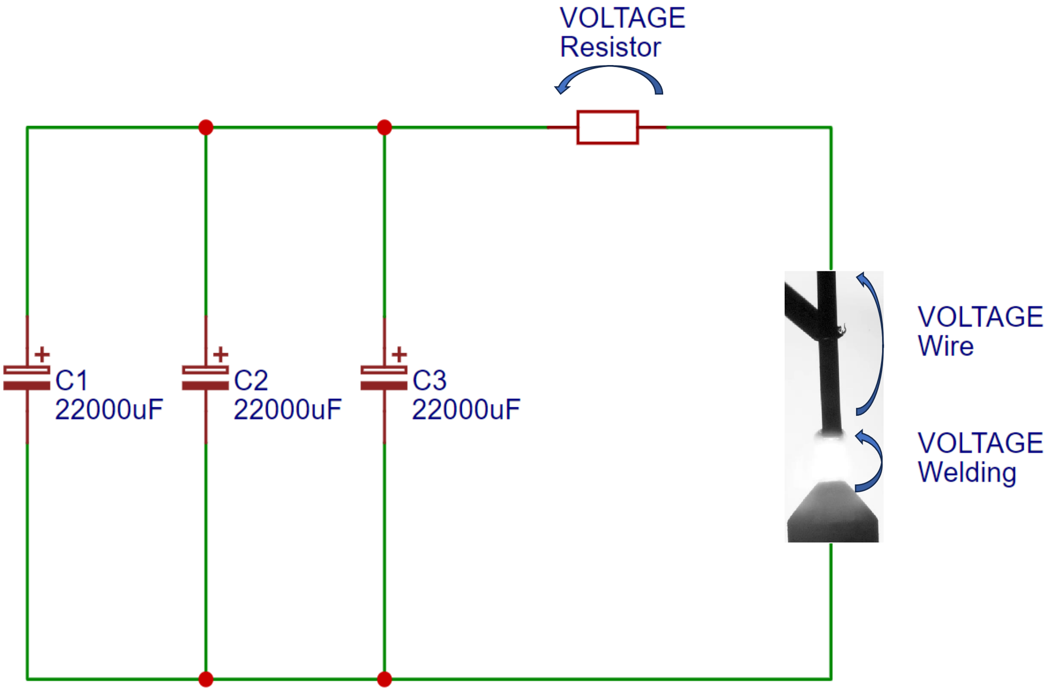

Figure 3.6 – Voltage distribution in circuit components.

This setup allows the calculation of the voltage across the welding resistance, as shown in Eq. (3.15), and the determination of the power used in the welding process, as expressed in Eq. (3.16).

$$V_{\text{total}} = V_{\text{wire}} + V_{\text{welding}} + V_{\text{resistor}} \tag{3.15}$$

$$P_{\text{welding}} = V_{\text{welding}} \times i \tag{3.16}$$

3.3 Simulating and calculating (COMSOL)

The calculation of the three-dimensional temperature distribution was performed using the FEM through the commercial program COMSOL Multiphysics.

3.3.1 Mesh

To ensure the accuracy and efficiency of the model, we conducted a mesh convergence test by refining the mesh at four distinct levels: coarse, normal, fine, and extremely fine. The objective was to evaluate how mesh refinement influences the obtained results and simulation time, allowing for the selection of the most suitable mesh for the model.

The extremely fine mesh, denoted as M_1, with 377,000 elements, took 59 seconds to calculate the temperatures over a 4 seconds simulation. The fine mesh, denoted as M_2, with 124,000 elements, completed the simulation in 24 seconds. The normal mesh, denoted as M_3, with 2,238 elements, took 7 seconds, while the coarse mesh, denoted as M_4, with 1,166 elements, completed the calculation in 6 seconds.

The results indicated that the M_2 mesh produced temperature results very similar to those of the M_1 mesh, with minimal differences, as illustrated in Figure 3.7. This demonstrates that the M_2 mesh is highly efficient, achieving nearly the same accuracy as the M_1 mesh but with a significantly shorter simulation time, only half the time.

In contrast, the M_3 and M_4 meshes showed considerable discrepancies compared to the M_1 mesh, with more pronounced differences in temperature results. This suggests that, although faster, these meshes may compromise the accuracy of the model, making them less suitable for simulations requiring high precision.

Based on these results, the M_2 mesh was chosen as the optimal option for modeling. It offers an excellent balance between accuracy and computational efficiency, providing a fast simulation without significantly compromising the accuracy of the results.

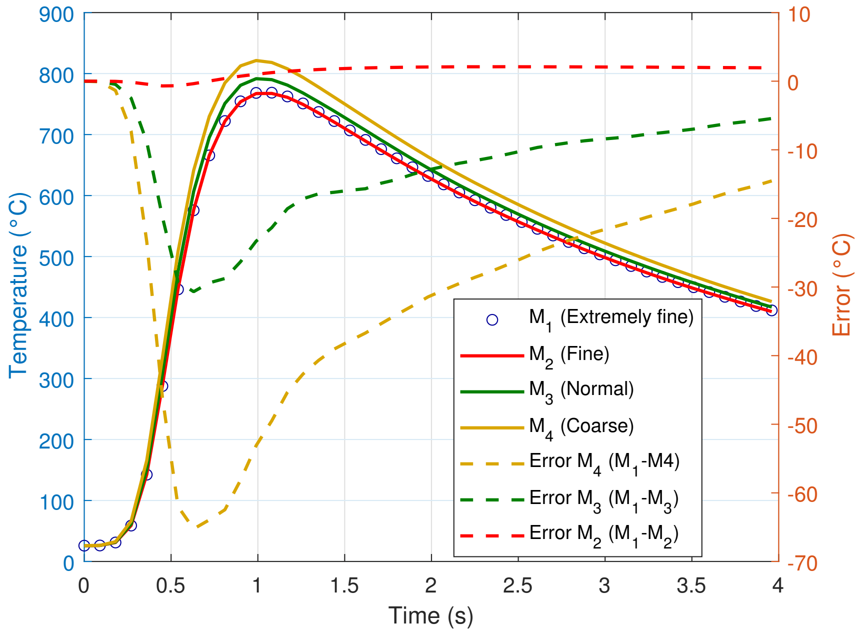

Figure 3.7 – Comparison of temperature results and errors across different mesh refinements.

3.4 Inverse heat transfer problem

Measuring the temperature at the tip of a thermocouple wire during bead formation is a complex task due to specific attributes that create obstacles for the measurement procedure, notably the phase transition and the high temperature. Estimating the heat input from the welding process involves addressing inverse heat conduction problems. In this method, temperature data gathered from accessible points along the wire are utilized to determine the heat rate applied to bead formation. Once the supplied heat rate is estimated, we can then assess the thermal efficiency of the process. This enables us to analyze the experimental and thermal model errors, leading to more accurate results and conclusions.

This study employs the Iterative Function Specification Method [38] to address the inverse heat transfer problem. Grounded in the Gauss Minimization Method, this approach is adept at solving nonlinear problems.

In this manner, the objective function is established as the squared difference between experimental temperatures, $\mathbf{Y}$, and numerical temperatures, $\mathbf{T}$, calculated using COMSOL Multiphysics. The numerical temperatures are described as a function of the unknown heat rate, $\mathbf{q}$. Since experimental temperature data is measured in two different positions along the wire, the procedure aims to compare and minimize the difference for both thermocouples. Thus, the objective function S_M is expressed as:

$$S_M = \sum_{j=1}^{J} \sum_{i=M}^{M+r-1} (Y_{j,i} - T_{j,i}(q_M))^2 \tag{3.17}$$

The parameter J denotes the number of temperature sensors while r represents the number of future data. It is worth noting that the parameter r functions to regularize the outcomes of the estimation by using temperature data from r time steps in advance of the current moment, t_M, for estimating q_M.

Given that the vector $\mathbf{T}$ is a function of the heat rate vector $\mathbf{q}$, the temperature at a point in the domain can be approximated through the Taylor series expansion:

$$\mathbf{T}_i|_{q+\Delta q} = \mathbf{T}_i|_q + \frac{\partial \mathbf{T}_i}{\partial q}|_q \Delta q \tag{3.18}$$

In Equation (3.19), the derivative term represents the rate at which temperature changes in response to a perturbation in the heat rate. This particular derivative is known as thermal sensitivity and its value is a function of the thermal parameters and the location within the domain. In this context, the thermal sensitivity, denoted as $\mathbf{X}$, is defined as follows:

$$\mathbf{X} = \frac{\partial T}{\partial q} = \begin{bmatrix} \frac{\partial T_1}{\partial q} \\ \frac{\partial T_2}{\partial q} \\ \vdots \\ \frac{\partial T_r}{\partial q} \end{bmatrix} \tag{3.19}$$

Replacing Eqs. (3.18) and (3.19) into Eq. (3.17), the objective function becomes:

$$S_M = \sum_{(j=1)}^{J} (\mathbf{Y}_i - \mathbf{T}_i|_q - \mathbf{X}\Delta q)^T (\mathbf{Y}_i - \mathbf{T}_i|_q - \mathbf{X}\Delta q) \tag{3.20}$$

In order to identify the heat rate magnitude that minimizes Eq. (3.20), the objective function is derivate in relation to the increment Δq and the derivative is forced to zero. Since the number of temperature sensors is known as two, the increment can be written as shown in Eq. (3.21):

$$\Delta q = [\mathbf{X}_1^T \mathbf{X}_1 + \mathbf{X}_2^T \mathbf{X}_2]^{-1} [\mathbf{X}_1^T (\mathbf{Y}_1 - \mathbf{T}_1) + \mathbf{X}_2^T (\mathbf{Y}_2 - \mathbf{T}_2)] \tag{3.21}$$

Thus, for each time step M, the increment Δq must be computed until the Eq. (3.22) reaches the convergence:

$$q_M^{(i+1)} = q_M^{(i)} + \Delta q_M^{(i)} \tag{3.22}$$

As outlined in Woodbury [39], achieving convergence can be challenging at times. One approach to ensure this convergence is to demand that each increment of the vector $\mathbf{q}$ has a relatively small magnitude compared to its own value. As described in Eq (3.23):

$$\frac{\Delta q_M}{q_M} < \delta \tag{3.23}$$

Usually, the parameter δ is configured with a value less than or equal to 0.001. Setting an exceedingly small tolerance results in considerably prolonged computation times. This extension in time might not be justified by the gained precision and could potentially result in non-convergence during certain time steps.

3.4.1 Validation of the proposed method

To validate the interaction between the physical model and the inverse problem solution algorithm, a numerical simulation was carried out in which temperatures were calculated from a known heat rate, as shown in Figure 3.8. The resulting temperature profile was then considered as "experimental temperature"and used as input to estimate the heat rate, applying the Iterative Function Specification Method described in this chapter.

The purpose of this procedure is to verify whether the estimated heat rate converges to the actual value used in the direct simulation, thus validating the effectiveness of the model and the consistency of the inverse problem solution algorithm. The comparison between the original and estimated heat rates allows the evaluation of the accuracy and stability of the proposed method. This type of numerical validation is an essential step before applying the method to real experimental data, as it allows the identification of potential limitations of the model and the adjustment of parameters or regularization strategies, such as the number of future time steps considered (r), when necessary.

Figure 3.8 shows the heat rate estimation results for two values of r (number of future time steps): $r = 12$ and $r = 20$. It can be observed that both estimates adequately reproduce the general trend of the original curve. However, for $r = 12$, the estimation presents higher oscillations (noise), although it more accurately reaches the heat rate peak of 40 W. In contrast, for $r = 20$, the estimated curve is smoother and less noisy, but it underestimates the peak, not reaching the maximum heat rate value.

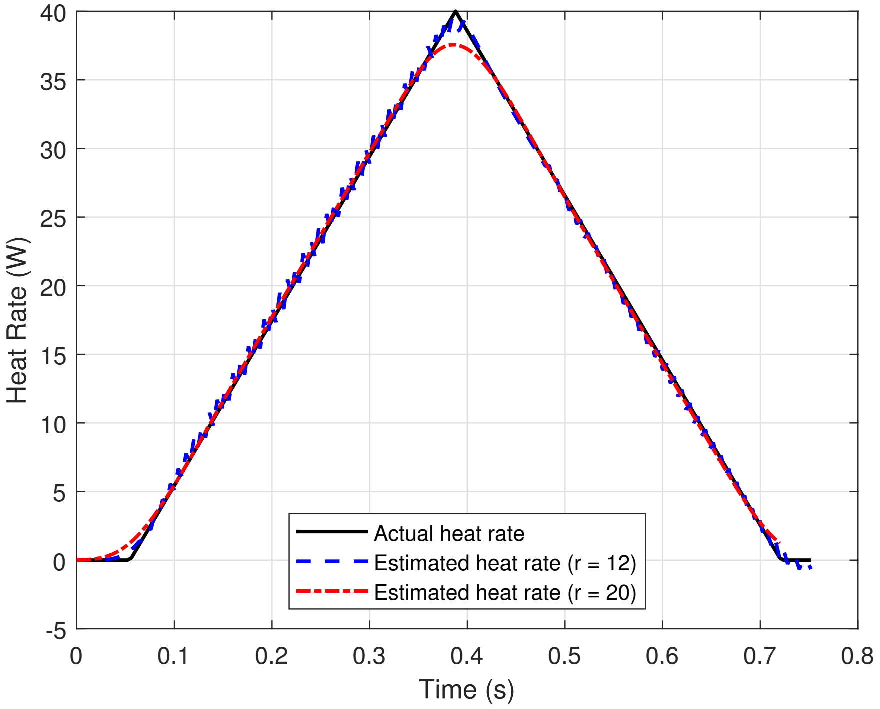

Figure 3.8 – Comparison of actual and estimated heat rates for $r = 12$ and $r = 20$.

Figure 3.9 presents the temperature profiles obtained from the actual and estimated heat rates. Despite the oscillations observed in the heat rate for $r = 12$, the estimated temperature shows good agreement with the actual curve, with differences smaller than 0.5°C throughout the entire time domain. This indicates that even with a lower value of r, the model is capable of adequately reconstructing the variable of interest. For $r = 20$, a maximum difference of approximately 1.5°C is observed between the actual and estimated temperatures. Although the absolute error is higher, the smoothing effect obtained with this value of r may be advantageous in cases involving noisy experimental data, reinforcing the importance of appropriately selecting the regularization parameter.

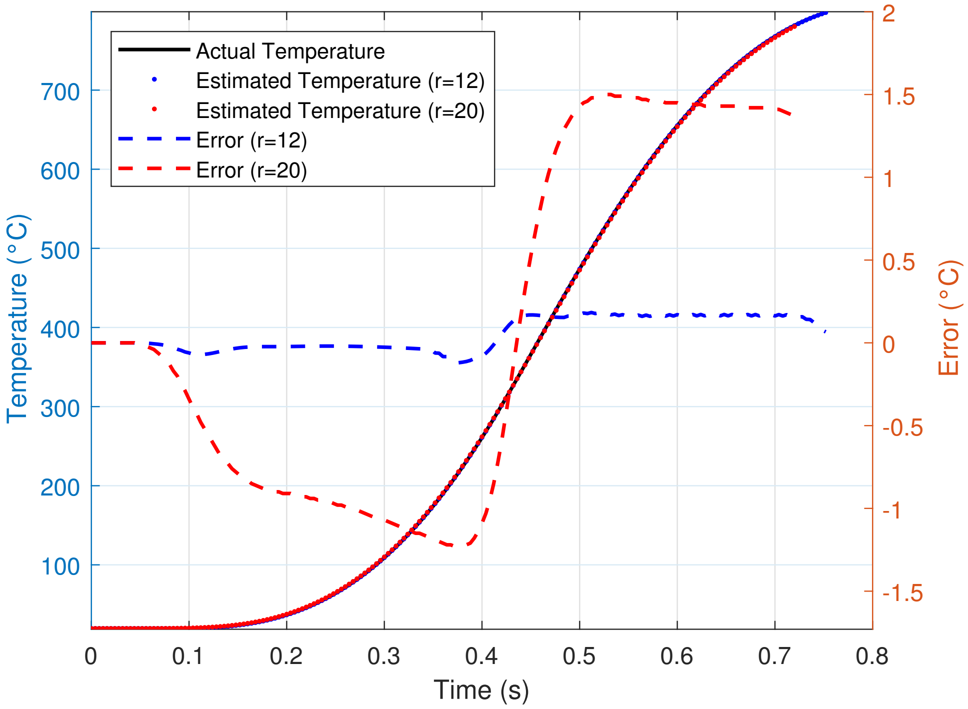

Figure 3.9 – Comparison of actual and estimated temperatures for $r = 12$ and $r = 20$.

4 Experimental Procedures

This section presents the experimental procedures adopted to investigate the CDW process applied to the joining of thermocouple wires. To this end, a custom-developed device specifically designed for this process is presented, which acted as the heat source to promote the union between the thermocouple wires. During the welding process, simultaneous acquisition of physical quantities was performed in order to characterize the thermal and electrical phenomena involved. The measurements included electrical quantities such as current and voltage, as well as the temporal evolution of the temperature in the specific region of the domain and the recording of images of the process using high-speed cameras.

In parallel with the welding process, but still within the experimental methodology, the electrical resistivity (temperature-dependent) of the chromel and alumel wires used was measured. This step was conducted independently from the welding process, aiming to obtain representative material parameters, which will later be used as input for the proposed numerical model. In addition, elemental composition analysis was carried out on both the wires and the welded bead, with the aim of identifying possible changes in the metallic alloy caused by the thermal process, as well as verifying the homogeneity and compatibility between the joined materials.

These combined experimental procedures enable a comprehensive understanding of the CDW process, providing data for equipment performance analysis, thermal model characterization, and the use of temperature data for inverse problem estimations.

4.1 Capacitor Welding Device

To conduct the welding experiments and improve the attachment of measuring thermocouples, a customized capacitor discharge welding device was developed with precise control over the energy stored in the capacitor bank. Unlike previous designs, such as the device by Fermo *et al.* [40], which prioritized usability with a microcontroller and LCD (*Liquid Cristal Display*) display, the device in this study employs a manual energy adjustment through a potentiometer and direct voltage measurement on the capacitor bank using a digital voltmeter. This precise, manual energy selection enables flexibility in welding both fine thermocouples, such as 40 AWG (*American Wire Gauge*), and thicker ones, up to 20 AWG.

A block diagram illustrating the device structure is shown in Figure 4.1. In the first stage, power is drawn from a 110 V or 220 V AC mains supply and converted to 50 V DC. The second stage controls the voltage supplied to the capacitor bank via a voltage regulator adjusted by the potentiometer. Finally, the necessary energy for the welding process is stored in the capacitor bank, with the actual voltage monitored by the digital voltmeter.

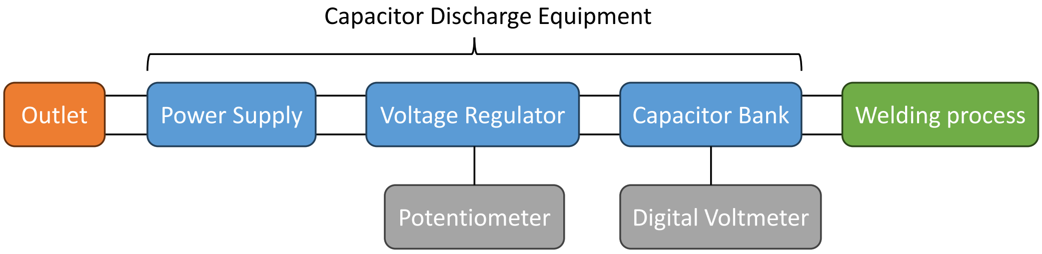

Figure 4.1 – Stages of the device presented in block diagram.

The electrical schematic of the device is divided into two parts. The first part, shown in Figure 4.2, illustrates the voltage regulator, which controls the voltage supplied by the 48 V switched-mode power supply ($J2$). In this design, the IRF3205 MOSFET transistor ($U1$ and $U2$) is the main component, dissipating voltage to achieve the desired output level. The IRF3205 is controlled by the potentiometer ($R5$).

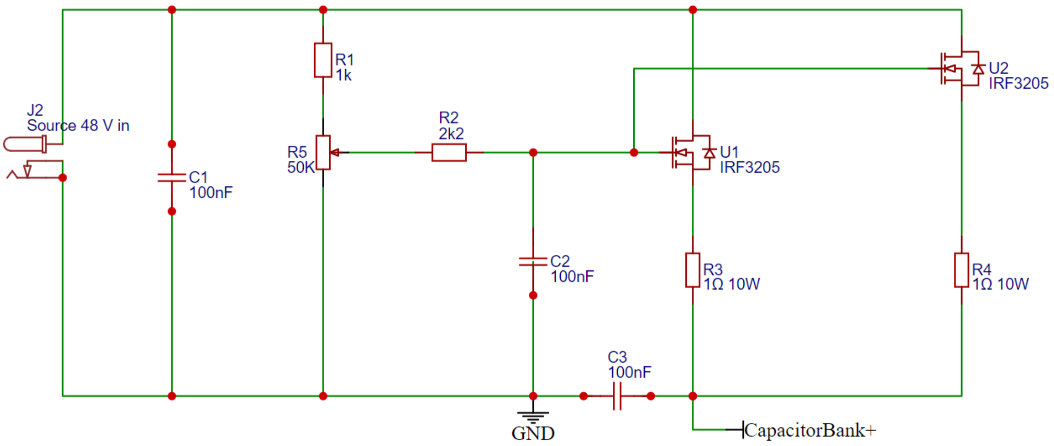

Figure 4.2 – Electrical design of voltage regulator.

The second part of the schematic, presented in Figure 4.3, shows the capacitor bank, composed of three 22000 μF capacitors. The regulated voltage source charges the capacitor bank, triggered by button $P1$. When the voltage reaches the desired level for welding, button $P3$ initiates the discharge for the welding process. If the capacitor bank holds a higher than required charge, button $P2$ discharges it safely through a power resistor, $R4$.

To simplify the assembly, a PCB *(printed circuit board)* was designed and manufactured, as shown in Figure 4.4, displaying both sides of the PCB. The electronic

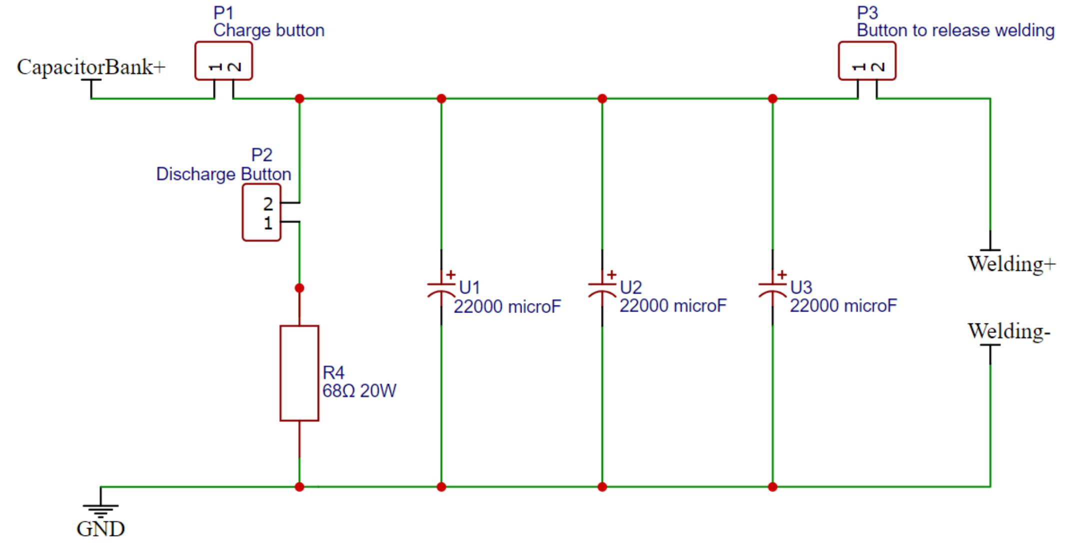

Figure 4.3 – Electrical design for capacitor bank.

components were soldered to the PCB using soldering iron and tin solder. After assembly, the board was connected to the power supply and the output terminals of the device. All components were enclosed within a protective casing, shown in Figure 4.5, which ensures safe operation and portability. The complete setup was tested with different thermocouple wire gauges to validate its capability to weld both thin and thick wires.

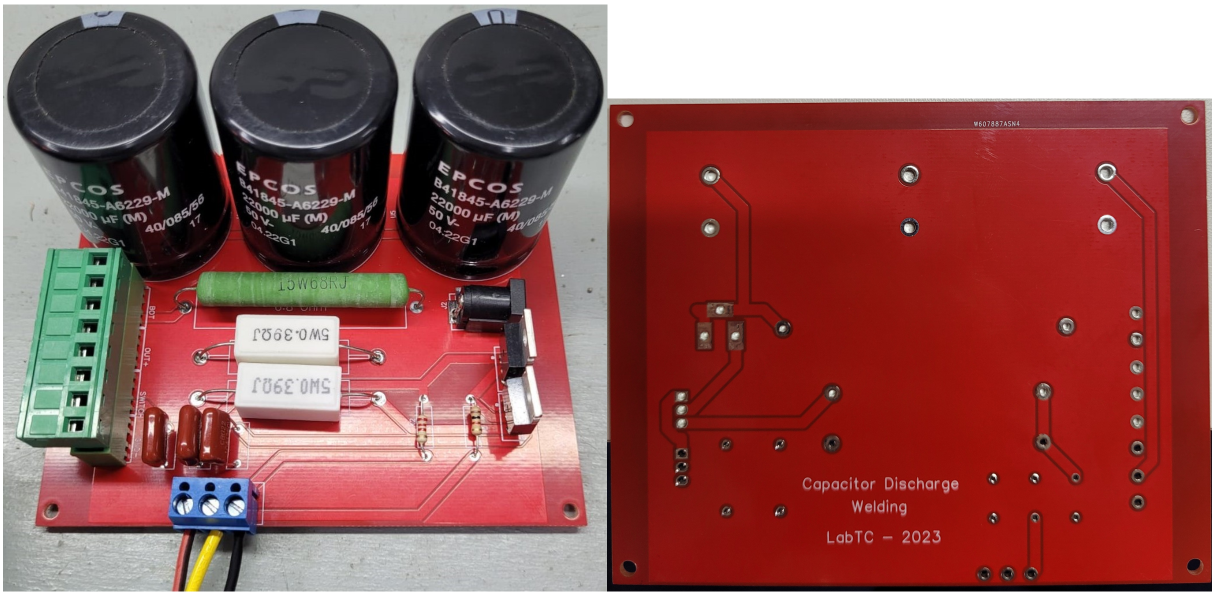

(a)

(b)

Figure 4.4 – Front and back views of the PCB developed to simplify the device assembly. a) Front side with components soldered. b) Back side of the printed circuit board.

The final device provides appropriate electrical insulation and mechanical protection, with a simple and user-friendly interface designed for safe operation. It offers a

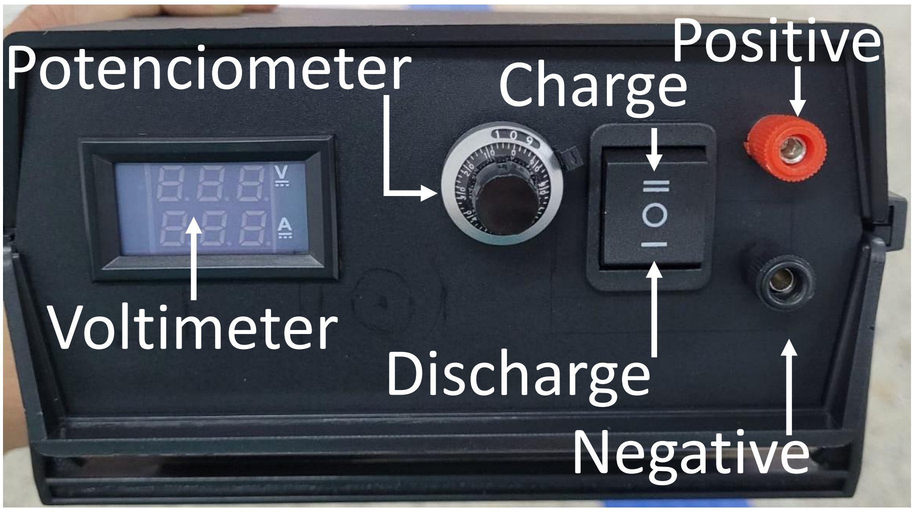

Figure 4.5 – Final assembled welding device.

reliable and customizable solution for joining thermocouple wires and also fixing them in metallic surfaces in laboratory environments.

4.2 Capacitor Discharge Welding Process

The CDW process studied in this work is applied to the joining of K-type thermocouple wires. This process is characterized by a high-intensity, short-duration energy pulse. In the tests performed, the discharge time was approximately 20 ms, with a peak current of around 160 A and an initial voltage of 40 V between the electrode and the wires. To carry out the process, the developed device was used. The positive terminal of the capacitor bank is connected to the thermocouple wires, while the negative terminal is connected to a tungsten electrode, as shown in Figure 4.6.

The manually controlled linear motion system allows precise positioning of the electrode in three directions. This positioning control ensures repeatability of the process, ensuring that the contact always occurs between the tips of the two wires. It also enables the application of a controlled contact force at an extremely low speed, which is important for the consistency and repeatability of the weld. Once aligned, the electrode and wires make contact, initiating an electric arc. This arc causes localized heating and melting of the wire tips, forming a weld bead due to surface tension. In addition to arc heating, the wires also undergo resistive heating due to the Joule effect. The rapid heating followed by cooling prevents excessive diffusion between the materials, which is essential for maintaining the thermoelectric properties of the thermocouples. The result of this process is shown in Figure 4.7.

In addition to the welding of two thermocouple wires, preliminary simplified tests were also carried out with the aim of studying the process behavior by melting only the

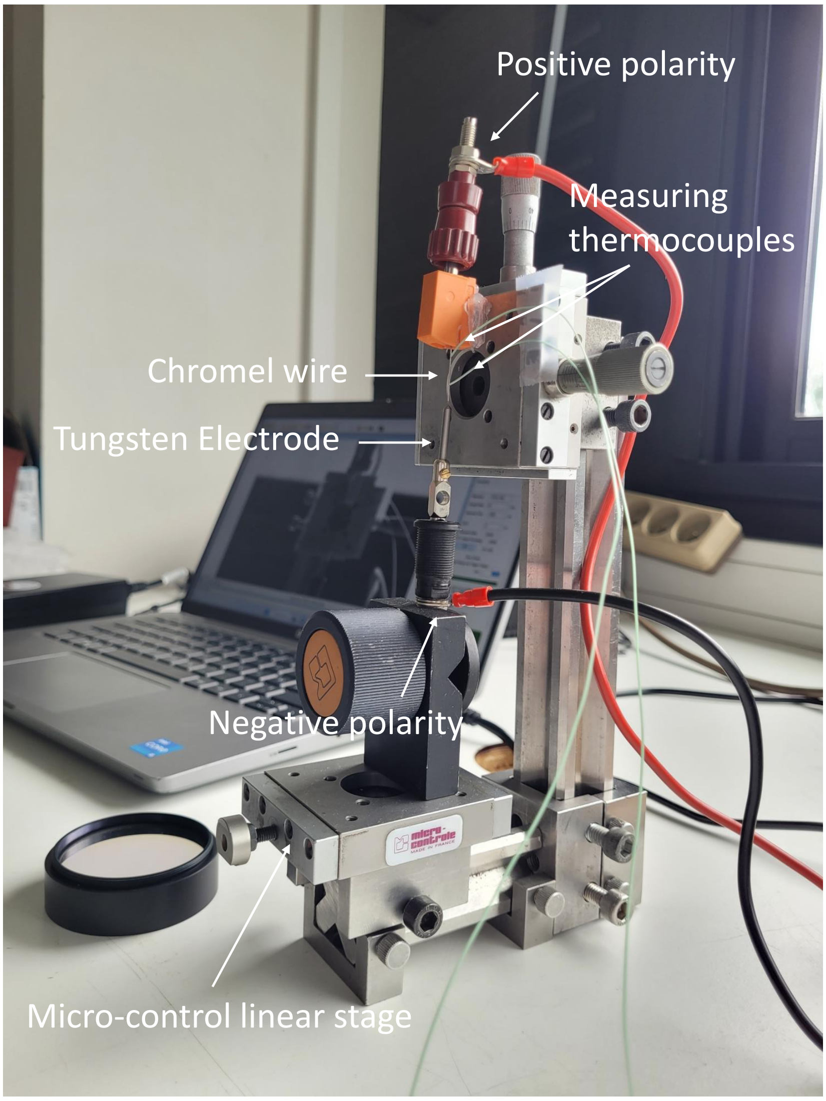

Figure 4.6 – Schematic of the capacitor discharge welding system used for joining thermocouple wires.

tip of a single Chromel wire. These tests made it possible to analyze the bead formation and thermal effects of the discharge in a single material in isolation.

Throughout all tests, both the thermocouple wire welding and the preliminary trials, the data described in the introduction to this chapter were collected: electrical quantities, temperature, and high-speed images. This information will later be used to validate the proposed thermal model, in inverse problems for heat rate estimation, and in analysis of the temperature measurement methods used, which may be further explored in future studies.

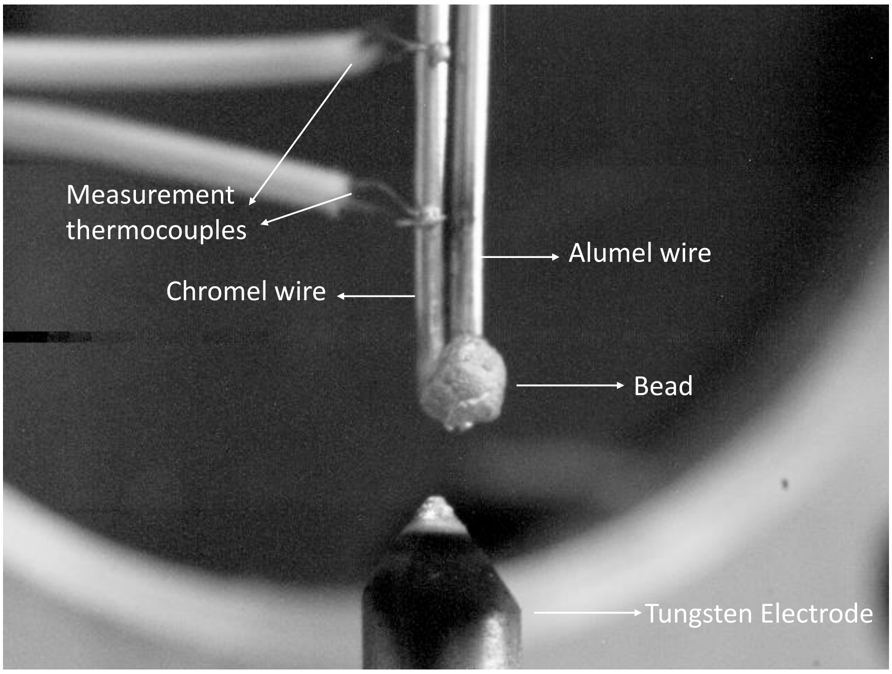

Figure 4.7 – Image of thermocouple wires after capacitor discharge welding, showing the formation of the weld bead.

4.3 Measuring electrical quantities during the process using the oscilloscope

To determine the electrical quantities of the welding process, including voltage, electrical current, and resistance, an electrical design was designed, as presented in Figure 4.8. The procedure involves the collection of voltage data across a high-power resistor (R_1), which is in series with the welding system. Once the resistance of this high-power resistor is known, it enables the calculation the current flowing during the welding process using the collected voltage data.

The oscilloscope is a fundamental tool in an engineering laboratory for measuring electrical quantities, including voltage and signals waves. Unlike other instruments, such as multi-meters, the oscilloscope is able to show electrical signals details, providing deep comprehension of their characteristics. It maintains sampling performance even when altering horizontal settings or utilizing multiple channels. The compact design of oscilloscope and user-friendly interface enhance its usability, making it an efficient tool for data analysis.

Upon triggering the oscilloscope and connecting the capture to the OpenChoice Tektronix software, the obtained values allow for the visualization of voltage data at intervals of 0.4 ms. This specific interval is achieved through measurements conducted by the oscilloscope at a rate of 100 ms per quadrant. Without executing this setup, the oscilloscope does not display data at this specific interval. The speed of data retrieval

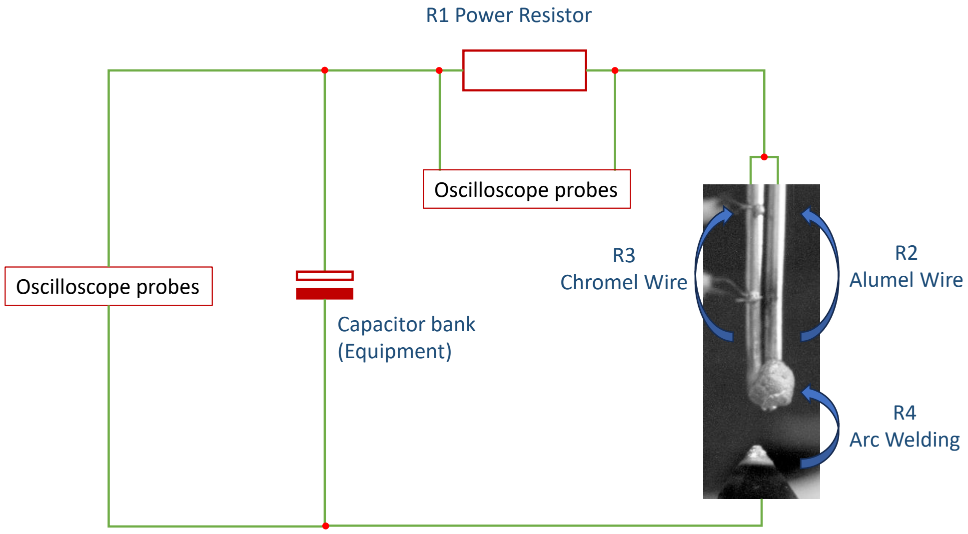

Figure 4.8 – Electrical design for oscilloscope.

from the software depends on the oscilloscope rate setting. Moreover, with a DC voltage range of ±45 V, the oscilloscope is well-suited for measuring the voltage on the capacitor bank.

In Figure 4.9, the image of the experimental bench used to collect electrical data using the oscilloscope is shown. Figure 4.8 illustrates the oscilloscope probes, denoted by the letter P, which are connected to the oscilloscope input, $CH1$ and $CH2$. Probes $P1$ and $P2$ are responsible for collecting voltage information from the capacitor bank, while $P3$ and $P4$ collect voltage data from the high-power resistor $R3$.

4.4 Measuring electrical quantities during the process using the data acquisition

The data acquisition is a tool for electrical collection, offering some advantages. One of them is its capacity to transmit data for storage on a computer. Another advantage is to simultaneously collect voltage data from various channels, including both electrical components and thermocouples that can be converted to temperature readings. This approach ensures the acquisition of data on a unified timescale.

As the data acquisition channel can measure voltages up to 10 V, a voltage divider was designed to collect the voltage evolution on the capacitor bank during the process. The resistors R_1 and R_2 work as this voltage divider, connected in parallel with the capacitor bank enables the collection of voltage data specifically on resistor R_2. This data facilitates the calculation of the voltage changes occurring on the capacitor bank throughout the

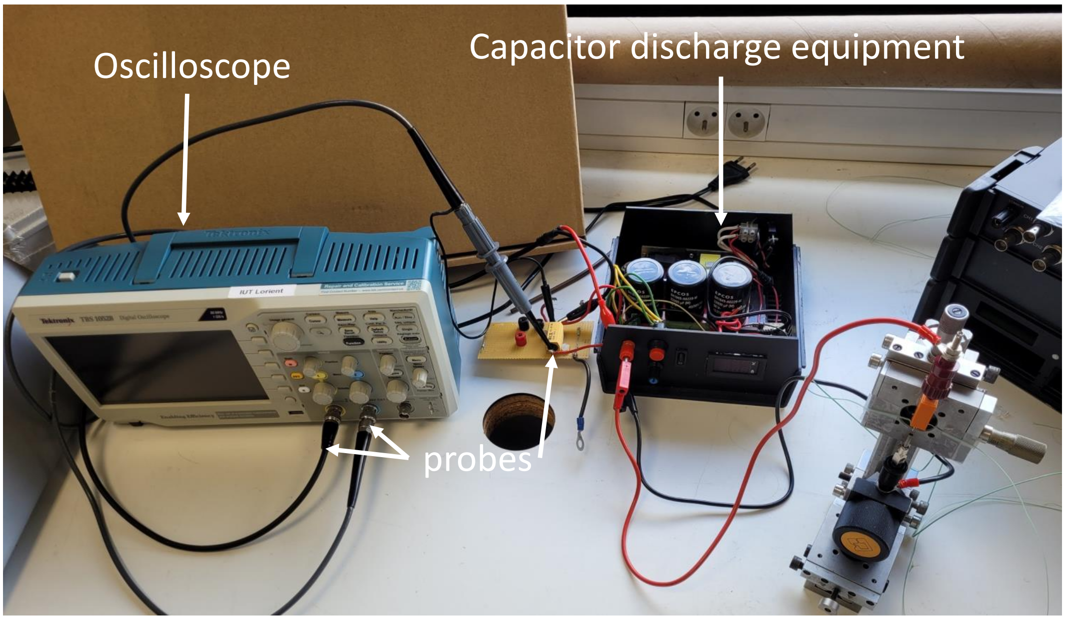

Figure 4.9 – Apparatus for measuring by oscilloscope.

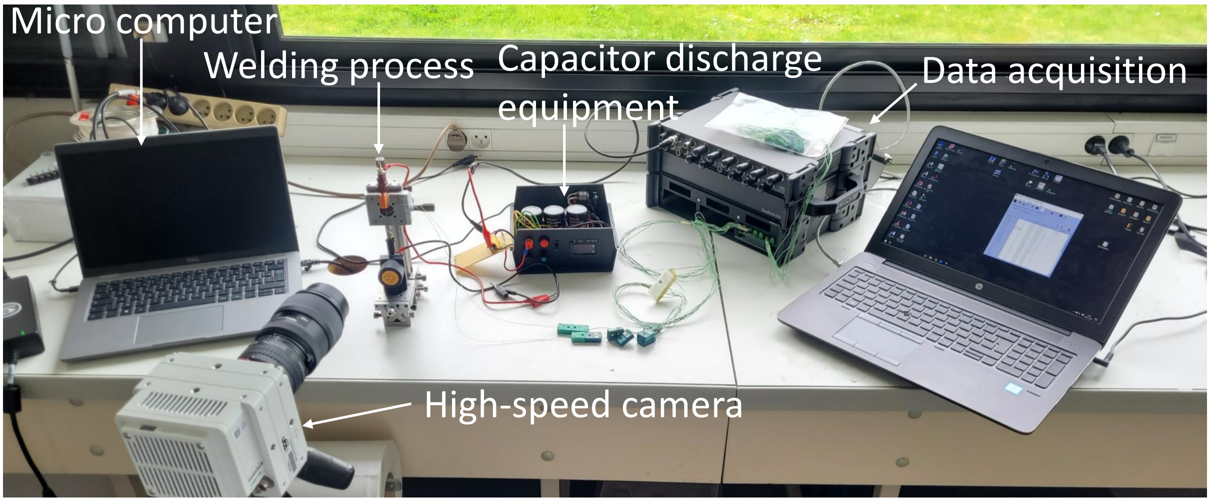

Figure 4.10 – Apparatus for measuring by data acquisition.

process.

A voltage divider is an arrangement of resistors in series, used to obtain a specific potential difference from a fixed voltage power supply. In Figure 4.11, a simple voltage divider is presented, consisting of two resistors, R_1 and R_2. The power supply provides an input voltage, V_{in}, and an output voltage, V_{out}, measured across the terminals of R_2. The output voltage is a fraction of the input voltage, that is $V = \alpha\epsilon$, where α is represented by $R_2/(R_1 + R_2)$ and varies from 0 to 1. In the series resistor circuit, the voltage in the circuit will divide proportionally based on the value of each resistor in relation to the total value of the series [41].

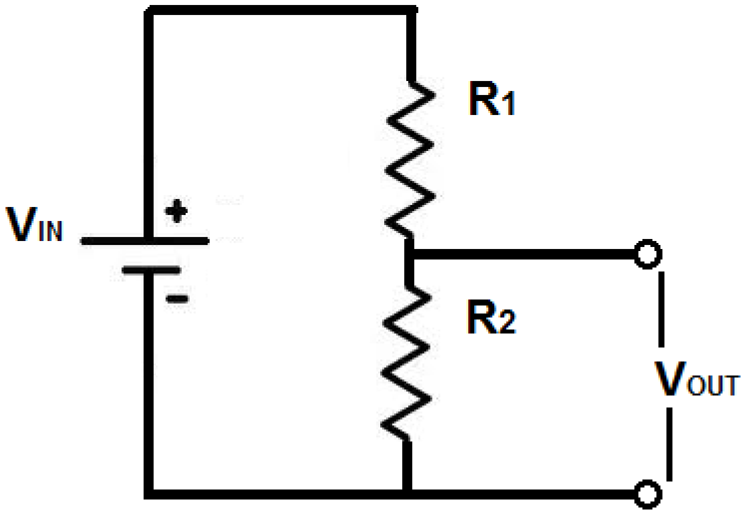

Figure 4.11 – Simple voltage divider.

Considering the maximum capacitor bank voltage used for creating the bead joint on the 0.51 mm K-type thermocouple is 40 V, the resistor arrangement ($R_1 = 1M\Omega$ and $R_2 = 330K\Omega$) ensures that the voltage across resistor R_2 remains below 10 V. Moreover, due to the extremely high equivalent resistance, the electrical current flowing through this path remains extremely low, thereby avoiding any compromise to the welding process current flow.

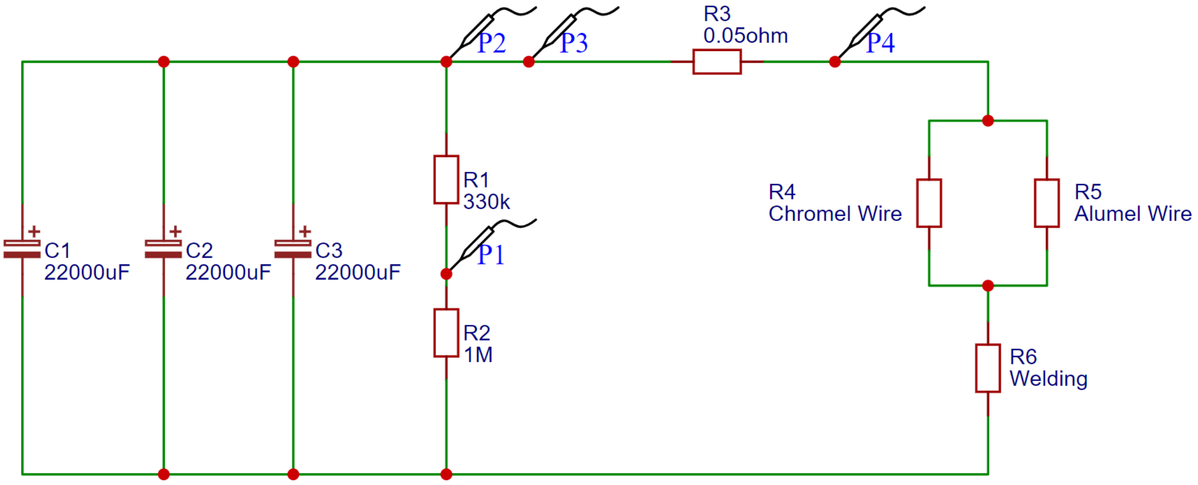

Figure 4.12 – Electrical design data acquisition.

4.5 Capturing the images during the bead formation

The high-speed camera can be used as a validation tool for measurements obtained through data acquisition, enabling a comparison between shape of the electrical arc and the evolution of the weld bead with the measured time and power evolution during the process. Additionally, the camera is used to take photos of the thermocouples, allowing for subsequent measurement of the thermocouples position, which collecting temperature along the wire. These measurements can be performed using ImageJ software, which calibrates the measurement system based on the number of pixels in a section with a known measurement in the image.

The captured images during the process can confirm the discharge time obtained through the electrical data. The observed electrical arc in the images can be compared with the power calculated from the electrical measurements. Two methods for capturing images of the process are presented. The first method involves adjusting the camera settings to capture the welding flash, allowing observation of the arc evolution and the bead formation during the flash or while it is illuminated, as shown in Figure 4.13. The second method places a light source behind the thermocouple, directed towards the camera, to create a silhouette of the thermocouple. This approach enables visualization of the metal forming the bead, as illustrated in Figure 4.14.

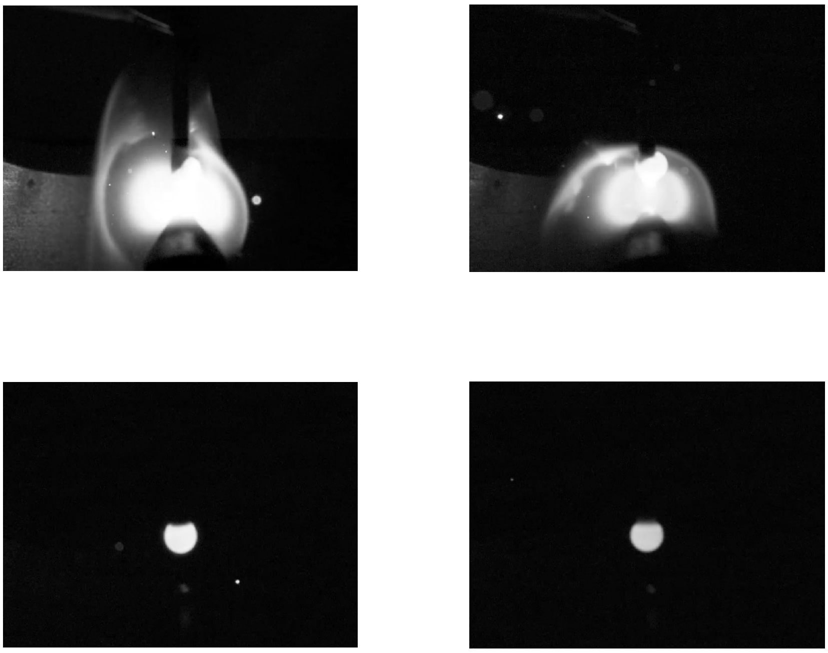

Figure 4.13 – Capturing the flash of the electrical arc.

4.6 Obtaining temperature data during the welding

Since the experimental temperatures helps to validate and refine the numerical model, experiments were performed to collect temperature data. Figures 4.15 and 4.16 show the experimental apparatus used to conduct the capacitor discharge welding process

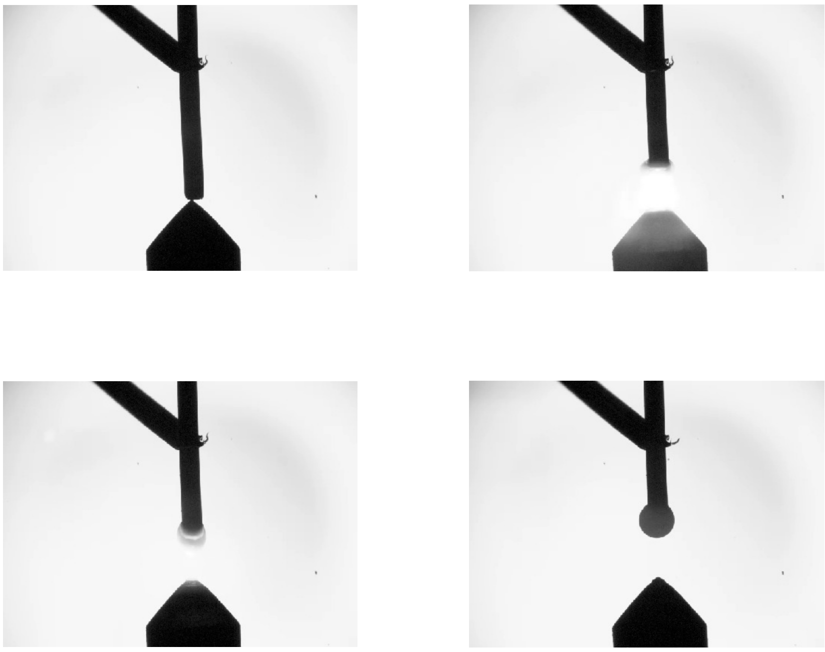

Figure 4.14 – Capturing the silhouette of the metal.

and collect temperature data. The setup includes a capacitor discharge welding machine, two measuring thermocouples (with diameters of 0.0787 mm or 0.254 mm), one 0.5106 mm diameter K-type thermocouple wire for welding, a microcomputer, and a data acquisition system. Initially, the measuring thermocouples are connected to the data acquisition system and then welded onto the 0.5106 mm diameter thermocouple wires, as depicted in Figure 4.16. To determine the distance between the measuring thermocouple position and the end of the wire, a camera captures the image shown in Figure 4.16. The ImageJ software is then used to perform the measurements, comparing the pixels with the known electrode size.

One method for measuring temperature using thermocouple wires is to produce a bead at the tip and collect temperature data from the bead itself (Figure 4.16). When the bead has a significant size relative to the surface, it may interfere with the heat flux. In such cases, the bead must be considered in the model, or the heat conduction caused by it must be accounted for. Another method involves welding the thermocouple wires at two points on the surface (Figure 4.17), measuring the mean temperature between these points. Since the model is symmetric, the temperature along the y-axis remains the same (isothermal), allowing for this configuration. In this setup, there may still be some heat flux through the leads, but it will be less significant than the first case. It is sometimes necessary to include the leads in the thermal model, in addition there might be potential differences along the wire, as they are in different positions, which could influence the temperature data from the thermocouples.

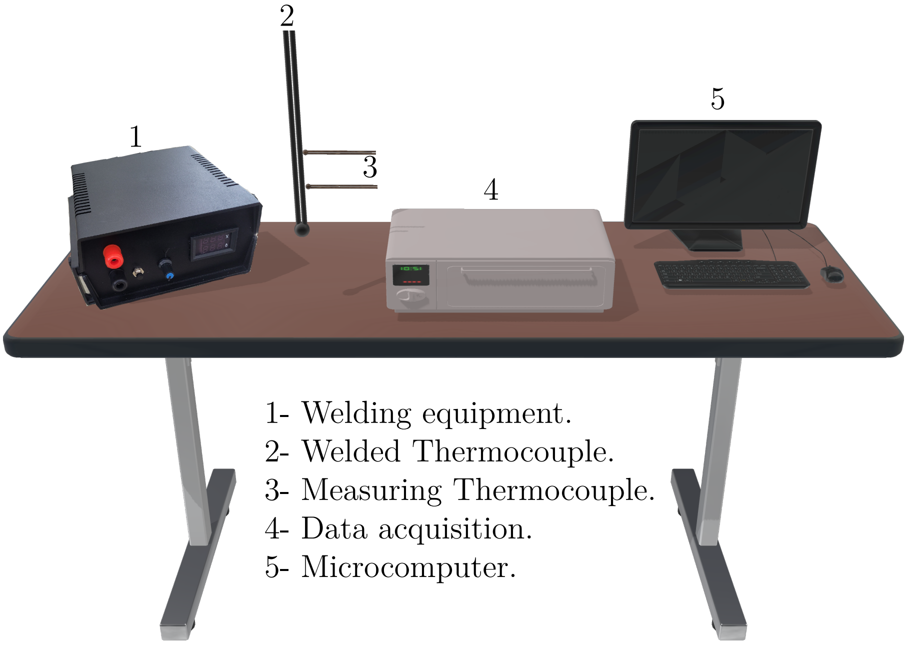

Figure 4.15 – Schematic of the experimental arrangement used to gather temperature measurements.

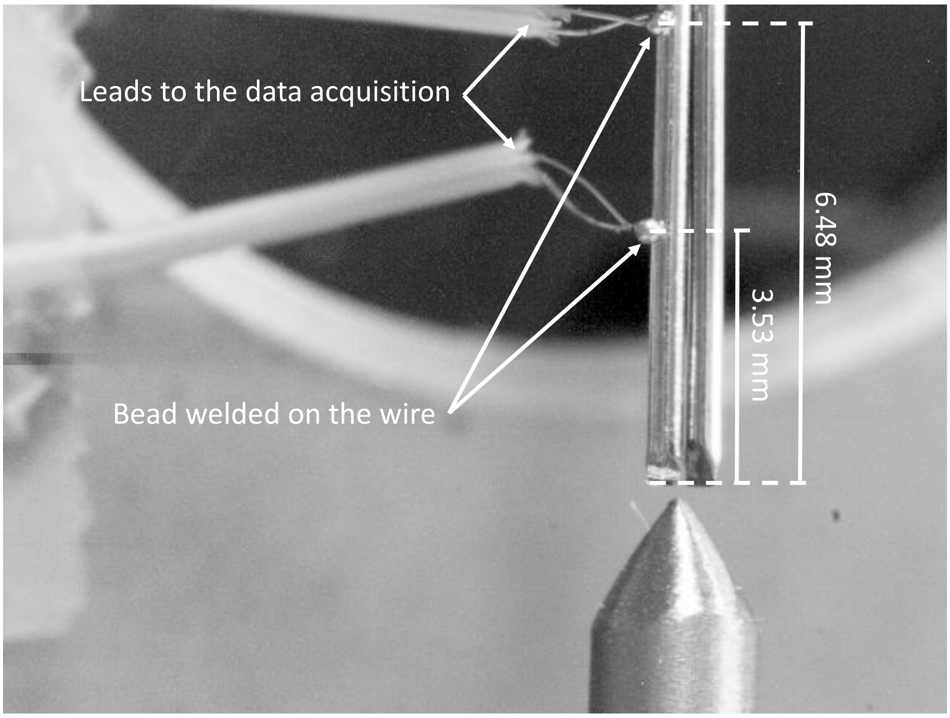

Figure 4.16 – Measuring thermocouples positioning in relation to the tip of the welded thermocouple.

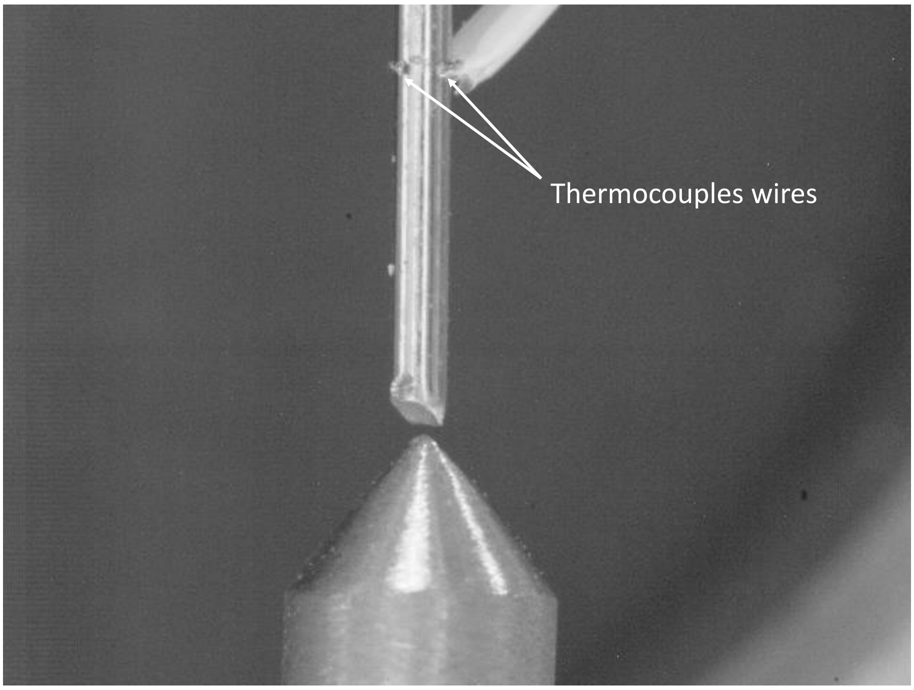

Figure 4.17 – Measuring thermocouple wires fixed in different point.

4.7 Resistivity Measurements

Due to the Joule heating effect in the wire during discharge, knowing the electrical resistivity of chromel and alumel as a function of temperature is important in this study. Electrical resistivity is defined as an ability of material to resist the flow of electric current. It is measured in ohm meters ($\Omega \cdot m$), while its inverse, electrical conductivity, is measured in siemens per meter (S/m). Resistivity is an intrinsic property of a material and does not depend on its size or shape, unlike electrical resistance, which is influenced by the length of material and cross-sectional area. The resistivity of steels primarily depends on their chemical composition. Minority atoms with different sizes from pure iron alter the mobility of free electrons in the steel. The atomic arrangement (crystal lattice), microstructure of the steel, and strain hardening (dislocation density) also affect its resistivity. As temperature increases, atomic thermal motion increases, making collisions with electrons more frequent and reducing the net movement of free electrons through a conductor. Consequently, resistivity increases with temperature.

The electrical resistivity measurements are performed using the four-wire method under controlled temperature and atmosphere (argon). This method allows for precise measurements of samples with low electrical resistance. In this study, measurements are conducted from room temperature up to 850°C for 35 mm long samples, and also for larger samples (110 mm) at room temperature to minimize uncertainty in the position of the measurement wires on smaller samples. The instrumentation used in the experiment, shown in Figure 4.18, consists of: 2 chromel wires introducing the current of intensity

I into the sample, represented as A and A'; 2 chromel wires placed at a spacing L_0 for measuring the potential difference U, represented as B and B'; and 1 K-type thermocouple fixed at the center of the sample to measure the temperature of wire, represented as TC.

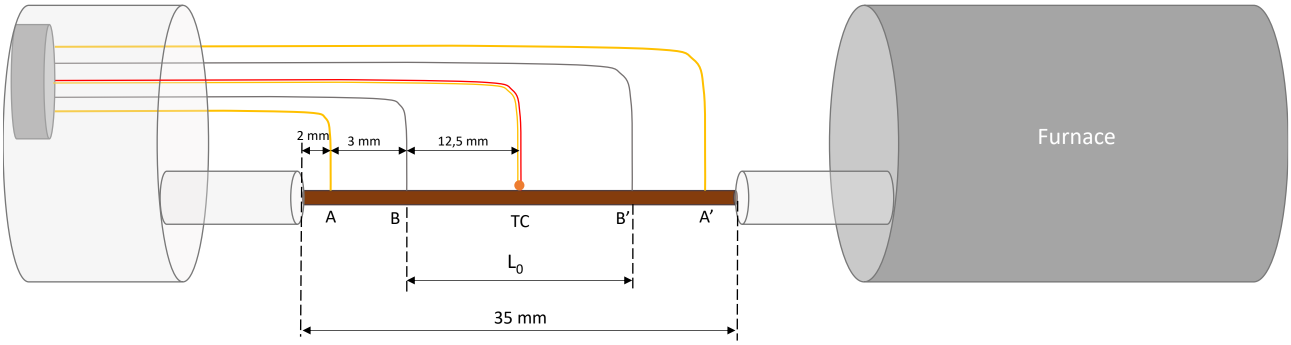

Figure 4.18 – Schematic of the four-wire resistivity measurement setup.

The instrumented sample is shown in Figure 4.19 in its quartz holder. The instrumentation wires are insulated with alumina, which not only ensures thermal insulation but also prevents any unintended contact between them, thus avoiding accidental short circuits. The 35 mm long sample is prepared by welding the instrumentation wires using a capacitor discharge welding device, and then inserted into a quartz sample holder. A tubular furnace with heating elements and an inner silica tube, as shown in Figure 4.19, is then slid over the sample. The tube is connected to the measurement apparatus via a steel flange. A primary vacuum is created in the tube, and argon flow is used to maintain the sample in a neutral atmosphere. The furnace temperature is monitored by a S-type thermocouple positioned in the holder next to the sample. A computer connected to a temperature controller allows for programming the desired thermal cycle.

The measurement current of 1 A is supplied by an Agilent E3644A 20V-4A power supply. The measurement current used is a square wave signal, as shown in the plot in Figure 4.20. The zero-intensity sequence allows for subtracting any thermoelectric effects caused by the differences in the materials of the measurement wires and the samples. The potential difference and sample temperature are measured using an Agilent E34970 data acquisition system, with the entire acquisition and calculations handled by a VBA program in Excel.

To determine the electrical resistivity, only the sample dimensions (length and diameter) and its resistance are needed. First, using Ohm's Law (Equation 4.1), the electrical resistance is calculated from the experimental current and voltage data:

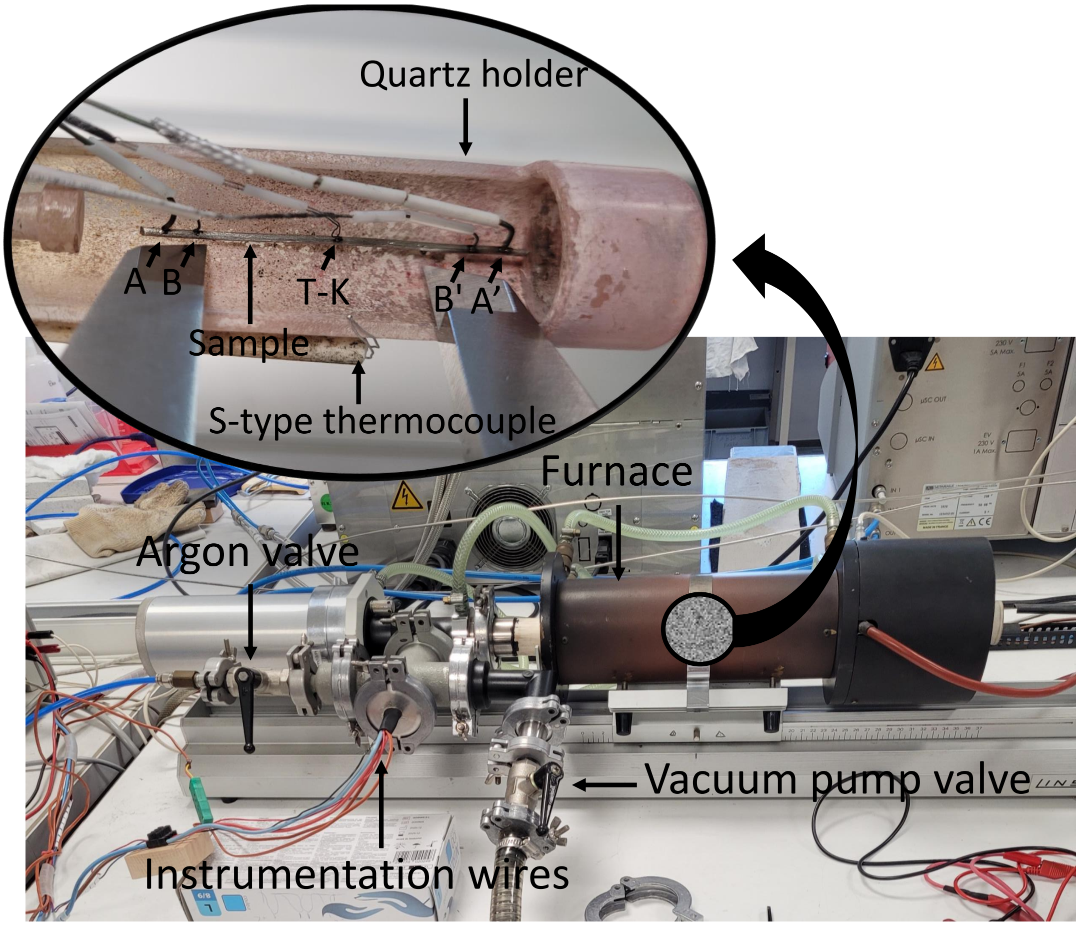

Figure 4.19 – Structure of the tubular furnace used in the experiment.

$$R = \frac{U}{I} \tag{4.1}$$

where U is the voltage measured by the data acquisition system and I is the current applied to the sample. The resistivity of the material is then calculated using Equation 4.2:

$$\rho = \frac{R \times S}{L_0} = \frac{U \times S}{I \times L_0} = \frac{U \times \pi \times D_0^2}{4 \times I \times L_0} \tag{4.2}$$

where R is the wire resistance, S is the wire cross-sectional area, L_0 is the distance between the voltage measurement wires, and D_0 is the wire diameter.

4.8 Elemental Composition Evaluation

In order to confirm the elemental composition of the bead formed during the CDW process, SEM analysis was performed on weld bead thermocouple specimens. The samples underwent conventional metallographic preparation, being hot-mounted in mottled bakelite powder (embedding polymer), followed by grinding with silicon carbide papers

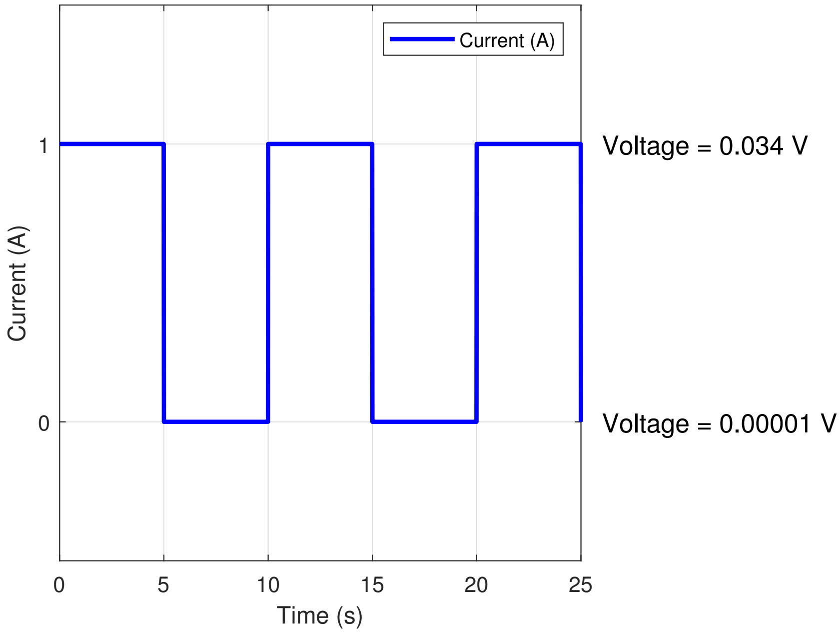

Figure 4.20 – Square wave current signal applied to the wire for the resistivity measurements.

ranging from 600 to 2000 grit and subsequent polishing with oxide polishing suspension (OPS) colloidal silica. The final result of the preparation is shown in Figure 4.21.

Figure 4.21 – Embedded samples after polishing process.

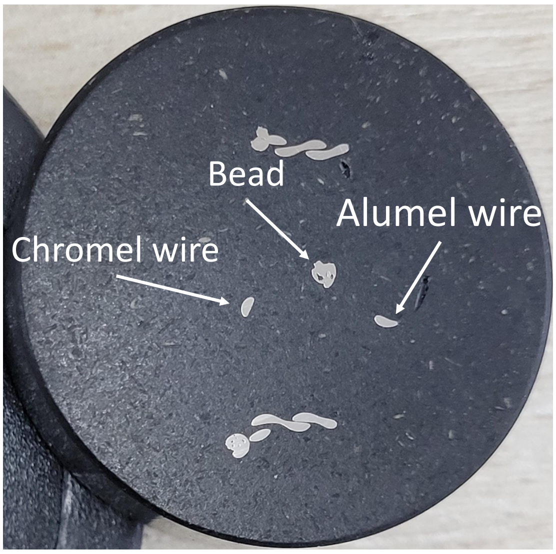

Source: Author.

The SEM analysis was conducted using a Carl Zeiss EVO MA15 microscope equipped with an EDS (*Energy Dispersive Spectroscopy*) detector (XFLASH 6—10). For the EDS analysis, rectangular regions of 200 µm × 286 µm (corresponding to an area of approximately 0.057 mm^2) were selected on the bead region of each specimen. These regions were used to perform the elemental mapping and identify the presence and distribution of the chemical elements in the fused area, allowing the assessment of possible alloying or contamination effects introduced during the welding process.

5 Experimental Results

5.1 Electrical quantities obtained of the one wire melting

In this section, it is presented the results of the electrical parameters gathered through the oscilloscope. Figure 5.1 shows the parameters during the process of melting one chromel wire. The initial voltage on the capacitor bank is 30 V, which discharges to 20 V when there is no longer contact between the electrode and the wire. Using the voltage data obtained from the resistor, it is possible to calculate the current through the process, given that the resistance is known to be 0.05 ohms. The maximum current in the circuit is 60 A, and the current decreases over approximately 20 ms until it reaches 0 A. The high current underscores the importance of considering the Joule effect on the wire, as the high current significantly influences the rapid temperature rise of the wire.

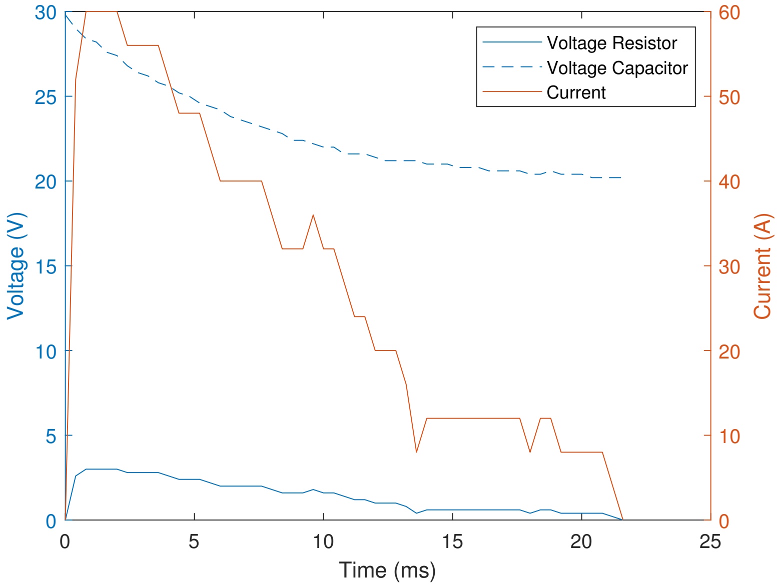

Figure 5.1 – Eletrical parameters obtained through the melting of chromel wire.

The electrical measurements obtained through the oscilloscope featured high temporal resolution, with a sampling interval of 0.4 ms. This allowed for a detailed analysis of the voltage and current transients during the capacitor discharge. In contrast, temperature measurements were acquired through a separate data acquisition system operating at a lower sampling rate. As a result, the two datasets cannot be directly compared on the same timescale. The oscilloscope data are suitable for analyzing the electrical behavior of the welding process, while the temperature data provide complementary information with lower temporal resolution. Despite this limitation, the electrical signals captured with the oscilloscope were essential for calculating the power delivered during the bead formation, as described in Section 3.2.2.

Figure 5.2 presents the calculated power results using the voltage data obtained through data acquisition. The equations used to calculate the power are detailed in section 3.2.2. By knowing the current in the circuit through the experimentally obtained voltages, it was possible to calculate the power in the wire fusion zone, labeled as welding power in the graph in Figure 5.2. This power is used for the thermal model calculations presented in the following sections. This figure also shows the total power obtained from the voltage evolution in the capacitor bank and the calculated current, the power across the power resistor (used to calculate the current), and the power across the wire determined from the known wire resistance and the circuit current.

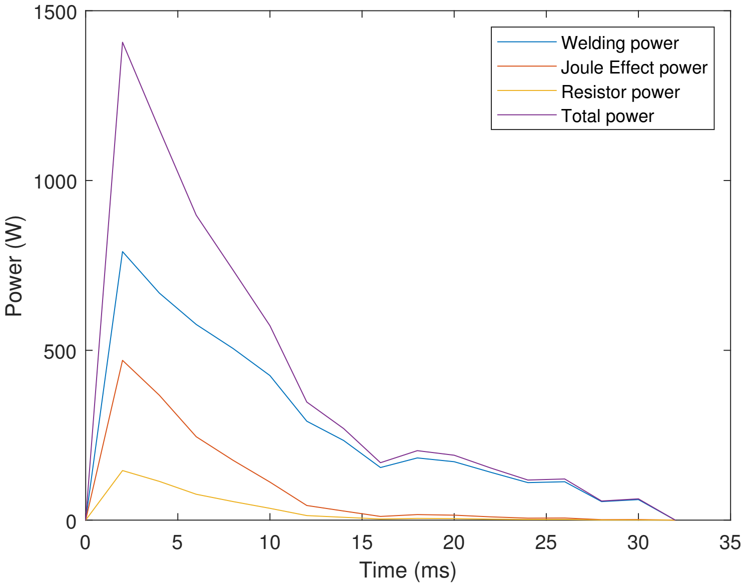

Figure 5.2 – Calculated power distribution during discharge.

These results help characterize how the electrical energy is distributed throughout the system during the discharge.

5.1.1 Thermocouples welding (40V)

This subsection presents the electrical parameters observed during the welding of two thermocouple wires using an initial capacitor bank voltage of 40 V.

Figure 5.3 displays the time evolution of the main electrical variables during the discharge. The capacitor bank voltage decreases exponentially from 40 V to 20 V, reflecting the typical behavior of an RC discharge. The circuit current starts at 158 A and decreases linearly to 0 A within 18 ms, which corresponds to the full discharge time. The voltage across the power resistor is also presented and was used to calculate the instantaneous current throughout the event.

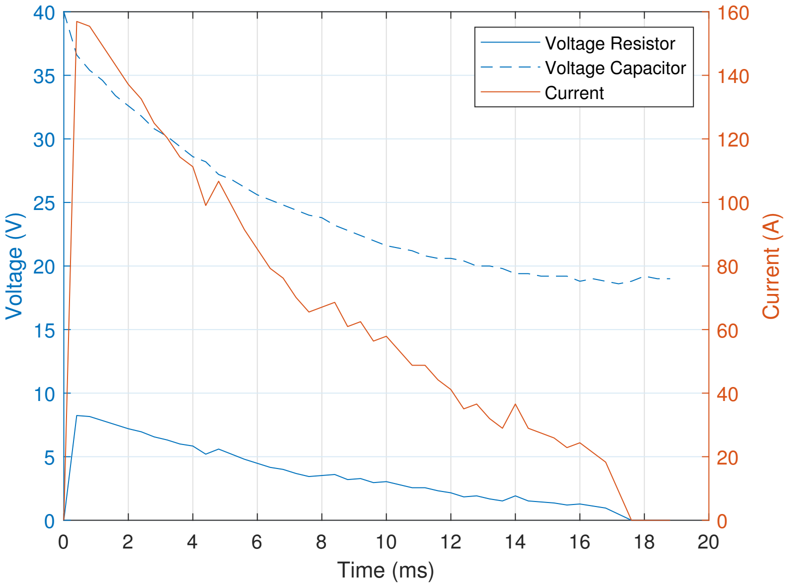

Figure 5.3 – Time evolution of electrical parameters during the discharge.

Figure 5.4 shows the power distribution during the same welding process. The total power delivered by the system initiates at approximately 6000 W and decreases exponentially to zero over the same 18 ms period. This curve characterizes the energy transfer from the capacitor bank. The figure also presents the power dissipated in the power resistor, the power dissipated across the thermocouple wire (calculated from the known wire resistance and current), and the welding power, representing the energy effectively used in the fusion zone.

These results demonstrate that the system is capable of delivering a high-energy pulse over a short time frame, making it suitable for welding thin thermocouple wires. The power concentration and its short duration are essential characteristics for achieving a localized and reliable fusion without damaging surrounding components or insulation layers.

5.2 Shape over time

The high-speed camera allowed visualizing the temporal evolution of the fusion process for two distinct configurations: melting a single chromel wire and welding two thermocouple wires. Figures 5.5 and 5.6 display selected frames captured during these processes.

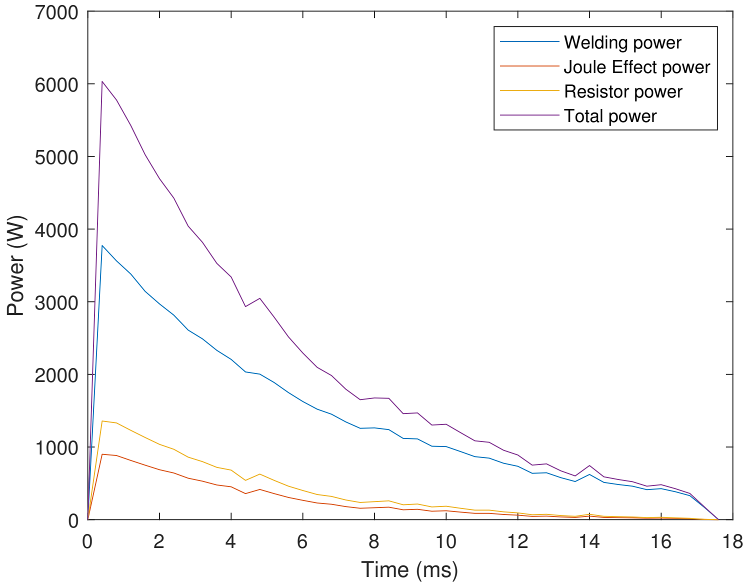

Figure 5.4 – Power distribution during the welding of two thermocouple wires.

Figure 5.5 presents a sequence of six high-speed frames illustrating the fusion process of a single chromel wire under a 30 V discharge. Each frame corresponds to a specific instant that reveals distinct physical phenomena during the formation of the molten drop. The wire undergoes rapid heating and localized melting at its tip due to the intense energy release from the capacitor discharge. Then, the wire tip gradually changes shape, transitioning from solid to a rounded molten drop before solidifying.

At 4 ms, the discharge initiates, and the arc is highly concentrated at the interface between the wire tip and the tungsten electrode. The energy begins to localize at the wire surface, initiating heating and early melting. By 14 ms, the arc has expanded spatially, and there is visible formation of molten metal. The wire begins to shorten due to melting, indicating active mass transfer from the solid phase to the molten region. At 28 ms, near the end of the electrical discharge, the molten sphere at the wire tip becomes well-defined and symmetrical. The arc is still present but more diffuse, and the energy input is decreasing. The molten drop exhibits a spherical shape, suggesting good surface tension effects and uniform heating. At 82 ms, with the arc extinguished, the molten sphere remains luminous due to residual thermal radiation. This frame allows clear visualization of the molten shape without the interference of the arc light. At 136 ms, the wire continues to contract slightly as the drop stabilizes. The brightness is reduced, but the molten sphere is still visible, indicating that the temperature remains high enough to sustain incandescence. Finally, at 244 ms, the sphere begins to darken and fade from view as it cools below visible radiation levels. The shape becomes indistinct, marking the end of the thermal event.

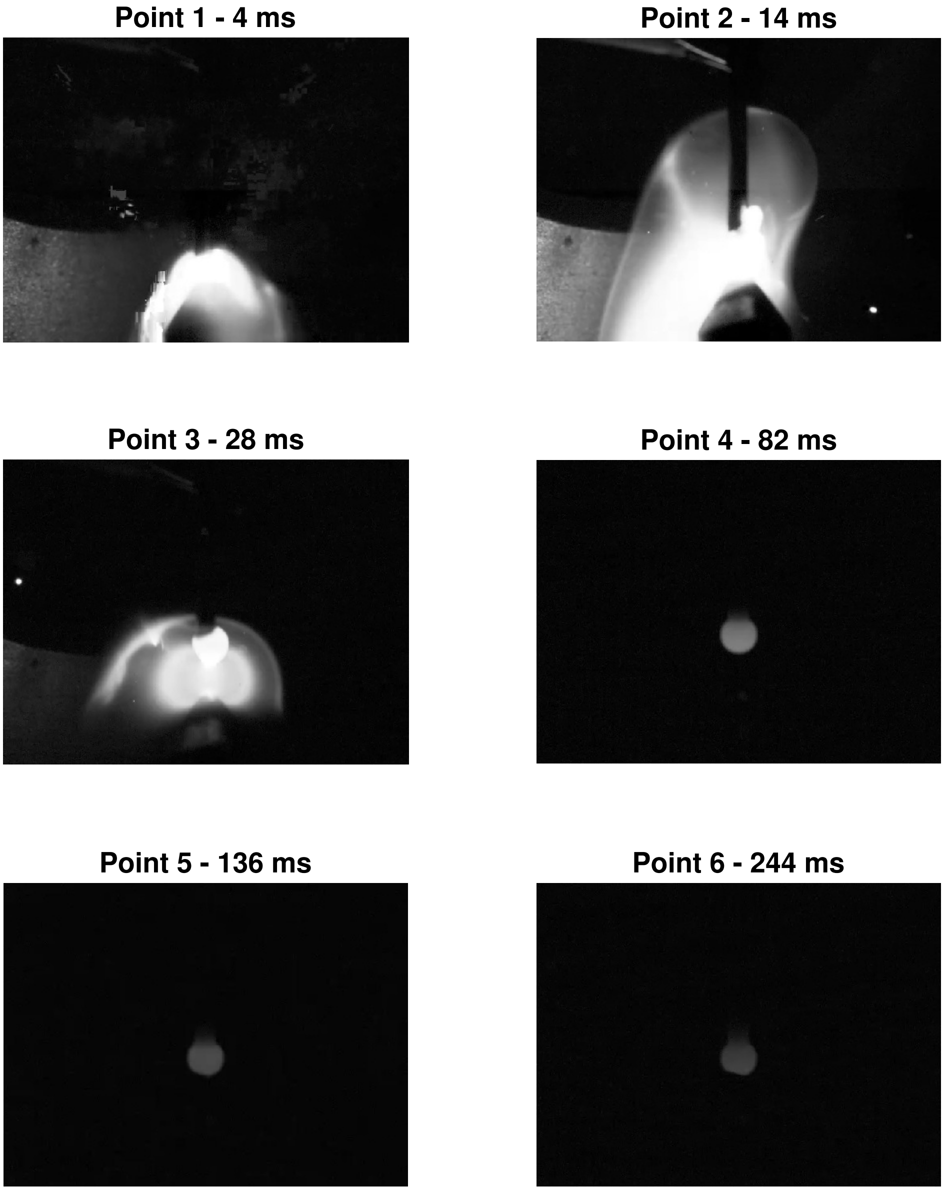

Point 1 - 4 ms

Point 2 - 14 ms

Point 3 - 28 ms

Point 4 - 82 ms

Point 5 - 136 ms

Point 6 - 244 ms

Figure 5.5 – High-speed frames of the melting process of a single chromel wire.

This sequence highlights the dynamic evolution of the fusion process, from arc ignition to the formation and stabilization of the molten drop. The symmetry and spherical morphology observed suggest favorable conditions for producing a consistent bead, essential for thermocouple junctions.

Figure 5.6 shows a sequence of high-speed images capturing the process of welding two thermocouple wires (Chromel and Alumel) during a 40 V capacitor discharge. The temporal evolution reveals stages of the electrical and thermal phenomena, from arc initiation to cooling of the molten junction.

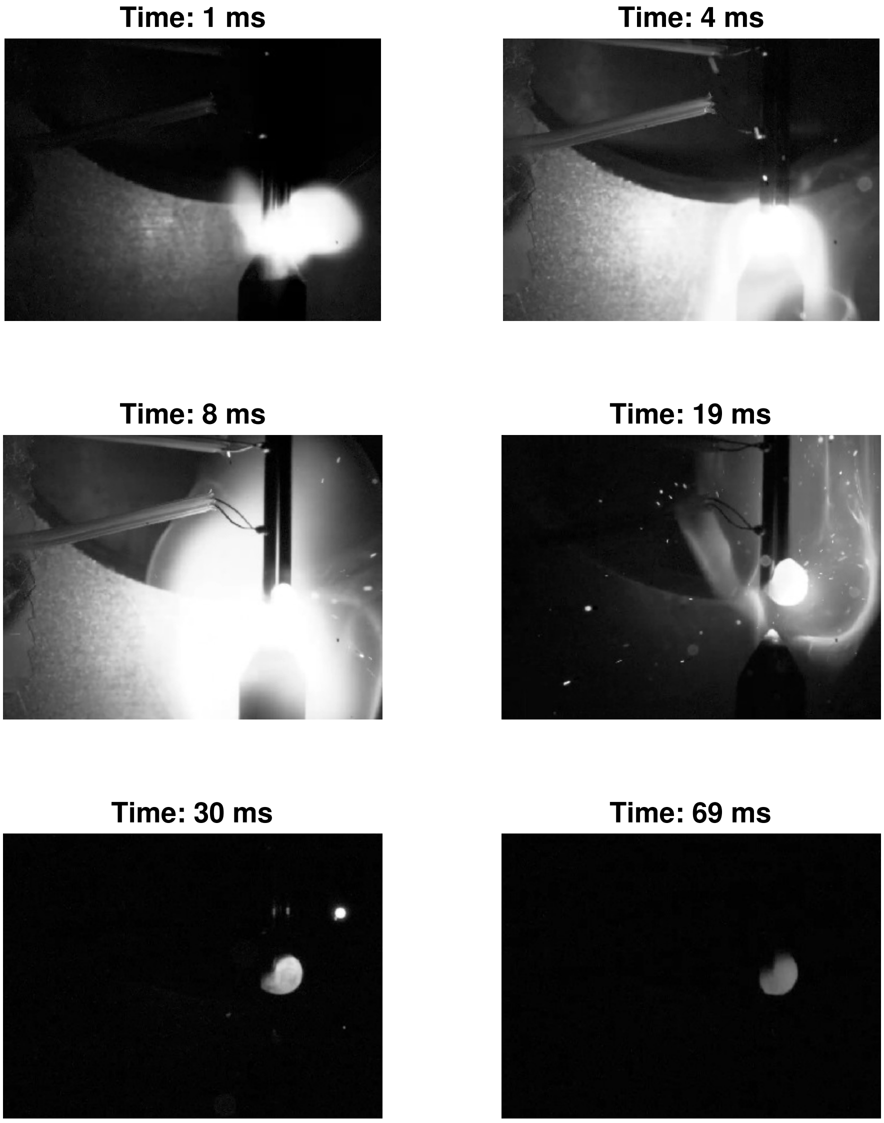

Time: 1 ms

Time: 4 ms

Time: 8 ms

Time: 19 ms

Time: 30 ms

Time: 69 ms

Figure 5.6 – High-speed frames of the thermocouple wire welding process.

At 1 ms, the first contact between the wires and the electrode occurs. A bright light is emitted, indicating the sudden initiation of the electrical arc and the rapid release of energy into the system. By 4 ms, the arc appears more concentrated near the electrode surface, and the initial shortening of the wires due to localized melting is visible. The current flow initiates heating, particularly at the contact region between the wires and the electrode. At 8 ms, a distinct molten bridge forms between the two wires, while the arc becomes more dispersed, extending over the surrounding area. The fusion zone becomes prominent as the heat generated leads to localized melting of both wires. At 19 ms, near the end of the discharge, the arc diminishes, but residual plasma and possibly metal vapor or smoke shadows can be seen. The molten region exhibits visible asymmetry, with a greater volume on the Alumel side. This is likely due to both the lower melting point and higher Joule heating in the Alumel wire, as it has lower electrical resistivity. At 30 ms, the fused region is still incandescent but begins to solidify. The bead now shows improved symmetry compared to earlier frames, indicating redistribution of the molten metal during cooling. Finally, at 69 ms, the junction loses brightness as the temperature drops below incandescence thresholds. The cooling solid bead is barely visible due to the lack of emitted light and the limitations of the imaging in low-light conditions.

This sequence demonstrates the complexity of the wire welding process, including arc dynamics, asymmetrical melting behavior, and solidification morphology. The differences in physical properties between Chromel and Alumel directly influence the bead formation and final junction geometry.

5.3 Discharge Time

This section presents a comparison between the electrical data acquired during the welding process and the images obtained through the high-speed camera. The objective is to validate the total discharge time of the capacitor bank and verify the temporal correspondence between the electrical signals and the physical events observed in the images.

Figure 5.7 shows four distinct moments of the welding process, correlated with the measured electrical data. Frame 5.7a shows the initial moment of the discharge, when the current reaches approximately 150 A (which may have occurred between 0.1 and 0.4 ms after the arc starts), marking the onset of the electric arc. This uncertainty is due to the difference in temporal resolution between the camera and the oscilloscope: the camera captures frames every 0.1 ms, while the oscilloscope samples at 0.4 ms intervals. The intermediate frames, 5.7b and 5.7c, correspond to the current decay phase. This behavior can be attributed to the shortening of the thermocouple wire during melting, which increases the resistance between the electrode and the wires, as well as the gradual reduction of the capacitor bank voltage during discharge. The electrical graphs associated with these intermediate frames also show the temperature evolution measured by the thermocouple closest to the fusion region. The temperature starts to rise shortly after contact begins, reaching about 65°C around 15 ms, indicating that the Joule effect is the main heating mechanism during this initial stage.

Finally, frame 5.7d shows the last moment (around 18 ms) in which the electric arc is visible, coinciding with the extinction of the current. The arc is interrupted due to a sharp increase in electrical resistance, caused by the separation between the electrode and the thermocouple wires. At this point, approximately 20V still remain in the capacitor bank, but this voltage is no longer sufficient to sustain the arc due to the high resistance in the circuit. This coincidence between electrical and visual events reinforces the reliability of the synchronization between the measured signals and the high-speed video recordings.

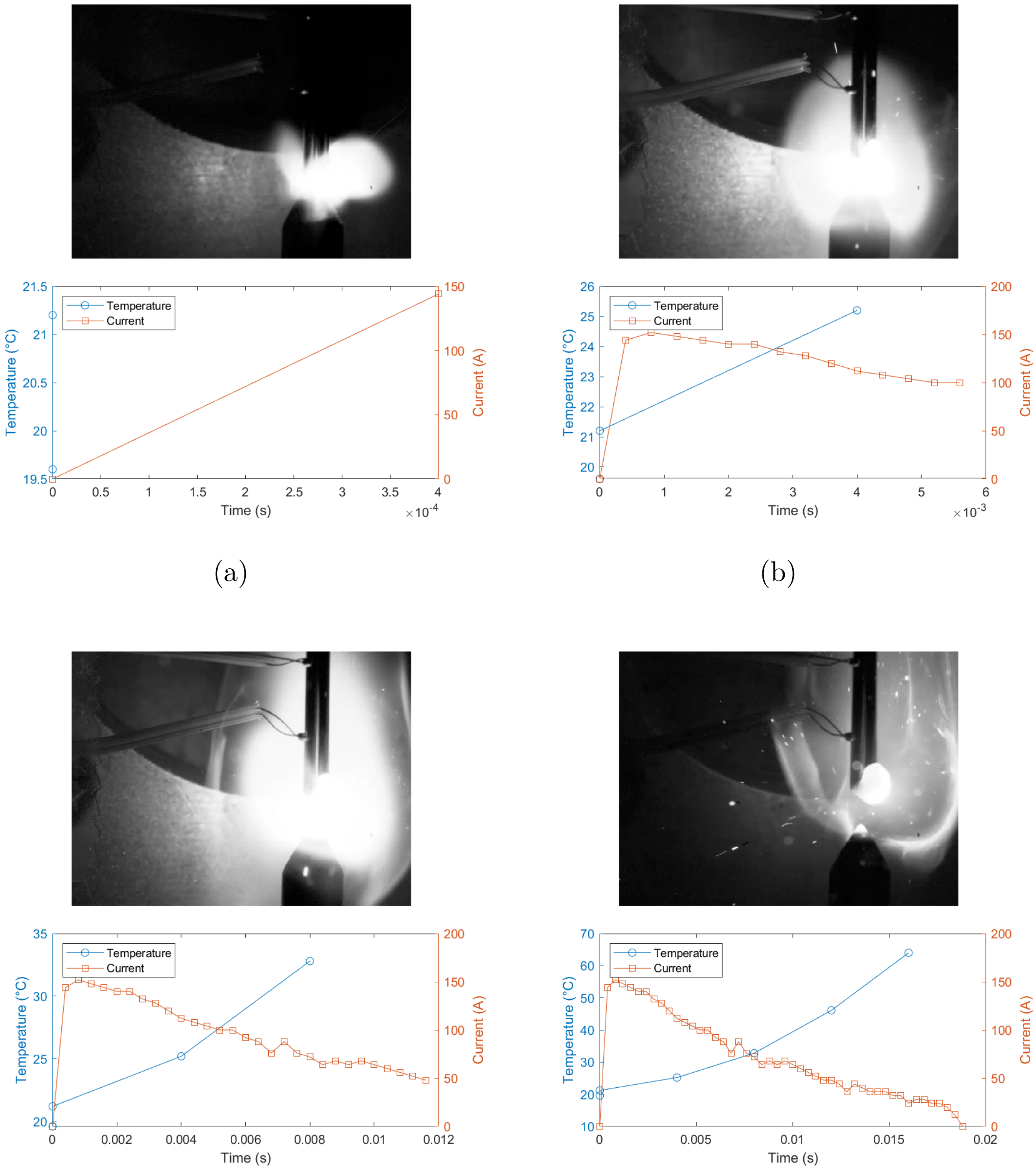

(a) (b)

(c) (d)

Figure 5.7 – Comparison between video and electrical measurements.

With this temporal alignment, it is possible to state that the electrical signals can be used as a reliable reference to identify physical events in the welding process, such as arc instabilities, melt pool formation, and droplet oscillation. Peaks or fluctuations in the power graphs can be directly correlated with changes in brightness or shape in the images, revealing thermal or mechanical oscillations during the process. Furthermore, this correlation enables automated analyses, such as identifying welding defects through anomalies in the electrical signal, without the need for continuous visual inspection. This represents an advancement for quality control in micro-welding processes.

5.4 Temperature During Melting of a Single Chromel Wire

The objective of studying the melting of a single chromel wire is to understand how the presence of the measurement bead influences the actual temperature readings. The temperature measured by the thermocouple bead will be compared with simulation data to validate the numerical model. With a simulation that closely matches the experimental data, it will be possible to use the model to estimate the actual surface temperature of the wire, rather than the temperature at the bead. After this validation, the heat flux absorbed by the bead can be estimated by simulating heat dissipation specifically in the region of the weld bead.

Temperature readings were obtained using the two experimental methods described in Section 4.6. For the purpose of comparing the data from these two methods, the thermocouples were positioned similarly in two different experiments, as shown in Figure 5.8.

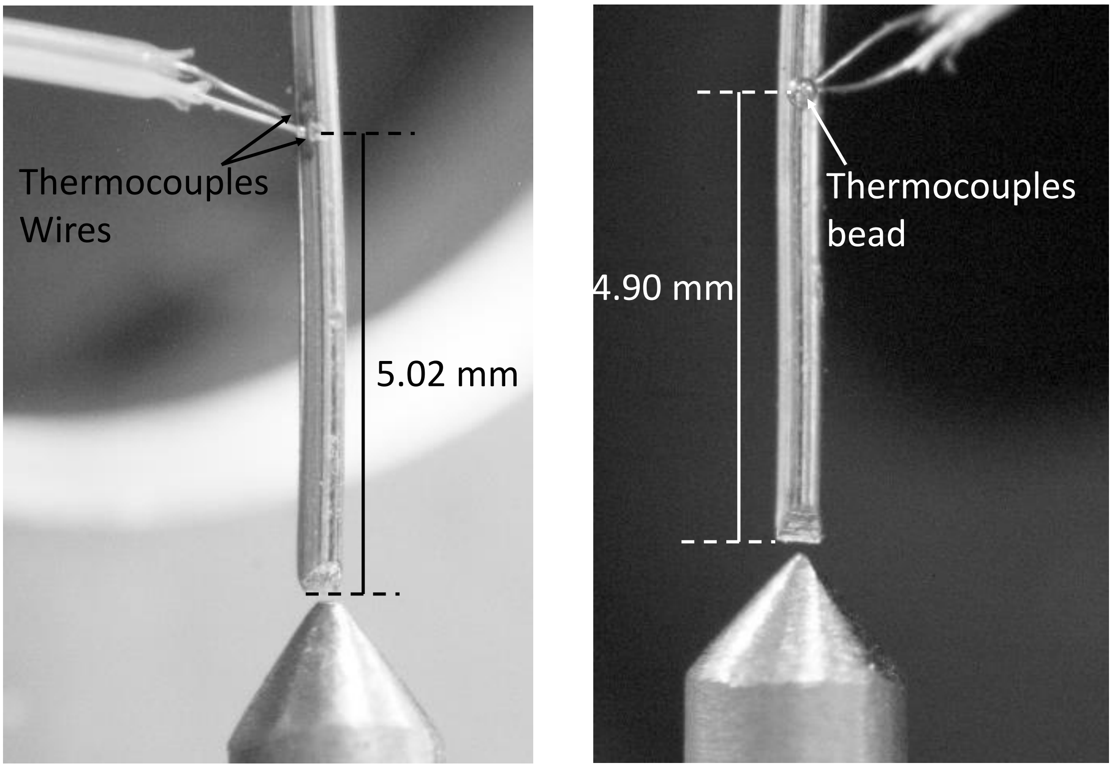

Figure 5.8 – Thermocouple wires fixed in different positions (Separated junction method) (right). Thermocouple wires fixed through the bead in the same position (left).

Figure 5.9 shows the results of the experiment using the separated junction method, which each wire was fixed in one side of the domain, as presented in Figure 5.8 (right). The graph, in Figure 5.9, presents the variation in temperature and voltage over time during the process. The six labeled points on the curve correspond to the moments captured in

Figure 5.5:

- Point 1 marks the beginning of the discharge.
- Point 2 occurs during the discharge.
- Point 3 represents the peak temperature during the final of discharge, when the welding arc is still active.
- Point 4 shows the bead still in the liquid phase, evidenced by its brighter appearance.
- Point 5 corresponds to the moment when the measured temperature reaches a minimum; at this point, the bead begins to lose brightness, indicating a drop in temperature.
- Point 6 shows the bead with almost no luminosity, while the measured temperature begins to rise again.

These points illustrate the various phases of the discharge and solidification of the weld bead.

An important observation in this graph is the rapid temperature rise between points 1 and 3, clearly highlighting the Joule heating effect. This heating coincides with the end of the electrical current in the circuit, as seen in the orange voltage curve. Between points 3 and 5, a rapid cooling effect is observed, which is likely due to heat conduction along the thermocouple wires, acting as fins and enhancing thermal dissipation. After point 5, the heat generated by the welding arc and droplet formation reaches the region where the thermocouple is located, causing a temperature increase that continues for approximately 1 second, as shown in Figure 5.9.

The graph presented in Figure 5.10 shows the measurement results, where Temperature 1 represents the data obtained with the thermocouple wires in different positions, and Temperature 2 represents the data obtained with the solder bead fixed on the surface. The Temperature 1 curve clearly shows the Joule effect present in the wire during the process, which is evident when analyzing the voltage curve that indicates the time during which the process is occurring and the wire is energized. The maximum temperature in this case is reached while there is still some current flowing through the process. Shortly after, the temperature begins to drop, not only due to the decrease in wire temperature by convection but also due to the heat flux along the thermocouple wires, which causes the temperature to decrease more rapidly. After this point, the heat generated by the melted weld bead flows to the wire, causing the observed region to increase in temperature again.

In the case of Temperature 2, the Joule effect is not as apparent. This is because the thermocouple does not read the surface temperature but rather its own bead temperature.

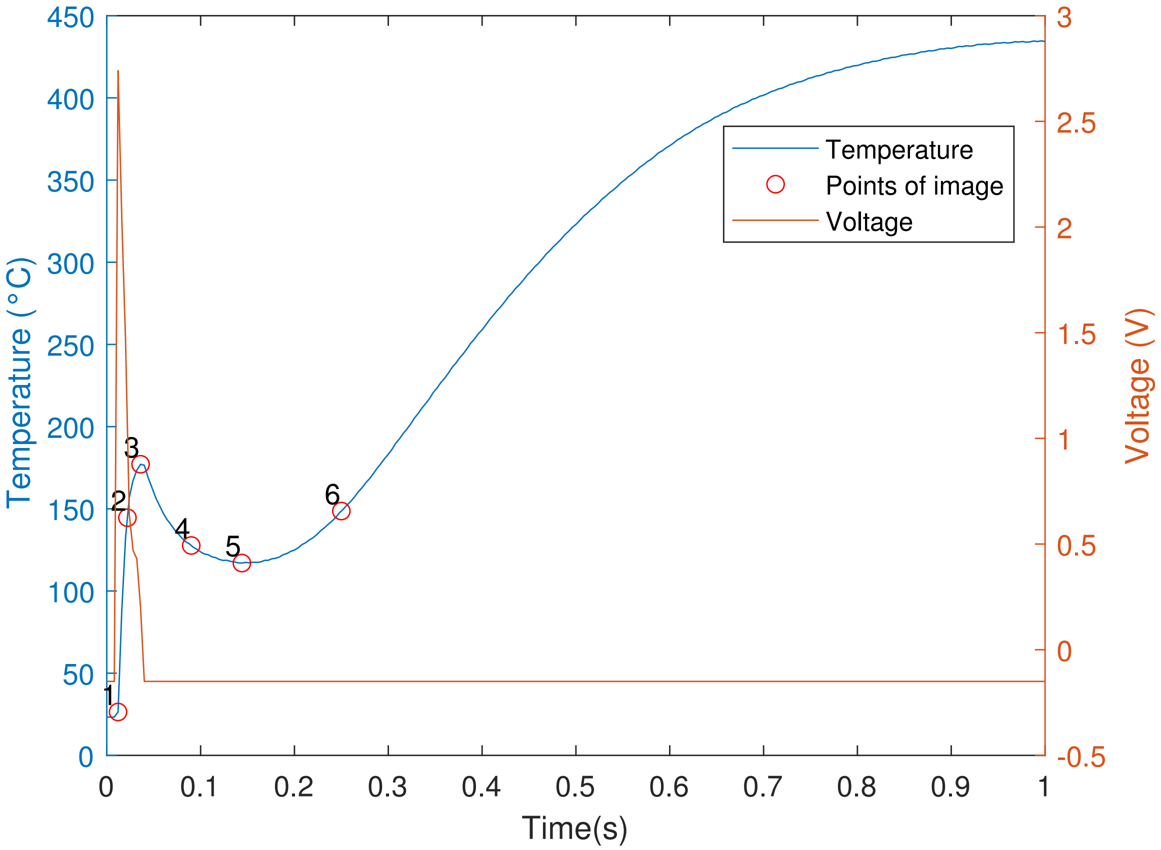

Figure 5.9 – Experimental temperatures measured by the 40 AWG (0.08 mm) thermocouples during the melting of the chromel wire (0.51 mm diameter), with 4 ms sampling interval.

In such a rapid effect, the bead does not heat up as quickly as the surface, causing a delay in the temperature response. Despite the difference at the beginning of the experiment, after the first few hundredths of a second, the temperature becomes consistent with the effect noted in the first case, as the difference between the temperatures may be related to a difference of position. In other words, the temperature does not exhibit abrupt changes as at the start of the process.

5.5 Experimental temperature welding thermocouples

In this section is presented the collected temperature data. First the previews experiments using the temperature reading in 90 ms interval, in theses experiments was used also thicker thermocouples for measure the temperature. The second section of experiments the reading intervals is 4 ms and the thinner thermocouples for measurements.

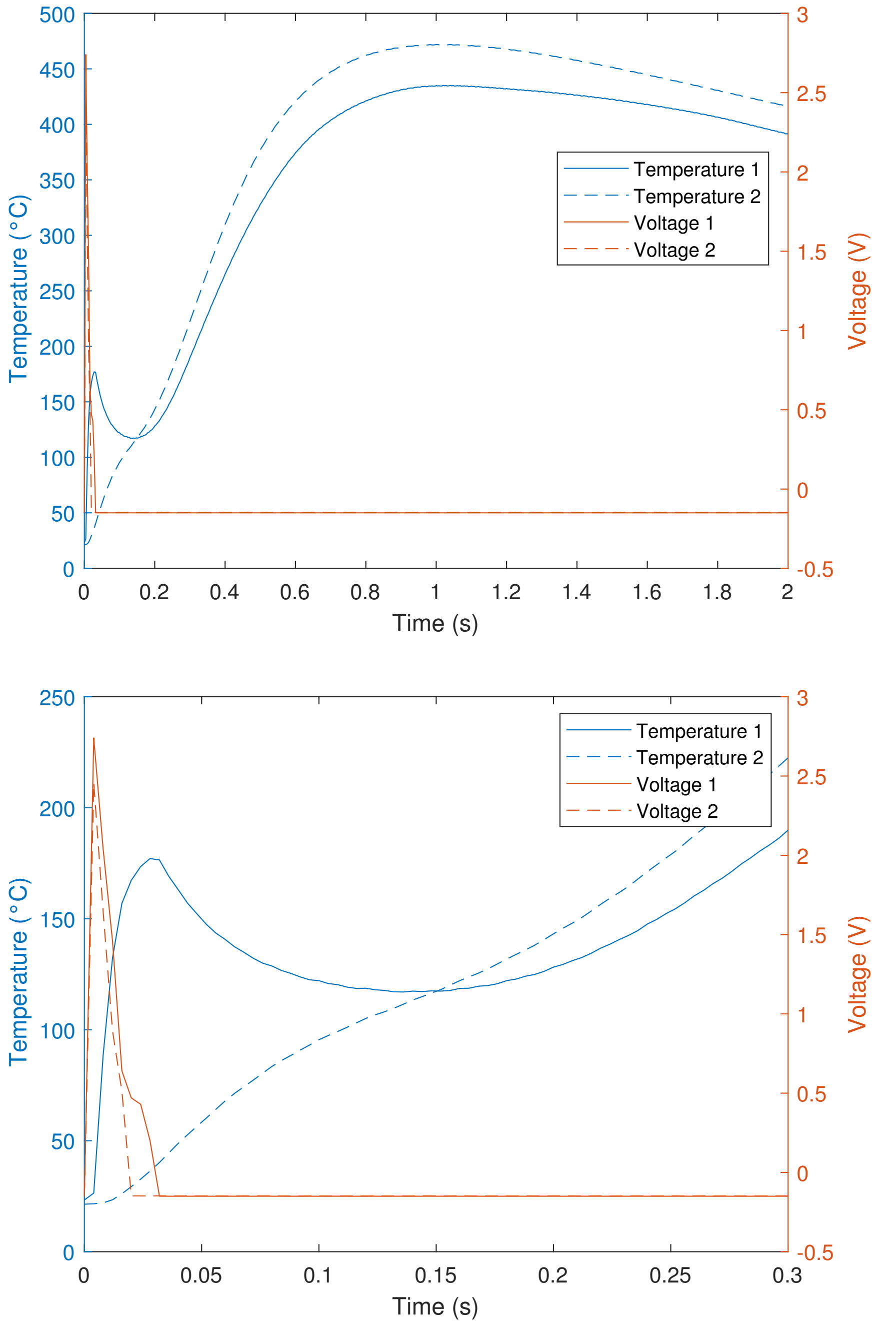

Figure 5.10 – Comparison between temperatures obtained by the two methods.

5.5.1 90 ms reading time step using 30 AWG (0.254 mm) measuring thermocouples

The data acquisition keysight 34980A was used for reading temperature data in 90 ms time step. The thermocouples used for these experiments was 30 AWG or 0.254 mm of diameter. This assembly is shown in Figure 5.11. The readings were started, and the tip of the 24 AWG (0.51 mm of diameter) thermocouple wire was subjected to a total energy input of approximately 38 J during the welding process using the capacitor discharge welding machine, resulting on the bead presented in Figure 5.11. The measurement process was halted after a few seconds, once the experimental process was completed. The temperatures were measured in regions approximately 2.00 mm and 4.70 mm from the end of the 24 AWG (0.51 mm of diameter) thermocouple.

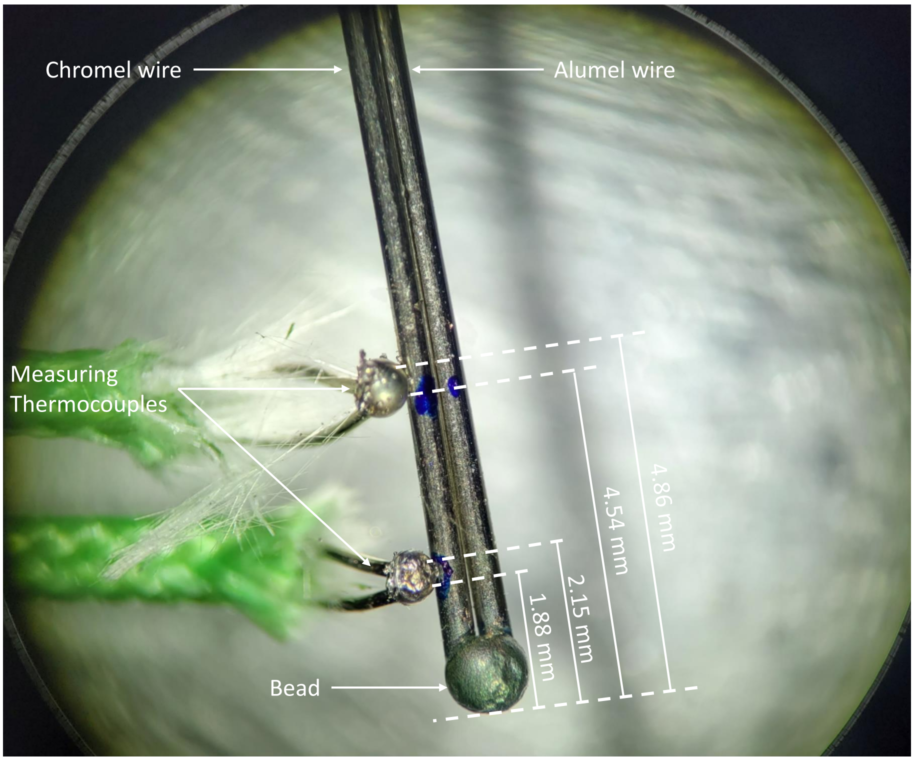

Figure 5.11 – 30 AWG thermocouples positioning in relation to the tip of the 24 AWG thermocouple.

5.5.2 4 ms interval reading using 40 AWG measuring thermocouples

The data acquisition DAQBOOK 2005 was used for reading the temperature data in 4 ms time step. The thermocouples used for these experiments was 40 AWG or 0.08 mm of diameter, around 3 times thinner than the experiment presented in the 5.5.1. This assembly is shown in Figure 5.13. The readings were started, and the tip of the 24 AWG thermocouple wire was subjected to a total energy input of approximately 38 J during the welding process using the capacitor discharge welding machine, resulting on the weld bead presented in Figure 5.13. The measurement process was halted after a few seconds, once the experimental process was completed. The temperatures were measured in regions approximately 2.29 mm and 5.25 mm from the end of the 24 AWG thermocouple.

5.5.3 Comparison

Figure 5.15 presents a comparison between temperature data obtained using thicker thermocouple (0.254 mm) with a reading time step of 90 ms (approach 1) and thinner thermocouple (0.08 mm) with a reading time step of 4 ms (approach 2). Although the

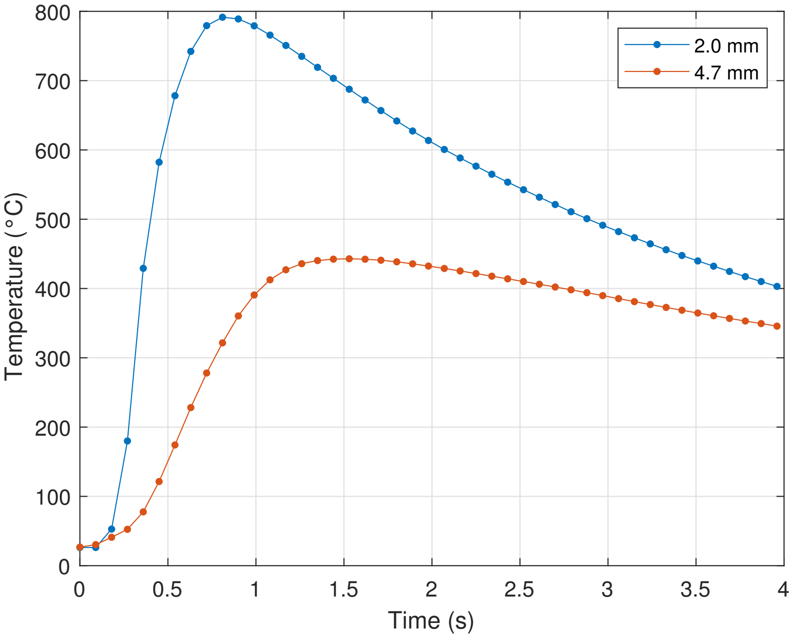

Figure 5.12 – Experimental temperatures measured by the 30 AWG thermocouples during the welding process, in 90 ms reading time step.

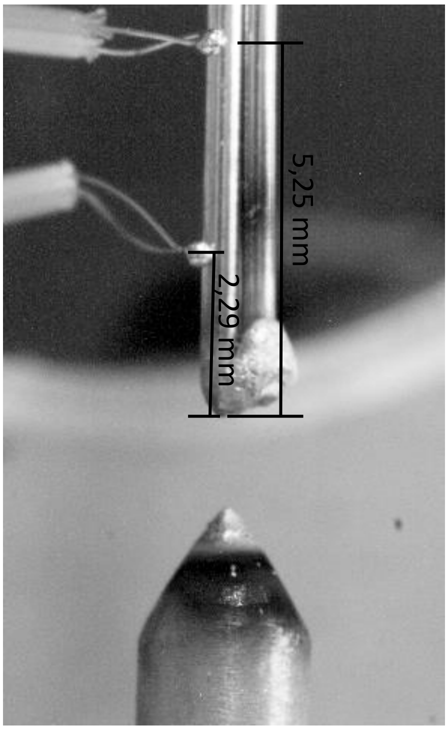

Figure 5.13 – 40 AWG thermocouples positioning in relation to the tip of the 24 AWG thermocouple.

positions of the thermocouple were not identical in both cases, the goal is to compare the temperature evolution between the two approaches.

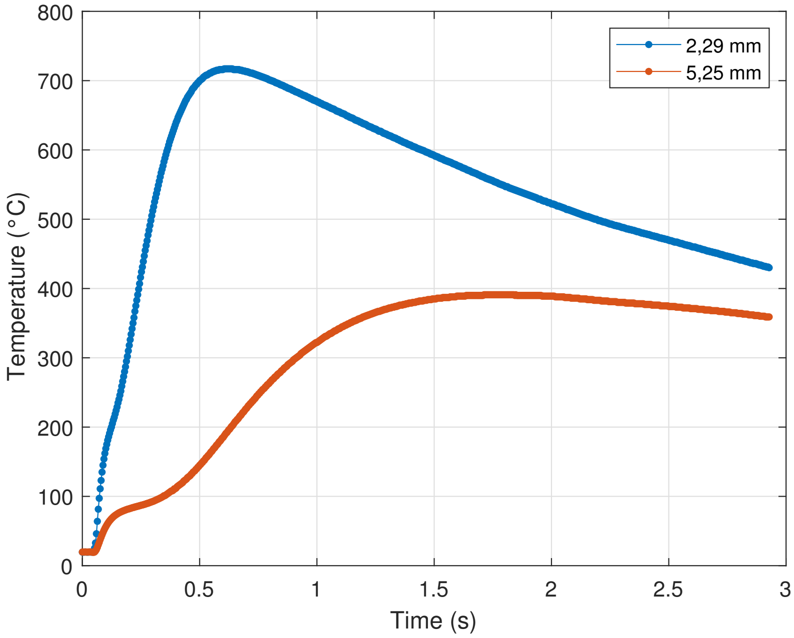

Figure 5.14 – Experimental temperatures measured by the 40 AWG (0.08 mm) thermocouples during the welding process, in 4 ms reading time step.

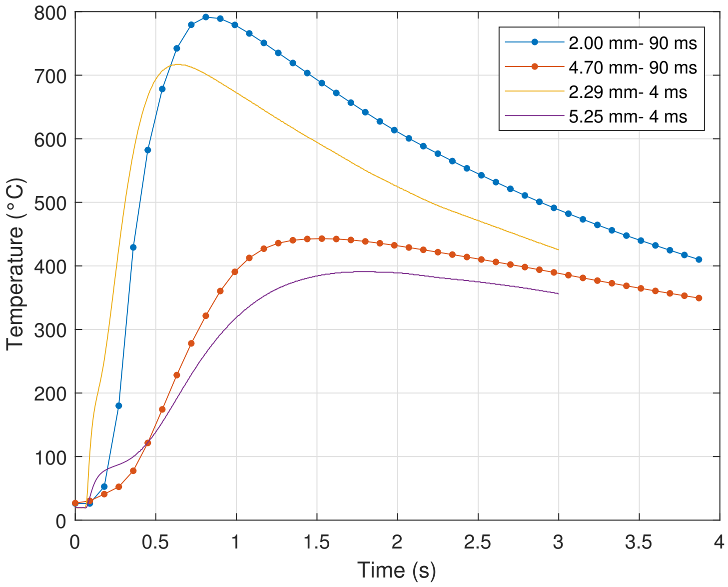

Figure 5.15 – Comparison between temperature read in 90 ms time step and 4 ms time step.

In approach 1, the thicker thermocouple and longer reading time step do not make clear the temperature evolution caused by the Joule effect, which occurs within the first 30 ms. The larger bead size of the thicker thermocouple results in a higher response time because the thermocouple measures the temperature of its bead rather than the surface temperature directly. This delay causes the quick temperature rise to be less noticeable.

In approach 2, the thinner thermocouple and shorter reading time step provide a clearer view of the temperature changes due to the Joule effect. The smaller bead size allows for quicker response times, enabling more accurate measurement of the surface temperature changes.

After the first few hundredths of a second, the beads in both approaches warm up and overcome their initial inertia. At this point, the temperature readings stabilize and align with the wire surface temperature. This results in similar behavior in both approaches, indicating that while initial readings may vary due to thermocouple thickness and response time, the long-term temperature trends are comparable.

5.6 Resistivity Measurements Results

This subsection presents the results of electrical resistivity measurements as a function of temperature and at room temperature. The temperature-dependent resistivity is used in the thermal model to calculate the heat generated by the Joule effect.

Determining the electrical resistivity at room temperature using a longer sample helped reduce uncertainty regarding the positioning of the voltage measurement wires. In this case, the wire sample can be longer than in the temperature-dependent measurements, so the effect of positioning uncertainty does not significantly affect the resistivity calculation. This will assist in accurately positioning the measurement wires later in smaller samples. The resistivity of chromel and alumel at room temperature (25 °C) was measured using a 110 mm wire length, yielding values of $7.10 \times 10^{-7}\,\Omega \cdot m$ and $2.71 \times 10^{-7}\,\Omega \cdot m$, respectively.

The graph of chromel resistivity as a function of temperature, from 25 °C to 850 °C, is shown in Figure 5.16. The electrical resistivity values range from $7.10 \times 10^{-7}\,\Omega \cdot m$ to $8.73 \times 10^{-7}\,\Omega \cdot m$. A non-linearity in resistivity as a function of temperature is observed around 500 °C during heating, which is not observed during cooling. After this observation, another experiment was conducted using the same sample, as presented in Figure 5.17. In this stage, the resistivity curves during heating and cooling remained similar, but with values corresponding to those from the cooling phase of the first experiment. This effect may also be a trick when measuring temperature using thermocouple of chromel and alumel, because as its resistivity changes after the first heating above 500°C, the calibration may change after first use in high temperature.

The graph of alumel resistivity as a function of temperature, from 25 °C to 850 °C, is shown in Figure 5.18. The electrical resistivity values range from $2.71 \times 10^{-7}\,\Omega \cdot m$ to $5.54 \times 10^{-7}\,\Omega \cdot m$. The behavior of alumel resistivity curve remained consistent during both heating and cooling. Alumel resistivity is more temperature-dependent than chromel, as observed in the graph, where the resistivity doubles between 25°C and 800°C, while

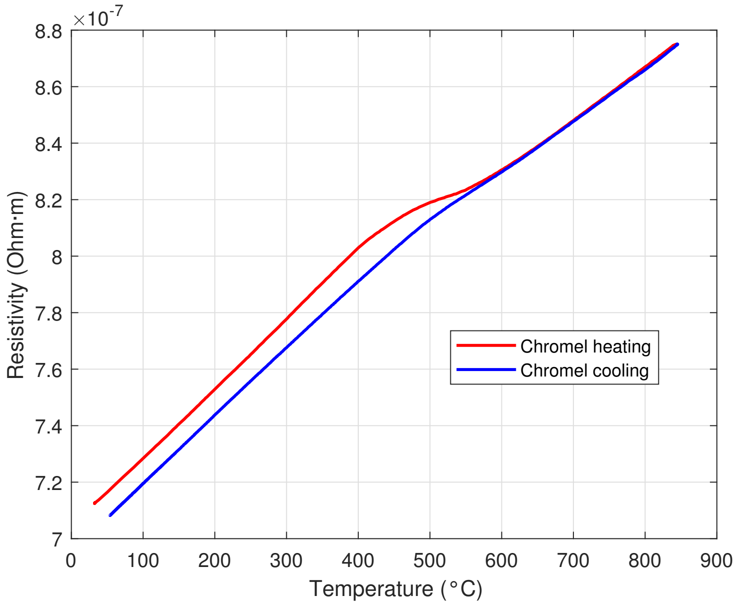

Figure 5.16 – Chromel resistivity as a function of temperature.

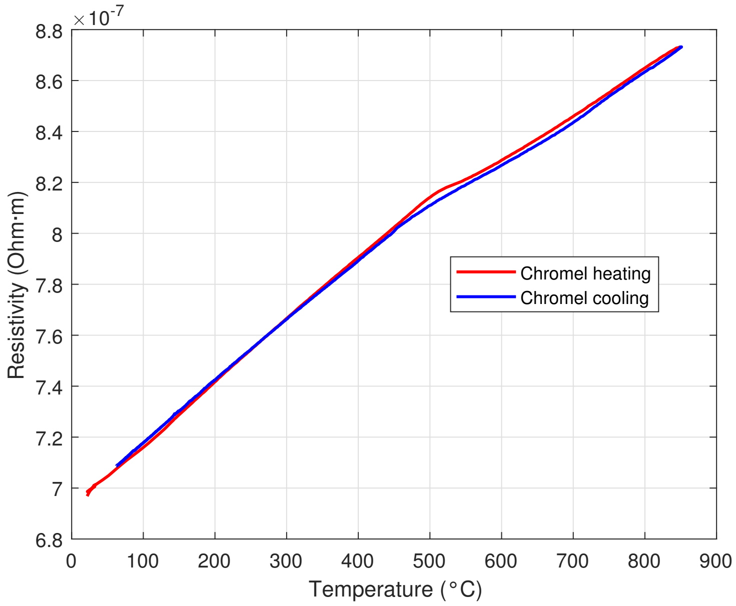

Figure 5.17 – Chromel resistivity during second heating.

chromel resistivity increases by about 22%.

The relative uncertainty of the calculated electrical resistivity is expressed as:

$$\frac{\Delta\rho}{\rho} = \frac{\Delta(\Delta U)}{\Delta U} + \frac{\Delta I}{I} + 2 \times \frac{\Delta D_0}{D_0} + \frac{\Delta L_0}{L_0} \tag{5.1}$$

The uncertainty in length L_0, which can be estimated as 1 mm due to the thickness of the measurement wire and instrument error in distance measurement, is independent

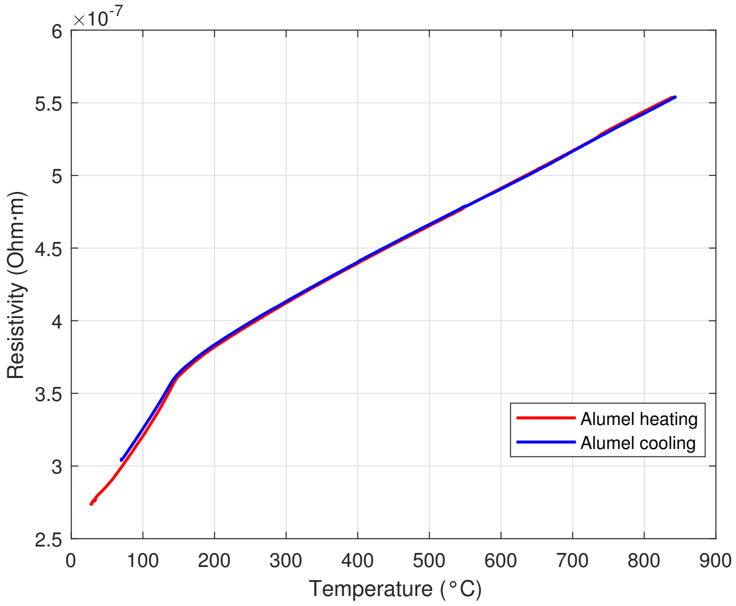

Figure 5.18 – Alumel resistivity as a function of temperature.

of the sample size. This represents 0.9% for 110 mm samples, resulting in an uncertainty of 0.9% in the electrical resistivity result. If this measurement were directly applied to smaller samples used in temperature-dependent experiments, it would result in 2.8%.

Uncertainties in electrical measurements are evaluated based on the characteristics of the measurement devices. For the uncertainty in the potential difference ΔU, the device measurement range (0.1 V) is considered. The uncertainty in the potential difference ΔU is given by:

$$\Delta(U) = 0.003\% \times U + 0.003\% \times (\text{Measurement range} = 0.1V) \tag{5.2}$$

In the worst-case scenario, at room temperature: $\Delta U = 0.002\,V$. The resulting relative uncertainty is less than 0.2%. Meanwhile, the uncertainty in the current measurement is given by:

$$\Delta I = 0.15\% \times I + 0.005 \tag{5.3}$$

The measurement current is constant and equal to 1 A: $\Delta I = 0.0065\,A$, which corresponds to 0.65%. Overall, the total uncertainty is approximately 4% for room temperature measurements and 5% for high-temperature measurements.

5.7 Energy Dispersive Spectroscopy results

In the EDS analysis, an initial global verification of the weight percentages of the constituent elements was conducted. The chemical compositions were obtained from five rectangular regions of 200µm × 286µm across the midplane bead region, as shown in Table 5.1. For statistical analysis, the average of these five points was calculated and is presented in the "Average"column of Table 5.2. The theoretical values, shown in the "Theoretical"column, were calculated assuming an ideal 50% chromel and 50% alumel mixture.

Table 5.1 – **Analysis of the compositions by EDS (Bead).**

Element	R1 [wt.%]	R2 [wt.%]	R3 [wt.%]	R4 [wt.%]	R5 [wt.%]
Al	1.24	1.33	0.93	2.44	2.01
Si	0.84	0.92	0.64	0.72	1.85
Cr	4.58	4.44	4.43	4.50	5.12
Ni	93.19	92.67	93.39	91.11	90.18
Mn	0	0.63	0.62	1.25	0.83

Table 5.2 – **Statistical Analysis.**

Element	Theoretical [wt.%]	Average [wt.%]	p-value
Al	2.10	1.59	0.13
Si	0.94	0.99	0.818
Cr	4.59	4.61	0.862
Ni	91.74	92.11	0.588
Mn	0.63	0.67	0.867

When comparing the average results with the theoretical expectations, the data shows overall agreement, suggesting that the bead composition consists approximately of equal parts chromel and alumel. This equivalence was confirmed by a one-sample t-test, and the resulting p-values (Table 5.2) are all greater than 0.05, indicating that the measured compositions are statistically consistent with the theoretical mixture.

However, it is worth noting that the average aluminum (Al) content was lower than the theoretical value (1.59% vs. 2.10%). Despite not being statistically significant ($p = 0.13$), this discrepancy may indicate a physical phenomenon occurring during the process. One explanation is the partial loss of aluminum due to its relatively high vapor pressure and low boiling point compared to the other elements present. During the welding process, localized temperatures are extremely high and can exceed the boiling point of aluminum, promoting its evaporation from the molten region. Additionally, the small volume and rapid solidification of the bead (in the order of milliseconds) may limit the reabsorption or redistribution of vaporized aluminum. These phenomena can lead to a measurable depletion of Al in the solidified region, as captured by the EDS analysis.

In addition to measuring the chemical composition of the bead, the composition of the thermocouple wires was also analyzed. Table 5.3 shows that the measured compositions for Al, Si, Ni, and Mn in Alumel are very close to their theoretical values, with p-values indicating no statistically significant differences.

Table 5.3 – **Analysis of the compositions by EDS (Alumel).**

Element	R1 [wt.%]	R2 [wt.%]	Average [wt.%]	Theoretical [wt.%]	p-value
Al	3.54	2.15	2.34	2	0.821
Si	1.28	1.59	1.43	1	0.218
Ni	93.79	94.97	94.38	95	0.48
Mn	1.24	1.29	1.26	2	0.06

Similarly, Table 5.4 presents the measured compositions for Al, Si, Ni, and Cr in Chromel. While there are slight discrepancies, particularly for Al and Si, the p-values again suggest that these differences are not statistically significant. The presence of Al and Si in Chromel, which are theoretically absent, might be attributed to minor contamination during sample preparation or residual elements from the manufacturing process. Additionally, the measured levels of silicon (Si) are very low and close to the detection threshold of the EDS equipment, suggesting that they could also stem from instrumental noise rather than actual material content.

Table 5.4 – **Analysis of the compositions by EDS (Chromel).**

Element	R1 [wt.%]	R2 [wt.%]	Average [wt.%]	Theoretical [wt.%]	p-value
Al	0.81	1.91	1.36	0	0.15
Si	0.3	0.37	0.33	0	0.066
Ni	89.55	88.64	89.09	90	0.297
Cr	9.28	9.08	9.18	10	0.077

These results suggest that the manufacturing processes for Alumel and Chromel wires ensure a consistent alloy composition. The alignment between measured and theoretical compositions is critical for ensuring the reliability and accuracy of thermocouple readings, particularly in high-precision applications. Any significant deviation in composition could alter the thermoelectric properties of the wires, potentially leading to measurement errors.

Furthermore, these findings validate the quality of the thermocouples used in the experiments, confirming that they meet the expected standards. This validation is essential for the credibility of subsequent thermal modeling and simulations, which rely on accurate material properties to correctly predict temperature distributions and heat fluxes.

6 Heat transfer model results

This chapter presents the results of the thermal models applied to the fusion of a single Chromel wire and to the fusion of thermocouple wires. It includes the estimation of heat flux during the welding process and the comparison of results obtained through different temperature measurement methods. Additionally, modifications made to the thermal model are discussed, and the welding efficiency is calculated based on the estimated thermal input and material response.

6.1 Heat transfer in single chromel wire

Two approaches were used to consider the heat flow in this case:

The first one is the heat flux entering the wire through the wire cross-sectional area, bottom.

$$P_{Total} = q_1 A_1 \tag{6.1}$$

The second one is heat flux in the wire cross-sectional area generated by part of the power represented by P_1 and also on the side due to the plasma, represented by P_2, from the position of 0 mm to 2 mm from the end of the wire, modeled as a Gaussian function. This heat flux is defined by Equation 6.4:

$$P_{Total} = P_1 + P_2 \tag{6.2}$$

$$P_{Total} = q_1 A_1 + q_{initial} \pi D \int_0^2 e^{-\frac{y^2}{a}} dy \tag{6.3}$$

$$q_2 = q_{initial} e^{-\frac{y^2}{a}} \tag{6.4}$$

Where a is a constant defining the shape of the function, and $q_{initial}$ is the heat flux at the point $y = 0$, calculated from the total power in the lateral region of the wire (P_2). This power was considered half of the total power. Power 2 is defined by the heat flux q_2 multiplied by the surface area of the wire. As the wire surface area is cylindrical, π was used, diameter, and the length of the region represented in the integral form, described in Equation 6.5.

$$P_2 = q_{initial} \pi D \int_0^2 e^{-\frac{y^2}{a}} dy \tag{6.5}$$

Thus, it is possible to calculate $q_{initial}$ for each power variation, as:

$$q_{inicial} = \frac{0.5P_{Total}}{\pi D \int_0^2 e^{-\frac{y^2}{a}} dy} \tag{6.6}$$

With these equations, we can obtain the evolution of the heat flux on the wire, presented in Figure 6.1. Using the experimental power data, the heat flux shape was calculated for each 0.4 ms.

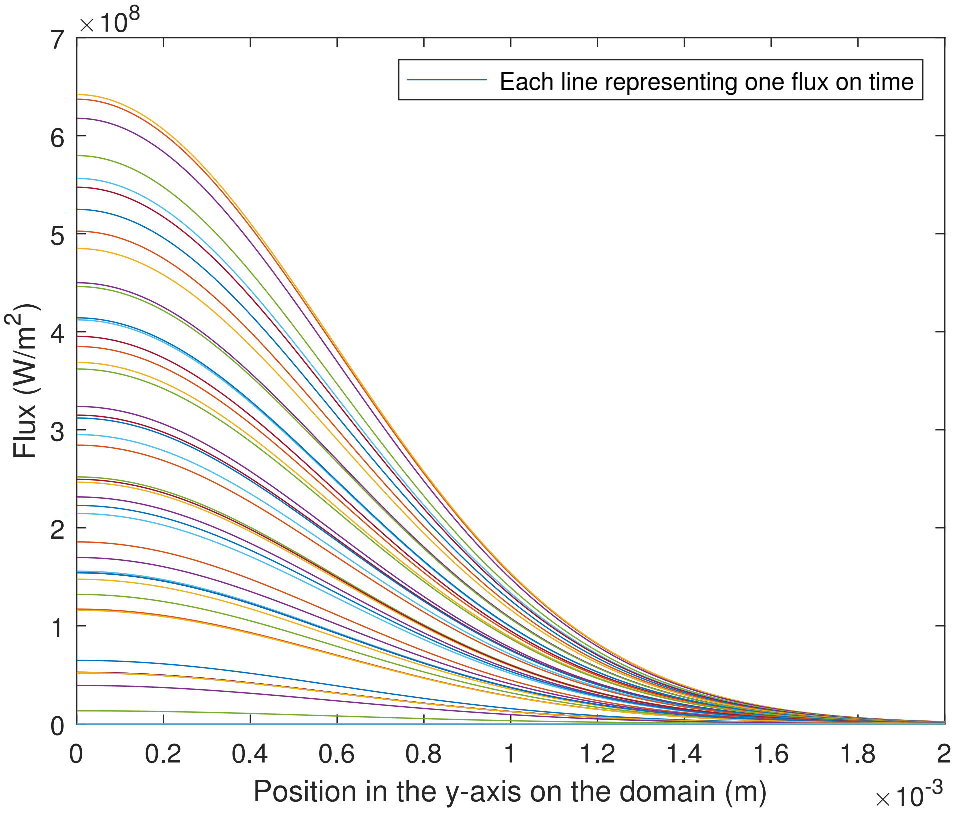

Figure 6.1 – Profile of the calculated heat flux.

The thermal model used to calculate temperatures during the melting of a single chromel wire is presented in Figure 6.2. To account for the influence that the wires may have on the temperatures in the desired region, the model includes not only the melted wire but also the measurement thermocouples and their beads, as shown in Figure 6.2. In this figure, point 1 represents the calculated temperature on the wire surface, and point 2 represents the temperature at the thermocouple bead. The thermal properties used in the model calculations were outlined in section 3.2, precisely the Figure 5.2. The welding power was obtained through the calculations presented in section 5.1. The thermal efficiency considered for this case was 45%. Stenbacka [42] conducted a literature review on published efficiency values for Gas Tungsten Arc Welding and estimated the average arc efficiency to be around 77%. In the case of Plasma Arc Welding, an average arc efficiency of 47% was observed [43]. DuPont and Marder [43] suggest that consumable electrode processes show higher efficiency than non-consumable electrode processes, due to the transfer of energy from the moving electrode to the substrate. Moreover, the low efficiency of the process can be explained by the large dissipation of energy through light and noise during the process. So, in the thermal model, the heat rate was considered 45% of the welding power calculated.

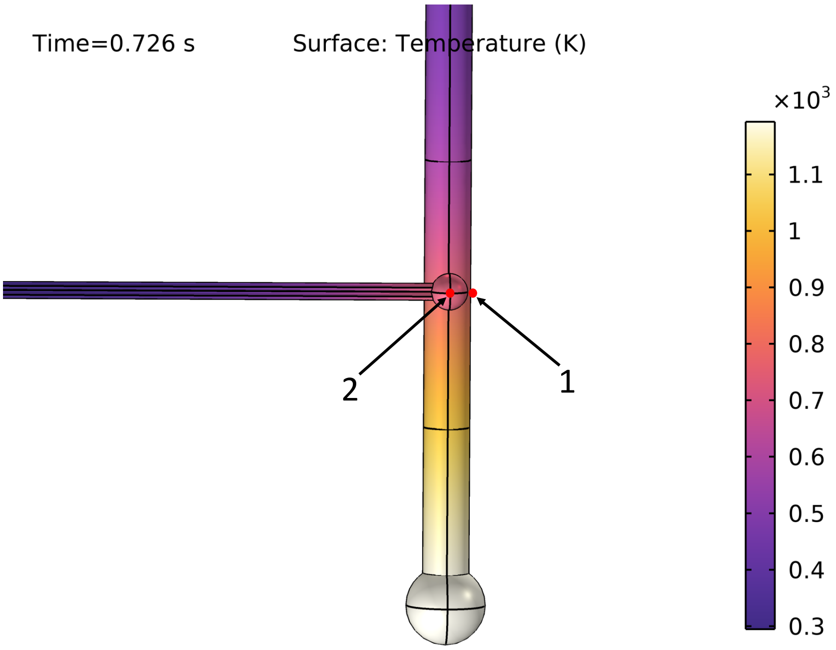

Figure 6.2 – Thermal model representing the one wire melting.

The positioning of the thermocouple in the model was defined to approximate the experimental measurements. Since the position of the thermocouple varies from the start of the process until the complete solidification of the bead, the position considered in the thermal model is when the discharge ends. At this moment, the distance between the electrode and the bead is 0.90 mm, as shown in Figure 6.3. These measurements were performed using an image comparator, made possible by the known electrode diameter of 2.42 mm. After comparing the right side of the Figure 5.8, the position of the thermocouples in the model is considered 4 mm from the bead.

The calculation results are presented in Figure 6.4. These results emphasize the importance of considering the effect of the thermocouple bead on the temperature readings. The calculated temperature at the measurement bead closely matched the experimental temperature, with only a small discrepancy likely due to the model not accounting for contact resistance.

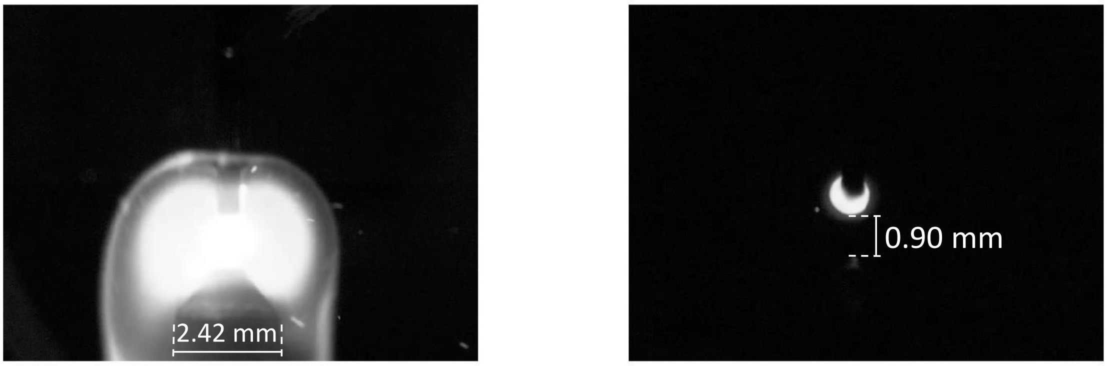

Figure 6.3 – Bead position used in the thermal model.

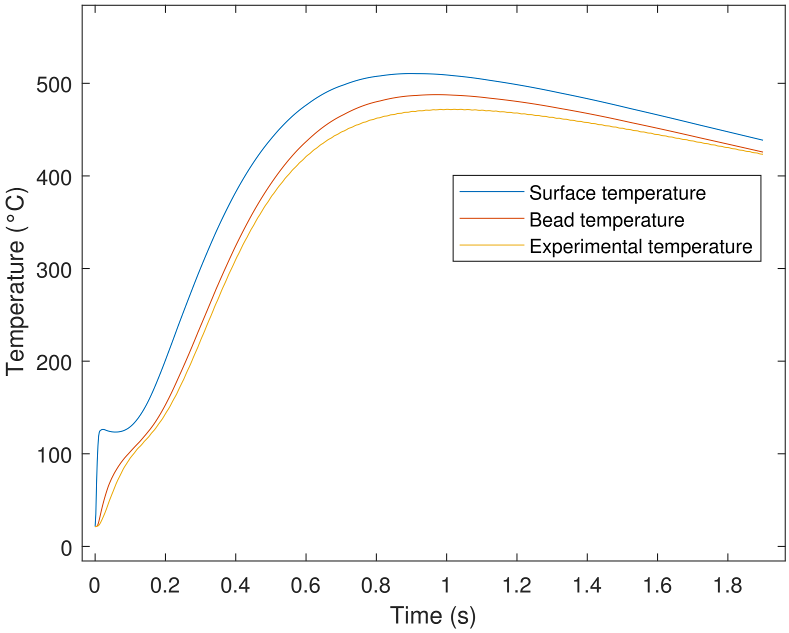

Figure 6.4 – Comparison of bead temperature, surface temperature, experimental temperature.

6.2 Heat transfer in two thermocouple wires

In Figure 6.5 is shown the geometry of the thermocouple with welded joint, which was used in the three-dimensional thermal model. In this model, the welded end of the thermocouple is subjected to a transient heat source, employed through the capacitor discharge. This heat flux fuses the two wire ends, where phase transformation occurs and a welded sphere is formed. The whole model is subjected to the initial temperature T_0.

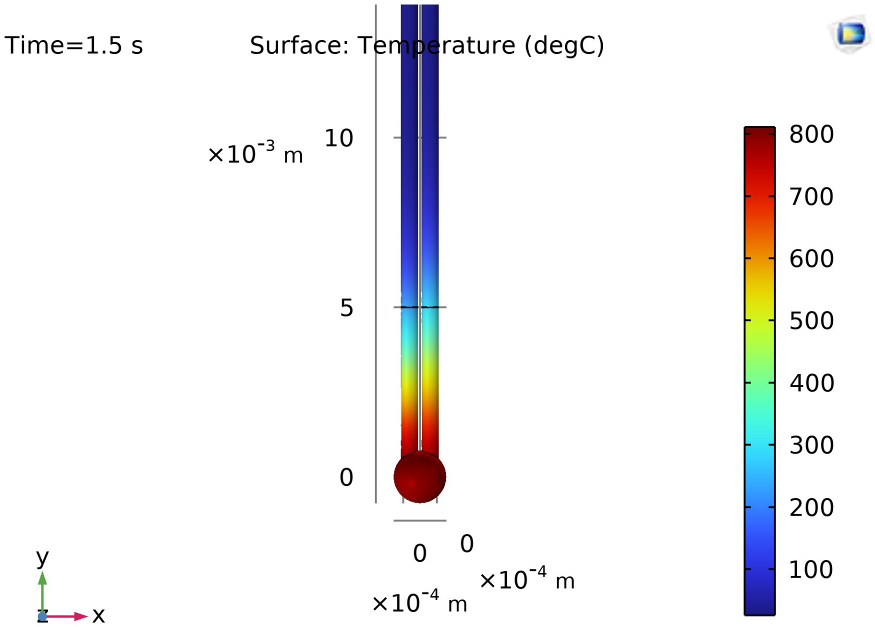

Figure 6.5 – Three-dimensional thermal model representing the thermocouple with welded bead.

6.2.1 Estimating using the 90 ms reading time step experiments

The heat rate employed in the welding process was estimated by the non-linear Function Specification Method, using the experimental temperature obtained in section 5.5.1. For this analysis, the smoothing parameter, r, was set as three. Examining the regularization parameter r is crucial to prevent substantial oscillations or overly regulated estimated functions, which might not accurately represent the problem. With an increase in the number of future data points, the estimated heat rate becomes more regularized. However, this may result in a greater difference between the experimental and the calculated temperatures [44].

The maximum value of $\hat{Q}$ was 25 W. The heat rate reaches its maximum value between 0.36 and 0.45 seconds and returned to zero by 1.6 seconds. The estimation results are depicted in Figure 6.6.

To calculate the welding process efficiency, it was necessary to calculate the energy generated by the estimated heat rate, measured in Joules. This energy can be calculated either by measuring the area under the graphic in Figure 6.6 or by integrating the estimated heat rate over time, resulting in 11.30 J.

Figure 6.7 illustrates a comparison between experimental and calculated temperatures, using the estimated heat rate and the residuals between the experimental and numerical temperatures are also displayed. The average residual during the first second of process was 13 °C, the standard deviation of 13.48 °C and the maximum residual reaches

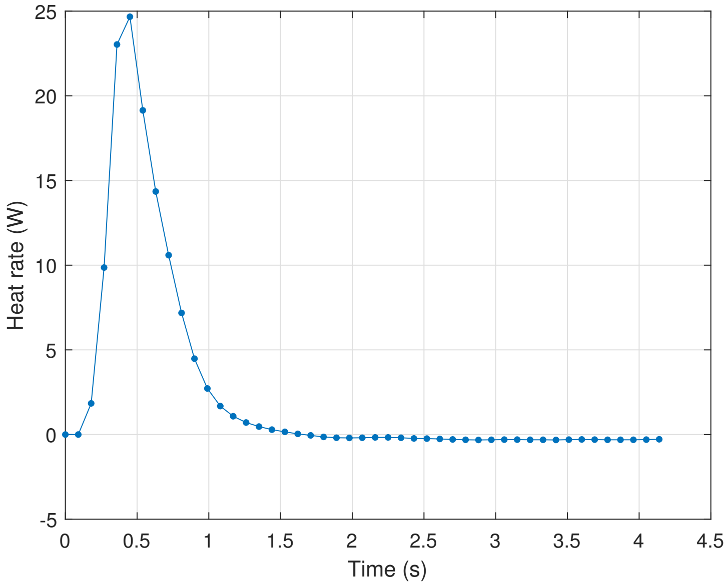

Figure 6.6 – Heat rate estimation using temperature measured in 90 ms reading time step, r=3.

a value of 44 °C. During the cooling (after 1 second) the experimental and numerical temperatures closely align, indicating the accuracy of the estimation.

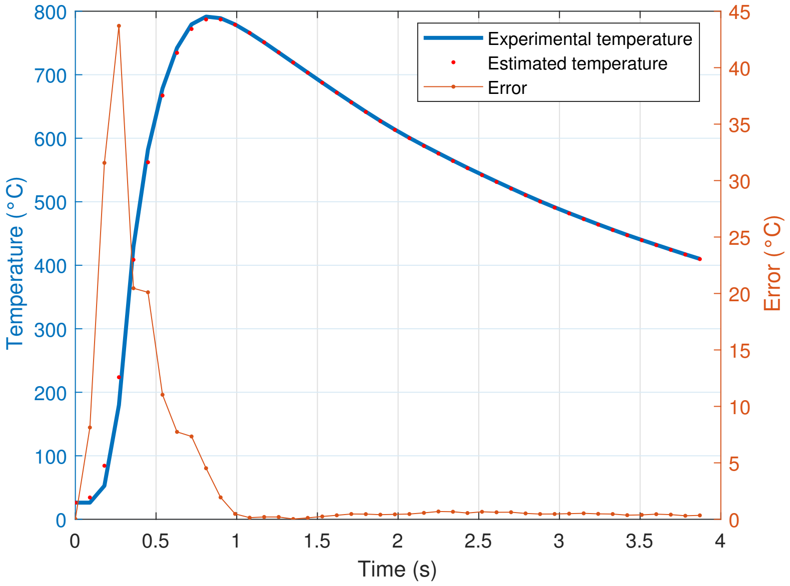

Figure 6.7 – Comparison between experimental and estimated temperatures.

6.2.2 Estimating using the 4 ms reading time step experiments

For r=10, the maximum value of $\hat{Q}$ was 140 W. The heat rate reaches its maximum value between 0.02 and 0.03 seconds and returned to zero by 0.5 seconds. The estimation results are depicted in Figure 6.8.

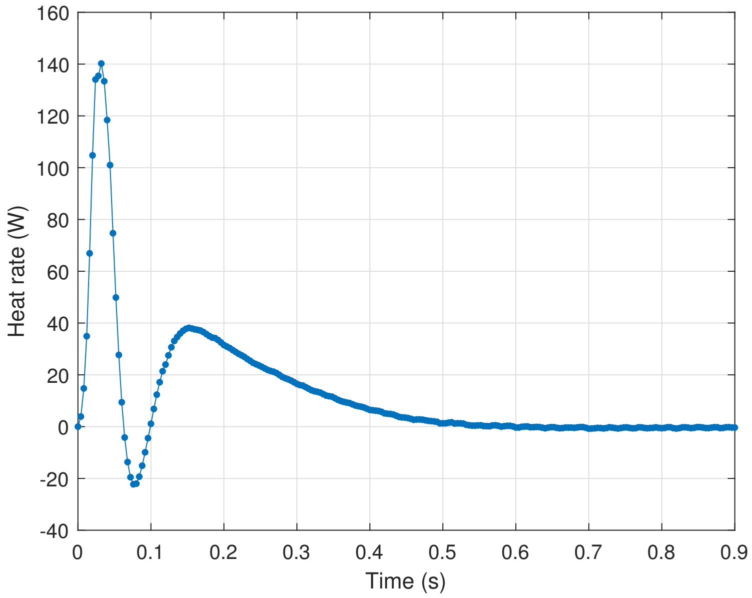

(a) Using r=10.

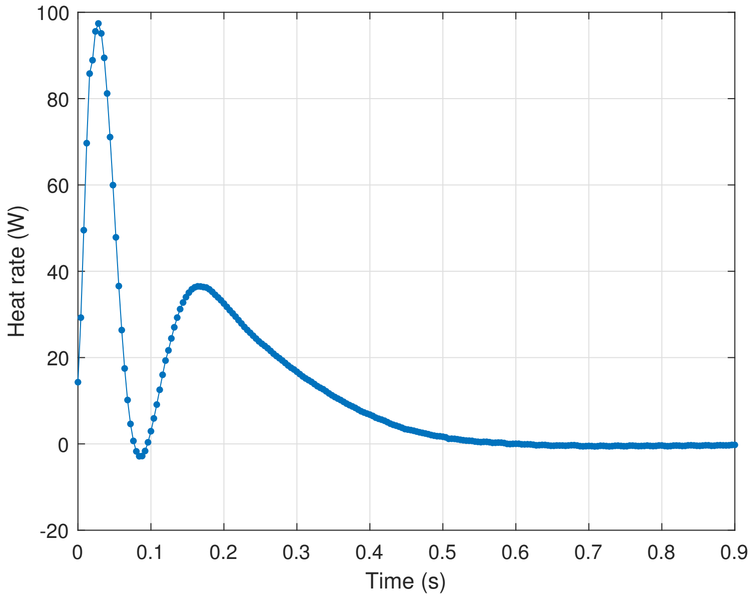

(b) Using r=13.

Figure 6.8 – Estimated heat rate without considering measuring thermocouple effect.

To calculate the welding process efficiency, it was necessary to calculate the energy generated by the estimated heat rate, measured in Joules. This energy can be calculated either by measuring the area under the graphic in Figure 6.8 or by integrating the estimated heat rate over time, resulting in 11.03 J, for r=10 and 11.06 J, for r=13.

Figure 6.9 illustrates a comparison between experimental and calculated temperatures, using the estimated heat rate and the residuals between the experimental and numerical temperatures are also displayed. Using r=10, The average residual during the first second of process was 0.63 °C, the standard deviation of 1.85 °C, the maximum residual reaches a value of 10 °C. After 0.2 second the experimental and numerical temperatures closely align, indicating the accuracy of the estimation. Using r=13, The average residual during the first second of process was 1.23 °C, the standard deviation of 3.10 °C, the maximum residual reaches a value of 17 °C. After 0.4 second the experimental and numerical temperatures closely align, indicating the accuracy of the estimation.

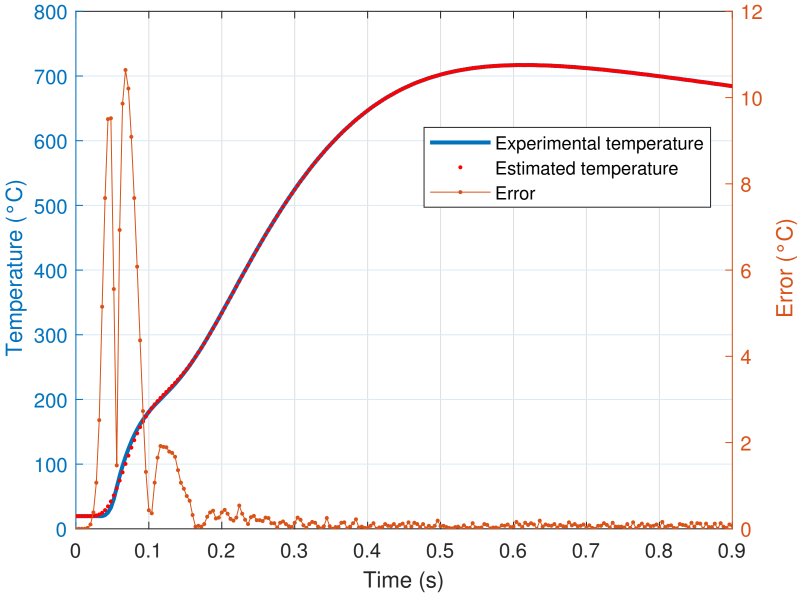

(a) Using r=10.

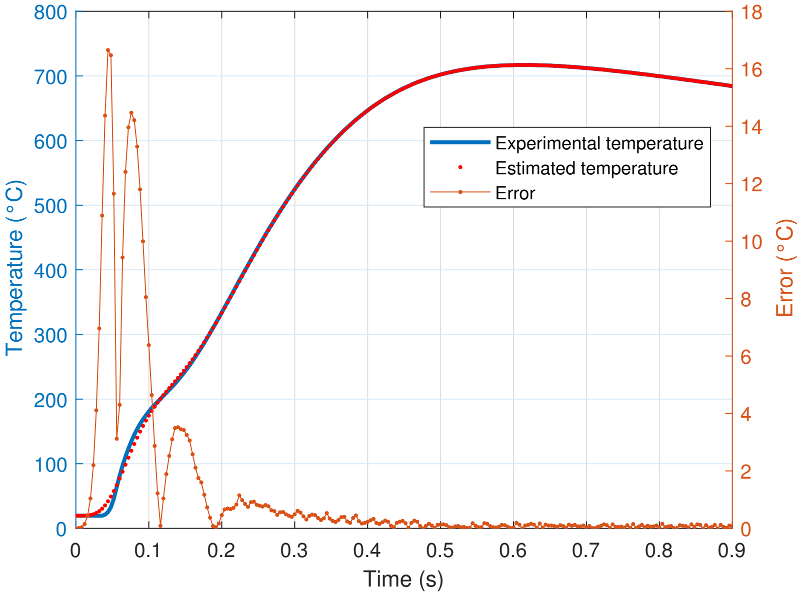

(b) Using r=13.

Figure 6.9 – Comparison between experimental and estimated temperatures

6.3 Two thermocouple wires with Joule Effect and measuring bead

In this approach the measuring thermocouple beads is considered in the thermal model, as shown in Figure 6.10. In addition the Joule effect was added in the model.

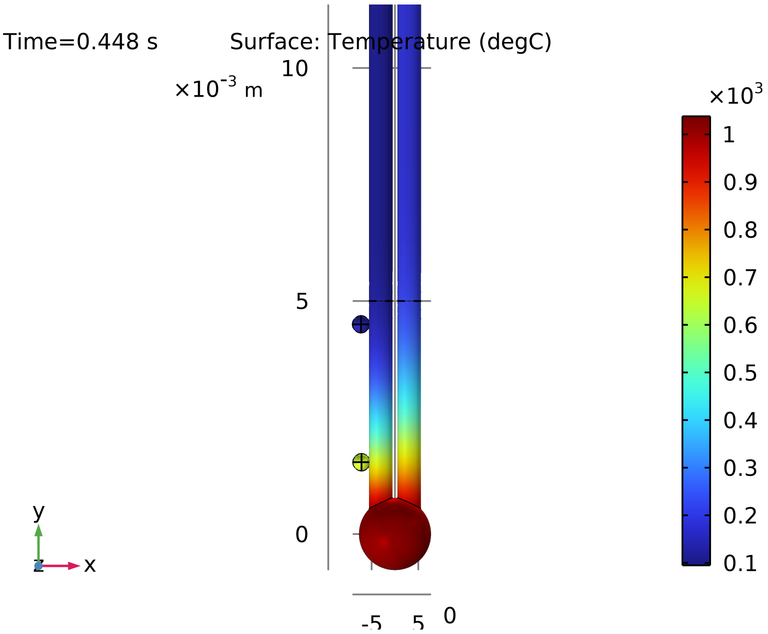

Figure 6.10 – Three-dimensional thermal model representing the thermocouple with measuring bead.

To calculate the heat generated by the Joule effect, it is necessary to consider a resistors association, as shown in Figure 6.11. Since the resistivity of each wire differs, the current passing through the resistors will be different. Given that the wires are connected in parallel, the total current is the sum of each wire current, and the voltage remains constant for both. Consequently, the current is inversely proportional to the resistivity (ρ), as expressed in Equations (6.7) and (6.8). Therefore, the heat generated by the Joule effect is greater in the alumel wire.

$$i_{chromel} = i_{Total}\frac{\rho_{alumel}}{\rho_{alumel} + \rho_{chromel}} \tag{6.7}$$

$$i_{alumel} = i_{Total}\frac{\rho_{chromel}}{\rho_{alumel} + \rho_{chromel}} \tag{6.8}$$

6.3.1 Estimating using two thermocouple wires with measuring bead

For r=10, the maximum value of $\hat{Q}$ was 314 W, the heat rate reaches its maximum value in 0.03 seconds and returned to zero by 0.42 seconds. For r=13, the maximum value of $\hat{Q}$ was 161 W, the heat rate reaches its maximum value in 0.03 seconds and returned to zero by 0.5 seconds. The estimation results are depicted in Figure 6.12.

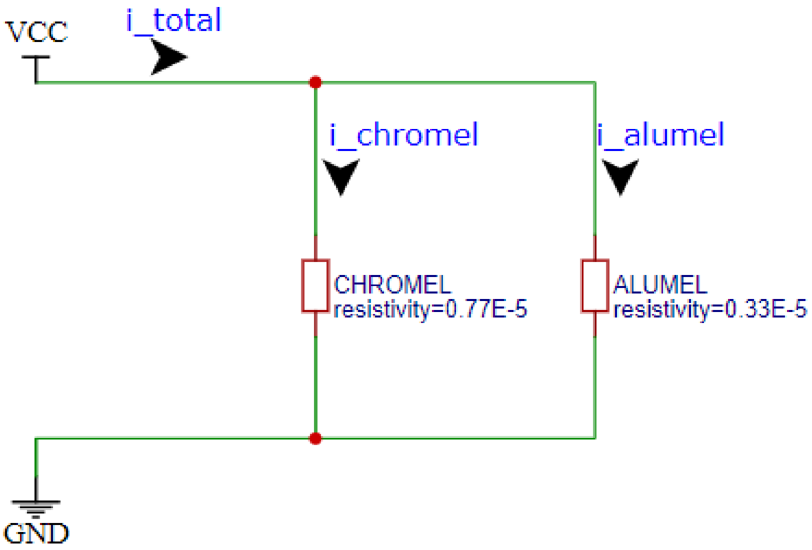

Figure 6.11 – Resistors association.

To calculate the welding process efficiency, it was necessary to calculate the energy generated by the estimated heat rate, measured in Joules. This energy can be calculated either by measuring the area under the graphic in Figure 6.12 or by integrating the estimated heat rate over time, resulting in 11.27 J, for r=10 and 11.28 J, for r=13.

Figure 6.13 illustrates a comparison between experimental and calculated temperatures, using the estimated heat rate and the residuals between the experimental and numerical temperatures are also displayed. Using r=10, The average residual during the first second of process was 0.36 °C, the standard deviation of 1.11 °C, the maximum residual reaches a value of 8 °C. After 0.15 second the experimental and numerical temperatures closely align, indicating the accuracy of the estimation. Using r=13, The average residual during the first second of process was 0.61 °C, the standard deviation of 1.66 °C, the maximum residual reaches a value of 13 °C. After 0.25 second the experimental and numerical temperatures closely align, indicating the accuracy of the estimation.

6.4 Comparison between the solutions

Due to the rapid nature of the Joule effect (20 ms), the heat generated by it was not clearly evident in the temperature data taken at 90 ms reading intervals. However, in experiments with a 4 ms reading time step, the presence of the Joule effect through the wires was clearly observed. Additionally, the shorter reading time step enabled smaller errors in the estimation, indicating that the computational model better and more accurately represented the phenomenon. This highlights the significance of using shorter reading intervals to capture rapid nature phenomenon, such as the Joule Effect.

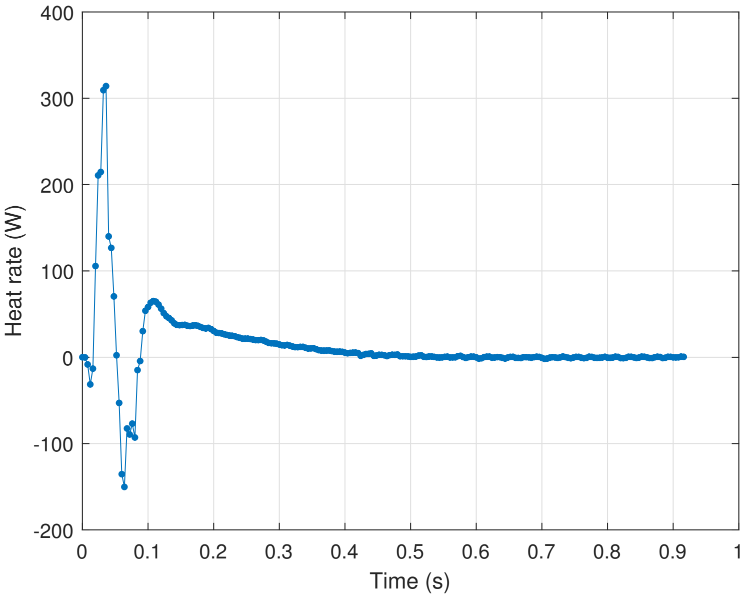

(a) Using r=10.

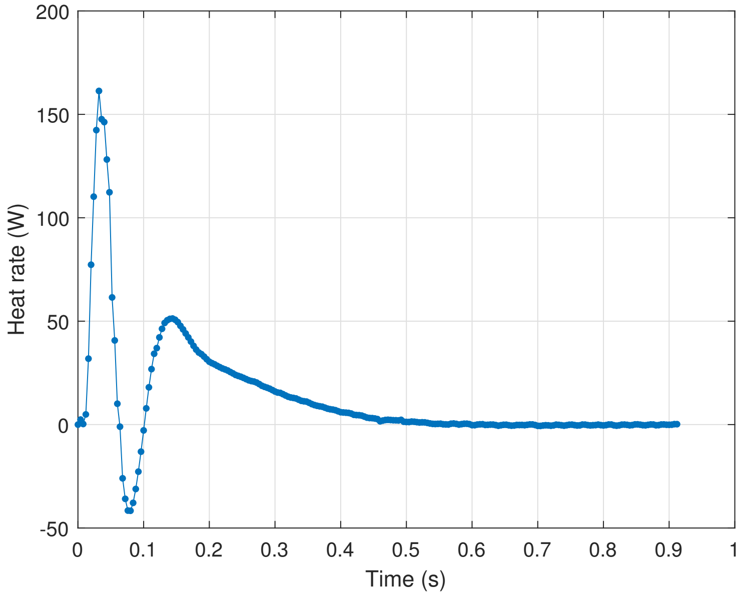

(b) Using r=13.

Figure 6.12 – Heat rate estimation using temperature measured in 4 ms reading time step.

Table 6.1 presents a comparison between experimental and estimated temperature data, using different experiments and modeling approaches. It is observed that both maximum and mean temperature residuals were smaller with a 4 ms reading time step compared to a 90 ms reading time step. This result highlights that the accuracy of temperature estimation improves significantly with the reduction of the measurement interval and the improvement of the experimental procedure, as more frequent data provides a more detailed temporal resolution of the process.

The analysis of future times and their impact on temperature accuracy shows that,

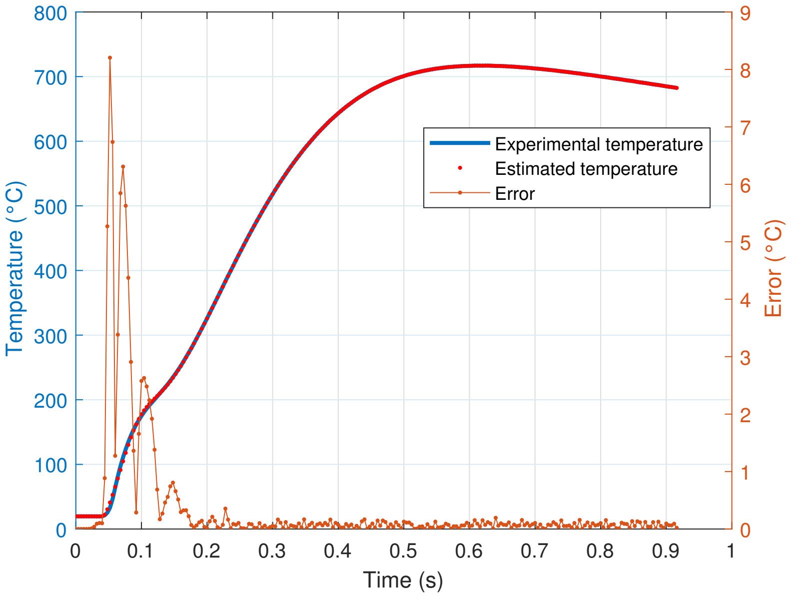

(a) Using r=10.

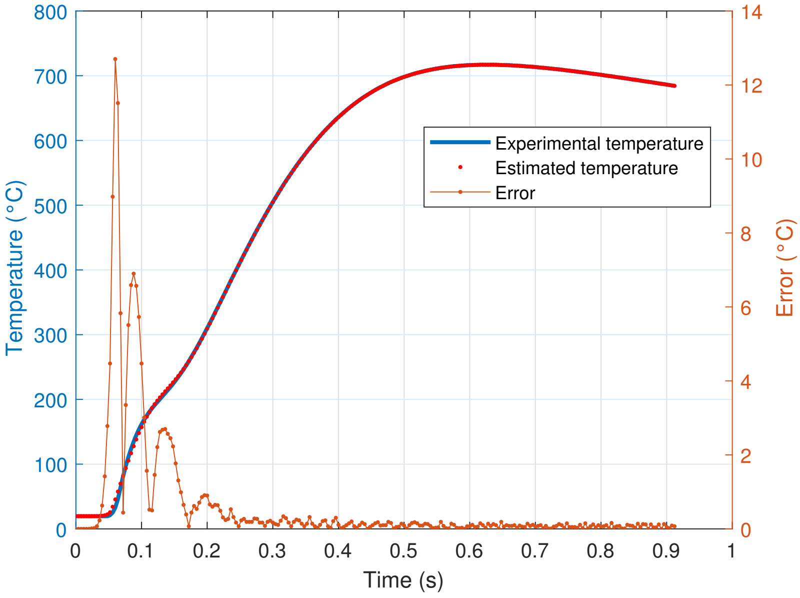

(b) Using r=13.

Figure 6.13 – Comparison between experimental and estimated temperatures, with the bead

by using smaller future times, the average differences between estimated and experimental temperatures decrease. However, when calculating the thermal input, the variation in estimates does not result in significant differences. As indicated in the table, the thermal input was approximately the same for all estimates, ranging from 11.03 J to 11.30 J, regardless of the temperature residuals.

Furthermore, considering the Joule effect in the modeling (r=10 and r=13) led to an additional improvement in the accuracy of the estimates, reflected in the smaller maximum and mean temperature residuals. This indicates that including additional physical effects in the model can lead to a better representation of the thermal process, further reducing residuals and variability in estimates.

Therefore, to improve the model and experiments, it is important to conduct experiments carefully and analyze how the reading intervals impact in the data accuracy, while considering all relevant physical effects in the welding process. Although the temperature residuals were smaller with shorter measurement intervals, the difference in calculating the thermal input was insignificant. This finding suggests that, while the precision of the measured temperature is important for understanding the process details, the total estimated thermal energy remains consistently accurate across different measurement configurations.

Table 6.1 – **Comparison between estimation.**

	90 ms interval	4 ms interval		Approaching Joule effect	
	r=3	r=10	r=13	r=10	r=13
Maximum residual	44 °C	10 °C	17 °C	8 °C	13 °C
Mean residual	13 °C	0.63 °C	1.23 °C	0.36 °C	0.61 °C
Standard deviation	13.48 °C	1.85 °C	3.10 °C	1.11 °C	1.66 °C
Thermal energy input	11.30 J	11.03 J	11.06 J	11.27 J	11.28 J

6.5 Thermal efficiency

Efficiency is given as:

$$\eta = \frac{U_{estimated}}{W_{Total}} \tag{6.9}$$

where η is the efficiency, U is the thermal energy provided to the thermocouple, which is calculated by integrating the estimated heat rate over the time, thermal energy is presented in the Table 6.1, and W is the total welding energy. The welding energy can be calculated by integrating the area of the "welding power"presented in Figure 5.4 the section 5.1.1, resulting in 24.5 J when we consider the Joule effect. When it is not considered the Joule effect, the calculus suggest a higher energy to the welding, 28.83 J. Then the thermal efficiency results in 0.45 when the model considers the Joule effect while 0.38 if the Joule effect it is not approached. The result of the efficiency confirm the efficiency used for one wire in the section 6.1.

7 Conclusion and Perspectives

In this study, the capacitor discharge method was employed to validate the technique of using thermocouples for temperature measurement. The research combined the necessity of an apparatus for welding thermocouples onto metallic surfaces and utilized the apparatus itself to conduct experiments. These experiments aimed to evaluate temperature measurements and obtain experimental data for estimating the heat transfer rate during the welding process using an inverse heat transfer problem technique. Additionally, phase change considerations were incorporated into the thermal model since the temperatures involved reached the melting points of the metals studied.

The transient temperature measurement approach using thermocouples highlighted the need to consider the influence and error introduced by the weld bead. The effect of the weld bead must be analyzed on a case-by-case basis. For example, in processes where the temperature changes slowly, the weld bead effect tends to be less significant compared to cases with rapid temperature changes. Additionally, the size of the measured surface relative to the weld bead is important; a smaller surface area in relation to the weld bead can amplify the temperature difference between the surface and the bead, as was the case in this study. Therefore, careful consideration of these factors is essential for accurate temperature measurements in transient conditions.

The results of estimation using the inverse heat transfer problem method underscored the importance of precise experiments and robust thermal models for achieving accurate estimations. The quality of the experiment, including factors such as low reading time steps and the use of thin thermocouples, significantly reduced the temperature difference between experimental and estimated values. Similarly, improvements in the thermal model, such as incorporating the previously unaccounted-for Joule effect, led to enhancements in accuracy.

Despite the lower precision in the estimated temperatures in some cases, there was no significant difference in the calculation of the thermal input for the process, resulting in similar efficiency across all approaches. While there is considerable variation in thermal efficiency calculations in the literature, this study demonstrates consistency when compared with some existing studies. However, there is a lack of literature addressing the thermal efficiency for the capacitor discharge process specifically.

7.1 Perspectives

The present study did not include a detailed simulation of the fluid formation during the CDW process. Modeling the fluid behavior involves highly complex phenomena such as free surface dynamics, surface tension, phase change, and electromagnetic–thermomechanical coupling. Each of these aspects requires dedicated models and significantly increases computational cost and simulation time. In addition, the short duration of the bead formation, on the order of 20 milliseconds, it is expected that the influence of the molten material flow on the overall thermal analysis is limited. The rapid solidification and the localized nature of the energy input suggest that most of the relevant thermal phenomena occur after or concurrently with bead stabilization. Therefore, the fluid dynamics component was neglected in favor of focusing on heat transfer behavior. This choice allowed for a understanding of thermal phenomena and parameters estimation methods without conflating results with complex multiphysics effects.

However, fluid behavior remains an important perspective for future work. A dedicated study focusing exclusively on the modeling and simulation of fluid formation during capacitor discharge welding could provide a deeper understanding of material deformation and its interaction with thermal distribution. Another promising alternative would be to adopt a quasi-dynamic approach that does not explicitly simulate fluid flow, but instead introduces geometric or boundary condition changes in the numerical model over time. This could partially mimic the physical displacement of the material and bring the simulation closer to real conditions, without the full complexity of fluid modeling.

Regarding temperature measurement using thermocouples, the present study opens up new opportunities for improving the understanding of thermal losses. For instance, future work could quantify the heat lost through the thermocouple wires and the weld bead. Such analyses could lead to the development of correction factors or compensation models, enhancing the accuracy of temperature measurements in transient processes involving thermocouples. These corrections could be broadly applicable in other industrial or laboratory applications that require precise thermal measurements.

Lastly, the methodology developed in this research, combining experimental analysis, thermocouple temperature measurements, and inverse heat transfer modeling, can be extended to other welding processes or thermal applications involving rapid heating and localized energy inputs. The inverse problem approach demonstrated here proved effective for estimating heat flux in conditions where direct measurement is not feasible, and it remains a promising tool for thermal diagnostics in complex industrial scenarios.

Moreover, based on the same model and experimental data developed in this work, future studies may explore the application of alternative inverse methods, such as the Levenberg-Marquardt algorithm, and compare their performance with the results obtained using the nonlinear specified function method. This could provide a broader understanding of the strengths and limitations of different inverse techniques when applied to fast, high-intensity thermal processes.

References

1 HOLMAN, J. P. *Experimental Methods For Engineers*. McGraw-Hill's, 2012. ISBN 9780073529301. Disponível em: <https://books.google.com.br/books?id=9B9VAQAACAAJ>. 19, 22, 23, 24

2 MICHALSKI, D.; STRąK, K.; PIASECKA, M. Estimating uncertainty of temperature measurements for studies of flow boiling heat transfer in minichannels. *The European Physical Journal Conferences*, v. 213, p. 02059, 06 2019. 22

3 KEE, Y. et al. Uncertainty of temperature measured by thermocouple. *Journal of Advanced Research in Fluid Mechanics and Thermal Sciences*, v. 68, p. 54–62, 03 2020. 22

4 WOOLLEY, J. et al. Obtaining the sensed temperatures from a detailed model of a welded thermocouple. In: . [S.l.: s.n.], 2008. v. 10. 22, 23

5 WOOLLEY, J.; WOODBURY, K. Thermocouple data in the inverse heat conduction problem. *Heat Transfer Engineering - HEAT TRANSFER ENG*, v. 32, p. 811–825, 08 2011. 22

6 ABDELAZIZ, Y. et al. Characterizing drift behavior in type k and n thermocouples after high temperature thermal exposures. *Journal of Advanced Research in Fluid Mechanics and Thermal Sciences*, v. 97, p. 62–74, 08 2022. 23

7 TSAI, C. et al. Analysis and development of a real-time control methodology in resistance spot welding. *Weld. J.*, v. 69, p. 339–351, 01 1991. 24

8 WANG, J. et al. Impulse capacitor discharge welding of hollow structure made of nickel-base alloy. *Tsinghua Science & Technology*, v. 12, n. 4, p. 453–458, 2007. ISSN 1007-0214. Disponível em: <https://www.sciencedirect.com/science/article/pii/S1007021407700676>. 25, 26

9 WILSON JR, R. D.; WOODYARD, J. R.; DEVLETIAN, J. H. Capacitor discharge welding: Analysis through ultrahigh-speed photography. *Welding Journal (Miami); (United States)*, v. 72:3, n. 1, 3 1993. ISSN 0043-2296. Disponível em: <https://www.osti.gov/biblio/6585932>. 25, 27

10 YUSHAN, Z.; DONG, S.-J.; ELY, K. Weldability of thin sheet metals by small-scale resistance spot welding using high-frequency inverter and capacitor-discharge power supplies. *Journal of Electronic Materials*, v. 30, p. 1012–1020, 08 2001. 25

11 GOULD, J. et al. Capacitor discharge spot welding of aluminum, part 1: Weldability assessments. *Welding Journal*, v. 100, p. 309–322, 10 2021. 25

12 CHIOZZI, S.; DATTOMA, V.; PANELLA, F. Capacitor discharge welded bars of inconel 718 and tial6v4 superalloys under fatigue. *Materials & Design*, v. 29, n. 4, p. 839–851, 2008. ISSN 0261-3069. Advances in Production and Processing of Aluminium. Disponível em: <https://www.sciencedirect.com/science/article/pii/S0261306907000726>. 26

13 CAO, X. et al. Capacitor discharge welding of nuts to steel sheets. *Journal of Materials Processing Technology*, v. 264, p. 486–493, 2019. ISSN 0924-0136. Disponível em: <https://www.sciencedirect.com/science/article/pii/S0924013618304369>. 26

14 LIENERT, T. et al. Projection-capacitor discharge resistance welding of 430 stainless steel and 14ywt. *Journal of Manufacturing Processes*, v. 75, p. 1189–1201, 2022. ISSN 1526-6125. Disponível em: <https://www.sciencedirect.com/science/article/pii/S1526612522000536>. 26, 27

15 VERÁSTEGUI, R. N. et al. Capacitive welding of sae 10b22 steel with sae 1045, domex 700mc and docol dp 1000 steels. *Soldagem & Inspecao*, v. 26, 2021. Disponível em: <https://doi.org/10.1590/0104-9224/SI26.05>. 26

16 CARBONE, R.; LANGELLA, A. Numerical modeling of resistance welding process in joining of thermoplastic composite materials using comsol multiphysics. In: . [S.l.: s.n.], 2009. 30

17 SALEEM, J. et al. Nugget formation during resistance spot welding using finite element model. *Int. Sci. Index*, v. 6, p. 707–712, 01 2012. 30

18 VURAL, M. Finite element analysis of the thermo-mechanical behavior of the resistance spot welding. *Usak University Journal of Material Sciences*, v. 2, p. 31–44, 06 2013. 30

19 ZAMMAR, I. et al. A three-dimensional transient model for heat transfer in thermoplastic composites during continuous resistance welding. *Advanced Manufacturing: Polymer & Composites Science*, Taylor & Francis, v. 3, n. 1, p. 32–41, 2017. Disponível em: <https://doi.org/10.1080/20550340.2017.1311094>. 30

20 JAIN, A.; PARHIZI, M. Theoretical analysis of phase change heat transfer and energy storage in a spherical phase change material with encapsulation. *International Journal of Heat and Mass Transfer*, v. 185, p. 122348, 2022. ISSN 0017-9310. Disponível em: <https://www.sciencedirect.com/science/article/pii/S0017931021014472>. 30

21 HADAMARD, J. *Lectures on Cauchy's Problem in Linear Partial Differential Equations*. New Haven, CT: Yale University Press, 1923. 31

22 CUI, M.; DUAN, W. wei; GAO, X. wei. A new inverse analysis method based on a relaxation factor optimization technique for solving transient nonlinear inverse heat conduction problems. *International Journal of Heat and Mass Transfer*, v. 90, p. 491–498, 2015. ISSN 0017-9310. Disponível em: <https://www.sciencedirect.com/science/article/pii/S0017931015007188>. 31

23 GOLUB, G. H.; HANSEN, P. C.; O'LEARY, D. P. Tikhonov regularization and total least squares. *SIAM Journal on Matrix Analysis and Applications*, v. 21, n. 1, p. 185–194, 1999. Disponível em: <https://doi.org/10.1137/S0895479897326432>. 31

24 KENNEDY, P. *A Guide to Econometrics*. MIT Press, 2003. (Mit Press). ISBN 9780262611831. Disponível em: <https://books.google.fr/books?id=B8I5SP69e4kC>. 31

25 BECK, J.; BLACKWELL, B.; CLAIR, C. *Inverse Heat Conduction: Ill-Posed Problems*. Wiley, 1985. (Wiley-Interscience publication). ISBN 9780471083191. Disponível em: <https://books.google.com.br/books?id=-1hzLAb_ZL0C>. 31, 33

26 NANFUKA, M.; BERNTSSON, F.; KAKUBA, G. Solving a cauchy problem for the heat equation using cubic smoothing splines. *Applicable Analysis*, Taylor & Francis, v. 0, n. 0, p. 1–16, 2021. Disponível em: <https://doi.org/10.1080/00036811.2021.1876224>. 33, 34

27 BECK, J. V. Nonlinear estimation applied to the nonlinear inverse heat conduction problem. *International Journal of heat and mass transfer*, Elsevier, v. 13, n. 4, p. 703–716, 1970. 33

28 STOLZ G., J. Numerical Solutions to an Inverse Problem of Heat Conduction for Simple Shapes. *Journal of Heat Transfer*, v. 82, n. 1, p. 20–25, 02 1960. ISSN 0022-1481. Disponível em: <https://doi.org/10.1115/1.3679871>. 33

29 CHEN, C.-K.; WU, L.-W.; YANG, Y.-T. Comparison of whole-domain and sequential algorithms for function specification method in the inverse heat transfer problem of laminar convective pipe flow. *Numerical Heat Transfer*, Part A: Applications, p. 927–947, 12 2006. 33

30 BERNTSSON, F. An inverse heat conduction problem and improving shielded thermocouple accuracy. *Numerical Heat Transfer Part A-applications - NUMER HEAT TRANSFER PT A-APPL*, v. 61, p. 754–763, 05 2012. 33

31 SAMADI, F.; KOWSARY, F.; SARCHAMI, A. Estimation of heat flux imposed on the rake face of a cutting tool: A nonlinear, complex geometry inverse heat conduction case study. *International Communications in Heat and Mass Transfer*, v. 39, n. 2, p. 298–303, 2012. ISSN 0735-1933. Disponível em: <https://www.sciencedirect.com/science/article/pii/S0735193311002351>. 33

32 BRITO, R.; CARVALHO, S.; Lima E Silva, S. Experimental investigation of thermal aspects in a cutting tool using comsol and inverse problem. *Applied Thermal Engineering*, v. 86, p. 60–68, 2015. ISSN 1359-4311. Disponível em: <https://www.sciencedirect.com/science/article/pii/S1359431115003907>. 34

33 NGENDAHAYO, J. P.; NIYOBUHUNGIRO, J.; BERNTSSON, F. Estimation of surface temperatures from interior measurements using tikhonov regularization. *Results in Applied Mathematics*, v. 9, p. 100140, 2021. ISSN 2590-0374. Disponível em: <https://www.sciencedirect.com/science/article/pii/S2590037420300509>. 34

34 SHI, H. et al. Corrosion resistance and microstructural stability of austenitic fe–cr–al–ni model alloys exposed to oxygen-containing molten lead. *Journal of nuclear materials*, Elsevier B.V, v. 524, p. 177–190, 2019. ISSN 0022-3115.

35 SUN, W. et al. Phase-field simulation of microstructural evolution of γ precipitate in γ' matrix in binary ni-al alloys. *Procedia Engineering*, v. 36, p. 200–206, 2012. ISSN 1877-7058. IUMRS International Conference in Asia 2011. Disponível em: <https://www.sciencedirect.com/science/article/pii/S1877705812015585>.

36 BUTTSWORTH, D. Assessment of effective thermal product of surface junction thermocouples on millisecond and microsecond time scales. *Experimental Thermal and Fluid Science*, v. 25, p. 409–420, 12 2001. 41

37 SASAKI, S. et al. Simultaneous measurements of specific heat and total hemispherical emissivity of chromel and alumel by a transient calorimetric technique. *International Journal of Thermophysics*, v. 15, n. 3, p. 547–565, may 1994. 42

38 BECK, J.; ARNOLD, K. *Parameter Estimation in Engineering and Science*. Wiley, 1977. (Probability and Statistics Series). ISBN 9780471061182. Disponível em: <https://books.google.com.br/books?id=_qAYgYN87UQC>. 45

39 WOODBURY, K. A. *Inverse Engineering Handbook*. CRC Press, 2002. ISBN 9780429117893. Disponível em: <https://doi.org/10.1201/9781420041613>. 46

40 FERMO, I. R. et al. Equipamento automatizado de soldagem capacitiva para termopares. *Soldagem & Inspeção*, v. 24, 01 2019. 49

41 BOYLESTAD, R. *Introdução À Análise De Circuitos*. PEARSON BRASIL, 2019. ISBN 9788543024981. Disponível em: <https://books.google.com.br/books?id=kEenwwEACAAJ>. 56

42 STENBACKA, N. On arc efficiency in gas tungsten arc welding. *Soldagem e Inspeção*, v. 18, p. 380–390, 10 2013. 87

43 DUPONT, J.; MARDER, A. Thermal efficiency of arc welding processes. *Welding Journal, Research Supplement*, p. 406s – 416s, Dec 1995. 87

44 DOURADO, R. et al. Estimating the absorption efficiency in a laser welding process using a nonlinear inverse problem method. *International Journal of Thermal Sciences*, v. 183, p. 107846, 01 2023. 90